

SINGLE-CELL ANALYSIS ON THE BIOLOGICAL CLOCK USING MICROFLUIDIC
DROPLETS

by

ZHAOJIE DENG

(Under the Direction of Leidong Mao and Jonathan Arnold)

ABSTRACT

Single-cell analysis has become crucial for uncovering the underlying mechanism for cell heterogeneity. Different biological questions pose different challenges for single-cell analysis. In order to answer questions like, whether a single-cell has a biological clock and how the clocks synchronize among cells to overcome the heterogeneity, continuous long-term measurement on large numbers of single-cells is required. However traditional measurement techniques usually involve measurement on millions of cells. My dissertation addresses these challenges by developing a microfluidic droplet platform capable of measuring the biological clock on >1000 *Neurospora crassa* single-cells for up to 10 days. The results show that in *Neurospora crassa* a single cell has the three major properties of a biological clock: a circadian oscillator, light entrainment, and temperature compensation and that single-cells synchronize their biological clock with each other possibly through quorum sensing.

INDEX WORDS: Single-cell analysis, Microfluidic droplets, *Neurospora crassa*, Circadian rhythm, Biological clock, Stochastic noise, Synchronization

SINGLE-CELL ANALYSIS ON THE BIOLOGICAL CLOCK USING MICROFLUIDIC
DROPLETS

by

ZHAOJIE DENG

B.A., Huazhong University of Science and Technology, China, 2008

M.S., Huazhong University of Science and Technology, China, 2011

A Dissertation Submitted to the Graduate Faculty of The University of Georgia in Partial
Fulfillment of the Requirements for the Degree

DOCTOR OF

PHILOSOPHY

ATHENS, GEORGIA

2017

© 2017

ZHAOJIE DENG

All Rights Reserved

SINGLE-CELL ANALYSIS ON THE BIOLOGICAL CLOCK USING MICROFLUIDIC
DROPLETS

by

ZHAOJIE DENG

Major Professor: Leidong Mao
Co-Major Professor: Jonathan Arnold
Committee: Heinz-Bernd Schüttler
Xianqiao Wang

Electronic Version Approved:

Suzanne Barbour
Dean of the Graduate School
The University of Georgia
December 2017

ACKNOWLEDGMENTS

I would like to thank my major advisors Dr. Leidong Mao and Dr. Jonathan Arnold for their constant guidance, support, and insights for this research work. Much appreciation also goes to my committee member Dr. Heinz-Bernd Schüttler for his invaluable advice during this research work. I also would like to thank Dr. Xianqiao Wang for serving on my advisory committee. I am also very grateful to my scientific collaborators Sam Arsenault, Cristian Caranica, James Griffith, Dr. Taotao Zhu, and Dr. Ahmad Al-Omari for their significant input for this thesis work. I extend my appreciation to my colleagues in the lab, especially to Dr. Taotao Zhu for the training he provided during the first year of my PhD, and Dr. Rui Cheng and Wujun Zhao for their technical assistance and suggestions. Last but not least, I would like to express my deepest gratitude to my parents who are always supportive and my husband for his persistent encouragement and unconditional love.

TABLE OF CONTENTS

	Page
ACKNOWLEDGEMENTS	iv
LIST OF FIGURES	vii
LIST OF TABLES	x
1 OVERVIEW	1
1.1 Introduction	1
1.2 Organization of the Dissertation	3
2 MOTIVATION	5
2.1 Review of methods for measurements on the biological clock at the single-cell level	5
2.2 Review of technologies for single-cell isolation and long-term measurement	8
3 EXPERIMENTAL METHODS	14
3.1 Strains and Media	14
3.2 Microfluidic device design and fabrication	14
3.3 Droplets generation and cell encapsulation	16
3.4 Time-lapse imaging	20
3.5 Correction of CCD image imperfections	21

3.6	Image processing	22
3.7	Control experiments for choosing objective magnification	23
3.8	Data analysis	28
3.9	Experimental noise calibration with fluorescence beads	29
3.10	Temperature stability verification of the measuring setup	32
4	SINGLE-CELL CIRCADIAN OSCILLATORS IN <i>NEUROSPORA CRASSA</i>	38
4.1	Measurements of expression on single cells over 10 days	39
4.2	Stochastic oscillators in single-cells	41
4.3	Single-cells circadian oscillators in <i>Neurospora Crassa</i> can be entrained by light	47
4.4	Temperature compensation is observed in single cells of <i>Neurospora crassa</i>	57
4.5	Conclusion	61
5	SYNCHRONIZATION OF THE BIOLOGICAL CLOCK <i>NEUROSPORA CRASSA</i>	64
5.1	Synchronization measures of the circadian stochastic oscillators.	64
5.2	A deterministic quorum sensing model for the circadian oscillators	66
5.3	Synchronization of stochastic circadian oscillators	72
5.4	Light synchronized the circadian oscillators in <i>Neurospora Crassa</i>	85
5.5	Conclusion	95
6	CONCLUSION	99

List of Figures

	Page
Figure 3.1 Schematics of the droplet-generating device.	15
Figure 3.2 Droplet generation and cell incubation.	16
Figure 3.3 Percoll stabilizes the cell movement.	19
Figure 3.4 Droplets are very stable during time-lapse imaging.	24
Figure 3.5 Cell grouping and tracking.	25
Figure 3.6 62 single-cell fluorescence intensity time series under different magnifications.	27
Figure 3.7 Coefficient of determination, R-square, was calculated by fitting linear regression on the fluorescence intensity of the cells measured under the lower magnifications, 5X, 10X, and 20X, against that measured under 50X.	27
Figure 3.8 No change in Projected Cell Surface Area (PCSA) indicates no germination, and no change in cell-to-cell distance indicates no cell fusion.	29
Figure 3.9 The beads signal variance varies quadratically with the mean bead fluorescence signal in the six-experiment bead data set	31
Figure 3.10 Temperature stability of the thermal stage	33
Figure 3.11 Rhodamine B (RB) intensity correlates with room temperature	35

Figure 3.12 LED light source output correlates with room temperature	35
Figure 3.13 Photobleaching decay in the Rhodamine B intensity	36
Figure 3.14 Detrended Rhodamine B time series for temperature compensation experiments	37
Figure 4.1 Oscillators of single cells can be measured with the workflow involving droplet microfluidics devices and fluorescent recorders of a clock output gene.	40
Figure 4.2 The oscillators in single cells of <i>N. crassa</i> are circadian with a period of 21 h in the dark (D/D), but there is substantial variation in phase and amplitude captured in a stochastic genetic network fitting the single cell clock data.	42
Figure 4.3 Relationship between period, amplitude, and phase of the circadian oscillator.	46
Figure 4.4 The microfluidic droplet platform integrated with a LED light to control the light-dark cycles that the cells experienced.	50
Figure 4.5 Entrainability of Single cell <i>N. crassa</i> to a 6 hours artificial day with 3 hours light on and 3 hours light off.	51
Figure 4.6 Entrainability of Single cell <i>N. crassa</i> to a 12 hours artificial day with 6 hours light on and 6 hours light off.	53
Figure 4.7 Entrainability of Single cell <i>N. crassa</i> to a 36 hours artificial day with 18 hours light on and 18 hours light off.	55

Figure 4.8 Period, amplitude and phase of the entrained oscillators under 3 hours light on and 3 hours light off.	56
Figure 4.9 Period, amplitude and phase of the entrained oscillators under 6 hours light on and 6 hours light off.	58
Figure 4.10 Period, amplitude and phase of the entrained oscillators under 18 hours light on and 18 hours light off.	59
Figure 4.11 Single cell temperature compensation.	62
Figure 5.1 Conidial cells communicate the state of their oscillators to each other within a droplet.	71
Figure 5.2 The synchronization as measured by the “order parameter” R or Hilbert transform phase synchronization.	74
Figure 5.3 The Kuramoto order parameter K displays an alternating structure with number of cells per droplet and substantial coherence between oscillators.	75
Figure 5.4 The synchronization surface for the Kuramoto phase-locking model .	76
Figure 5.5 The synchronization surface (ICC) is a function of genotype.	77
Figure 5.6 Randomly picked trajectories	78
Figure 5.7 The synchronization surface for the <i>prd-4</i> knockout is significantly different from that of the reference strain, <i>ccg-2p:mCherry</i> (MFNC9).	82
Figure 5.8 ICC surface of cells under 3 light entrainment conditions.	98

List of Tables

	Page
Table 3.1 Number of cells per droplet distribution with cell suspension flow rate as a changing parameter	18
Table 3.2 <i>N.crass</i> cell viability after incubated in the media with different concentrations of Percoll for 6 days	19
Table 3.3 Droplet size distributions when using different concentrations of percoll	20
Table 3.4 <i>LGP</i> for objective lens with different magnifications	26
Table 3.5 R-square under different magnifications	28
Table 4.1 Temperature coefficient Q_{10} for single cell circadian oscillators . . .	61
Table 5.1 Analysis of Variance (ANOVA) of fluorescence of the <i>ccg-2</i> promoter between and within droplets is used to estimate the intraclass correlation ρ	67
Table 5.2 The mean period of single cell oscillators within a droplet increases significantly with the number of cells per droplet	73
Table 5.3 The intraclass correlation surface (ICC) for <i>prd-4Δ,ccg-2p:mCherry</i> is significantly different from that of MFNC9.	80

Table 5.4	Global response and mean period of isolated single cells in 3 light entrainment conditions.	86
Table 5.5	Phase locking value of single cells in 3 light entrainment conditions .	87
Table 5.6	Kuramoto order parameter of single cells in 3 light entrainment conditions	88
Table 5.7	Amplitude and Global Response of <i>N. crassa</i> with different neighboring cells in a droplet (number of cells per droplet) in the 3 hours light on 3 hours light off condition.	91
Table 5.8	Amplitude and Global Response of <i>N. crassa</i> with different neighboring cells in a droplet (number of cells per droplet) in the 6 hours light on 6 hours light off condition.	93
Table 5.9	Amplitude and Global Response of <i>N. crassa</i> with different neighboring cells in a droplet (number of cells per droplet) in the 36 hours light on 36 hours light off condition.	94
Table 5.10	Phase synchronization of of <i>N. crassa</i> with different neighboring cells in a droplet (number of cells per droplet) in the 3 hours light on 3 hours light off condition.	95
Table 5.11	Phase synchronization of of <i>N. crassa</i> with different neighboring cells in a droplet (number of cells per droplet) in the 6 hours light on 6 hours light off condition.	96
Table 5.12	Phase synchronization of of <i>N. crassa</i> with different neighboring cells in a droplet (number of cells per droplet) in the 18 hours light on 18 hours light off condition.	97

CHAPTER 1

OVERVIEW

1.1 Introduction

The biological clock is a timekeeping machinery that regulates almost every critical biological process in living organisms with a 24-hour rhythm (circadian rhythm). It helps plants, animals and humans to adapt to the light-dark cycle of the planet to take advantage of the optimal environment for living[1, 2]. Awareness has risen in recent years that the biological clock is fundamental to health. When the clock goes awry in mammals, it can lead to many diseases, ranging from sleep disorders[3, 4], heart disease[5, 6], and lung disease[7, 8] to cancer[9, 10] and Alzheimer's disease[11]. Also the biological clock influences treatment effects of drugs[12, 13]. For application, construction and manipulation of the clock may bring beneficial outcomes in biosensor[14–16], biotechnology[17, 18], and biopharmaceutical industries[19].

Over several decades' work, scientists identified the functional basis of the biological clock in various model organisms including *Synechococcus*, *Neurospora crassa*, *Drosophila*, *Arabidopsis*, and Mouse[20, 21]. Only recently, studying the biological clock on the single-cell level was believed to be significantly important for understanding the mechanism underlying the clock[22–26]. Cell-to-cell variation/heterogeneity always presents in single cell resolution measurement and to determine its functional meaning has been a challenge for biologists[27]. For the biological clock, implication for this heterogeneity is cell-to-cell variation in the clock's parameters such as period, phase,

and amplitude. The challenges are to understand how the cells synchronize/communicate their biological clocks with each other so that at a macroscale level they achieve a robust and deterministic clock output and whether the cell-to-cell heterogeneity in the clock has a meaningful biological function. The cell-to-cell variation also poses a challenge to establish accurate model of the biological clock to guide understanding the dynamics of the clock.

Therefore single-cell analysis on the biological clock is of great importance. Unfortunately, the biological clock is measured traditionally on a population average of millions of or tens of millions of cells with the race-tubes[35] or luminescence-based technique[38, 39]. Recent advances in experimental techniques and high-resolution imaging have allowed for monitoring circadian rhythms on a single-cell[28, 29]. However, these measurements were done on cells not spatially separated, meaning they may communicate with each other and therefore not strictly measuring the biological clock at the single cell level.

For single-cell analysis on the biological clock, several challenges need to be overcome in developing technology to measure circadian rhythms at the single cell level. These challenges include long-term temporal observations of single cell's circadian rhythm, measurement on large number of cells (>1000) simultaneously, and identification of intercellular noise (heterogeneity) and detection/measurement noise. This thesis describes a high-throughput microfluidic droplet platform that is capable of measuring the biological clock on isolated single-cells/cell-cluster (more than one cell) up to 10 days. A fluorescence reporter gene was used to observed the transcriptional behavior of a *clock controlled gene (ccg-2)*[30]. Over a thousand of single cells of *Neurospora*

Crass (*N. crassa*) can be measured simultaneously. With this platform, the heterogeneity and synchronization of the biological clock were evaluated, and the light entrainment and temperature compensation properties were measured at the single-cell level for the first time for *N. crassa*.

1.2 Organization of the Dissertation

chapter 2

This chapter reviews methods used to measure the biological clock of different model systems at the single-cell level and their limitations, microfluidic/micofabricated technologies for single-cell analysis, specifically focus on single-cell long-term measurement, and last the justifications for choosing microfluidic droplets for this dissertation work.

chapter 3

This chapter describes the materials, experimental procedures, control experiments, and data analysis. Also the technical choices behind the development of the microfluidic droplet platforms presented in this thesis work are explained.

chapter 4

This chapter describes the circadian oscillator of single-cells of *N. crassa*, light entrainment in single-cells of *N. crassa*, and temperature compensation in single-cells of *N. crassa*.

chapter 5

This chapter describes the heterogeneity and synchronization of the biological clock of single-cells of *N. crassa* .

chapter 6

This chapter has the conclusions.

CHAPTER 2

MOTIVATION

Single-cell analysis aims at studying the biological system at the single cell level, an approach now possible in genomics, transcriptomics, proteomics, and metabolomics. The motivation for single-cell analysis arises from the widely observed phenomenon of cellular heterogeneity. Such cellular heterogeneity may be partially due to the discrete bursts in gene transcriptions[31, 32]. Other reasons could be cell cycle differences, uneven partitioning of cellular contents during cell division, and circadian rhythms[33, 34]. Nevertheless, due to cellular heterogeneity, ensemble measurements on a population of cells do not give much information about the behavior of individual cells. However, it is believed that the differences among individual cells sometimes can lead to differences in the outcomes for the average population or to a different biological function. The challenge is to identify what aspects of the cellular heterogeneity serve a critical biological function[27]. Over the last decade more and more attention has been arisen to using single-cell analysis to unveil the biological information/functions that cellular heterogeneity contains/serves.

2.1 Review of methods for measurements on the biological clock at the single-cell level

The biological clock is measured traditionally on a population average of millions or tens of millions of cells with the race-tubes[35], Western Blot/qPCR to measure total

RNA[36, 37], or luminescence[38, 39] or fluorescence[30] to measure relevant total protein level. Only in the recent years, measuring the biological clock at the single-level has become possible with the advances in experimental techniques and high-resolution imaging.

Luciferase based techniques are mostly used to measure the biological clock at the single-cell level owing to their non-invasive nature and quantitative performance. Luciferases are protein enzymes that are naturally generated in some living organism[40]. It can catalyze the light-emitting ATP-dependent monooxidation of luciferin[37]. Usually, a luciferase reporter is tagged to a gene promoter so that luminescent product of interest will be expressed under the control of the promoter. Luminescence techniques do not require excitation applied to the cell sample, which has the advantages over fluorescence including lower background noise, and the absence of photobleaching and phototoxicity. Traditionally, luminescence cannot provide sufficient spatial resolution for obtaining signal at the cellular level[41]. But the advances made in high resolution imaging in recent years bring the possibility for measuring circadian rhythms at the single-cell level[41]. The camera for recording luminescence intensity is usually required to be cooled to very a low temperature, as low as ~ -80 °C, in order to be able to acquire a very weak signal from a single-cell with a high signal-to-noise ratio[42, 28, 43]. Luminescence techniques have been applied to various model organisms including bacteria[25], plants[44], and animals[45, 46] to measure circadian rhythms at the single-cell level. Stable circadian rhythms was demonstrated in unicellular cyanobacterium *Synechococcus elongatus* through using a bacterial luciferase reporter system consisting of two neutral site chromosomal insertions: *psbAI::luxAB* and *psbAI::luxCDE*[25]. In

this study, single bacteria were identified on the phase-contrast images. This is because usual spatial resolution of luminescence imaging is low due to the diffusion of luciferin as well as the transporter proteins[47, 48]. A particle bombardment was introduced by Muranaka *et.al.*, using reporter–plasmid-coated gold particles, which enables dispersed transfection into cells on the surface of a plant, and therefore bioluminescence signals from individual cells were able to be detected[47, 44]. Heterogeneity of cellular circadian clocks in a duckweed species, *Lemna gibba*, was shown by measuring bioluminescence intensity of individual cells in the intact plants[44]. Synchronized circadian rhythm of hundreds of neurons in the mammalian suprachiasmatic nucleus (SCN) was shown using mice carrying the *mPer1*-promoter driven luciferase reporter gene (*mPer1-luc*). Using bioluminescence imaging of Rat-1 fibroblasts, Welsh *et.al* found that single fibroblasts can oscillate robustly with diverse circadian periods but no coupling among them when dissociated from SCN[28].

Although less used, fluorescence based techniques have also been applied to measurements on the biological clock of cyanobacteria[49], plants[50], and mammalian tissues[51] at the single-cell level. A fluorescent signal in general is much brighter than luminescent signal and provides higher spatial resolution[52]. Therefore, fluorescence based techniques do not require an ultra-cooled CCD camera[52]. A yellow fluorescence protein (YFP) reporter was used to measure the promoter activity of *KaiBC*, a clock component of a cyanobacterial cell, in single-cells[49]. The circadian clocks of individual cyanobacterial cells exhibited stochastic response to phase resetting by temperature[49]. YFP-tagged *CCA1* in *Abrabidopsis* plant was monitored for its circadian rhythm at the single-cell level[50]. Cell-type-specific differences in period and partially

desynchronization among individual leaf cells were observed in the plant[50]. The YFP was also used to quantify the single-cell circadian rhythm in a mouse tissue explant[51]. Photobleaching in fluorescence based techniques can be problematic for long-term real-time imaging. Fluorescence also requires light to excite the fluorophore restricting its usage in monitoring circadian clocks that are affected by the excitation light.

Studies mentioned above for single-cell analysis of the biological clock are limited by either the number of single-cells that were measured (mostly ~ 100) or the number of days (usually only ~ 3 days) during which the circadian rhythms were measured. Moreover, most of these measurements were done on cells in tissue. The cells were not spatially separated, which means they may communicate with each other. A high-throughput platform is needed for measuring the biological clock at the single-cell level. This platform should be able to isolate large numbers of single-cells into an individual microenvironment for long-term incubation. This physical isolation of single-cells prevents cells communicating with each other and is necessary when investigating whether a clock related property presents in single-cells or is an emergent phenomenon due to cell-to-cell communication. Last but not least, this platform should be able to be integrated with optical measurement for via fluorescence or luminescence in order to measure the circadian clock of single-cells.

2.2 Review of technologies for single-cell isolation and long-term measurement

For single cell analysis, the isolation of cells is necessary for further analysis because the target cells need to be identified in order to perform analysis at the single cell level. There is isolation of cells from multi cell type cultures for down stream analysis

and isolation of cells into individual microenvironments for further assay/monitoring depending on the purpose or application. Various current single cell isolation technologies were developed to meet different application requirements.

For isolating specific cells from a multi-cell type population or tissues, the techniques can be categorized into two kinds, depending on what mechanism they use. The first kind relies on physical properties of the cells, such as size, shape, electric charge, density *etc.*. The second kind of techniques is based on cellular biological/physiological characteristics, for example, specific surface markers. There are five major techniques that are extensively used to isolate cells for a single cell study[53], including limiting dilution, fluorescence active cell sorting (FACS), magnetic activated cell sorting (MACS), mechanical or laser micromanipulation, and microfluidics. Each technique has its own advantages and limitations and one may be more suitable for certain applications than others. Efficiency, purity, and recovery are the three major parameters to consider for the performance of a particular single cell isolation technique.

Limiting dilution is probably the most straight forward method to obtain single cells from a heterogeneous cell population. In this approach, serial dilution of a cell suspension is performed until only single cells remain in individual small volumes. Further analysis is usually required to confirm the obtained cells are of interest. This technique is used most in applications where a cell population is required to be grown from a single-cell. Limiting dilution is hard to scale to a high-throughput operation, and on average only about one third of the obtained volumes contain single cells.

Fluorescence active cell sorting (FACS) utilizes fluorescence associated with specific surface markers on cells of interest to select actively the cells from a heterogeneous

population. FACS is one type of flow cytometry. It starts by flowing a cell suspension driven by pressure, and the cells are then lined up one by one due to the effect called hydrodynamic focusing[53]. A laser is then used to excite the fluorescence of the cells whose emission is then detected downstream. The detected positive signal activates the sorting apparatus to select the target cells. Right before sorting happens, droplets encapsulating the cells are usually generated by vibrational activation. The droplets with target cells are then charged and deflected by electrically charged plates to the collection reservoir. FACS system can provide high-throughput single cell sorting with a rate $> 10^4$ cells/s[53]. Also it can simultaneously analyze multiple characteristics of a cell population by using different color fluorescence[54].

Magnetic activated cell sorting (MACS) uses magnetic beads to label cells of interest by conjugating enzymes, antibodies, streptavidins or lectins to the magnetic beads[55]. When a magnetic field is applied, cells labeled by magnetic beads are collected while other cells are discarded by washing steps. Compared to FACS, MACS requires a less complex detection and sorting system. However, the final purity of the isolated cells usually is compromised due to the non-specific contamination from adsorption of non-relevant cells to the capturing device or adhesion of them to a large excess of magnetic particles[55]. Also MACS can only differentiate positive and negative cells and therefore lacks of the ability to sort multiple type of cells simultaneously.

Mechanical manipulation is a manually operated approach. Micropipettes are used to pick manually a specific cell with the aid of observation under a microscope by applying suction. The selected cell is later transferred to a collection tube. The throughput

of this method is limited, and highly skilled professionals are required to operate this micromanipulation method.

Laser capture manipulation (LCM) dissociates single cells from solid tissue using highly focused laser beams. Under a microscope, the film surrounding the cell of interest are melted by the laser, and the cell is dissociated with the rest of the tissue. Then the cut cell is extracted via adhesive taps, by simply gravity, or by pressure catapulting[53]. LCM has the advantage of precisely selecting the cells while maintaining a relatively high speed. The important spatial information of the extracted single cells can be obtained directly from the cellular structure of the tissue. LCM also requires no direct contact of the cells and provides the flexibility to manipulate the cells in an enclosed chambers. However the LCM operation need to be carefully conducted so that no photodamage is introduced to the cells. Also the laser energy in LCM may introduce UV damage to DNA and RNA[56].

Microfluidic techniques have been adopted for more and more single cell analyses in recent years. This may due to the fact that microfluidic devices usually provide precise flow control, low cost, and low sample/reagent consumption[57]. Mainly four kinds of working principles are used in microfluidic techniques for cell separation: sorting cells based on their physical properties (*e.g.* size, shape, or density), cell sorting based on cell affinity due to the interaction between antigens and antibodies or ligand and receptor, cell separation based on dielectric properties of the cells, and cell sorting utilizing immunomagnetic beads[55].

Besides isolating cells of interest from a multi-cell type population, compartmentalization of single cells into a physically isolated environment is also essential for various single cells analyses. Fox example, compartmentalization could

prevent the target molecule from a cell to diffuse away and therefore allow more specific and sensitive measurements[58]. And compartmentalization sometimes can provide a stable environment for single cells with long-term incubation. Microfluidic techniques and microtechnologies are extremely powerful in terms of providing a very flexible way to manipulate the microenvironments that the cells are in and the cells too at the same time. Various microfluidic/micro-scale platforms have been designed to perform single-cell analyses[59–63]. Most of these platforms/tools can be categorized into four groups according to the microstructure used to capture single-cells: chambers[64–69], microwells/microarray[70–78], traps[79–81], and droplets[82–84]. Among these platform/tools, some were used for short-term (<~5 hours) or real-time single-cell analyses, such as PCR-based single-cell analysis[65, 66, 85, 86], observation of cell migration[67], stem cell differentiation stimulation[64], cellular products detection[78], gene screening[76], protein–protein interactions[87], *etc.*; others were used for long-term (several hours to days) single-cell incubation/studies purposes, for example, stem cell therapeutic potential[68, 88–90], drug screening[70, 82, 91], bacteria quorum sensing[83], immune response[73, 75, 76, 92, 93], bacterial antibiotic resistance[74], aging[81], cell growth[84, 94], *etc.*. Chamber-based platforms can isolate single-cells and disconnect their communication by cutting off media exchange between chambers using pneumatic solenoid valves[64] or hydrodynamic valves[93]. But the main challenge will be in scaling up these platforms for a large number of single-cells[63]. Large-scale investigation on olfactory sensory neuron (OSN) (over 20000 single OSN simultaneously) to detect rare responding OSN was demonstrated by Figueroa et al. using microwells[77]. However, cells share the same medium in the main channel above the microwells. Droplet

microfluidics as an emerging tool for single-cell analysis provides a way to isolate single-cells into an individual environment[63]. Boedicker et al. developed a microfluidic droplet platform, which can confine as few as one to three cells in a droplet and monitored initiation of quorum sensing (QS) over time (>40 h) of a hundred single-cells and small populations of clonal cells[83]. The droplets were formed by introducing an air bubble over microwells that contained a small volume of bacterial suspension. With this platform, they demonstrated that single-cells are able to initiate QS and observed high viability in QS initiation within small populations of cells (one to three cells in a droplet). Pan et al. demonstrated a simpler droplet platform using a flow-focusing method to generate droplets that encapsulate individual algal cells for long-term (up to 10 days) tracking of growth of several hundreds of individual algal cell[94]. Three different species of green microalgae were cultured in droplets. Detailed analyses of their growth were done on this platform at the single-cell level by examining the effect of nutrition concentration, pH, initial cell number per droplet and droplet volume on cell growth. Their study showed that higher final concentrations of cells were achieved when cells were grown in droplets rather than in a bulk system and revealed heterogeneity in rates of division of individual cells. Studying the biological clock usually requires a long term measurement (up to 10 days). A comparison of the advantages and disadvantages of these previous platforms suggests that droplet microfluidics can be a potential tool for observation of the biological clock on a large number of isolated single-cells.

CHAPTER 3

EXPERIMENTAL METHODS

3.1 Strains and Media

N. crassa strain, MFNC9[30] (Fungal Genetics Stock Center 10626), was used in 3% sorbose, 1 M Sorbitol, 0.0125% glucose, 0.0125% fructose, 0.3 mg/ml sodium formate, 1X Vogels Media with recommended Biotin and trace element supplements[95], as modified from Lindgren[96]. The strains *prd-4Δ,ccg-2p:mCherry* and *frqΔ,ccg-2p:mCherry* were generated by a cross between a deletion construct[97] and MFNC9 on cornmeal crossing medium[95].

3.2 Microfluidic device design and fabrication

Microfluidic droplets are discrete miniature volumes (μl to fl) of one phase in an immiscible phase. Two major geometries are widely used in microfluidic droplets generation device design: T-junction and flow-focusing. Flow-focusing strategy is believed to offer a better control over droplet formation due to it leveraging multiple parameters that affect the droplet size[98]. These parameters include the channel geometries, flow rates of the two phases, flow rate ratio of the two phases, and the viscosities of the two phases[98]. As a result, the flow-focusing geometry was chosen for the design of the microfluidic device for this thesis work. In a flow-focusing geometry, a flow that contains the phase to form droplets is introduced to a channel that is intercepted by two side channels where the other phase is flowing in to cut the center flow to form

droplets. The generating nozzle is the region that follows the intersection of the two phase and its dimension is critical for controlling droplet generation[99]. Generating nozzles with different dimensions were designed, and the optimal working design with a generating nozzle dimensions of $125 \mu\text{m} \times 50 \mu\text{m}$ (width \times depth) is shown in Figure 3.1.

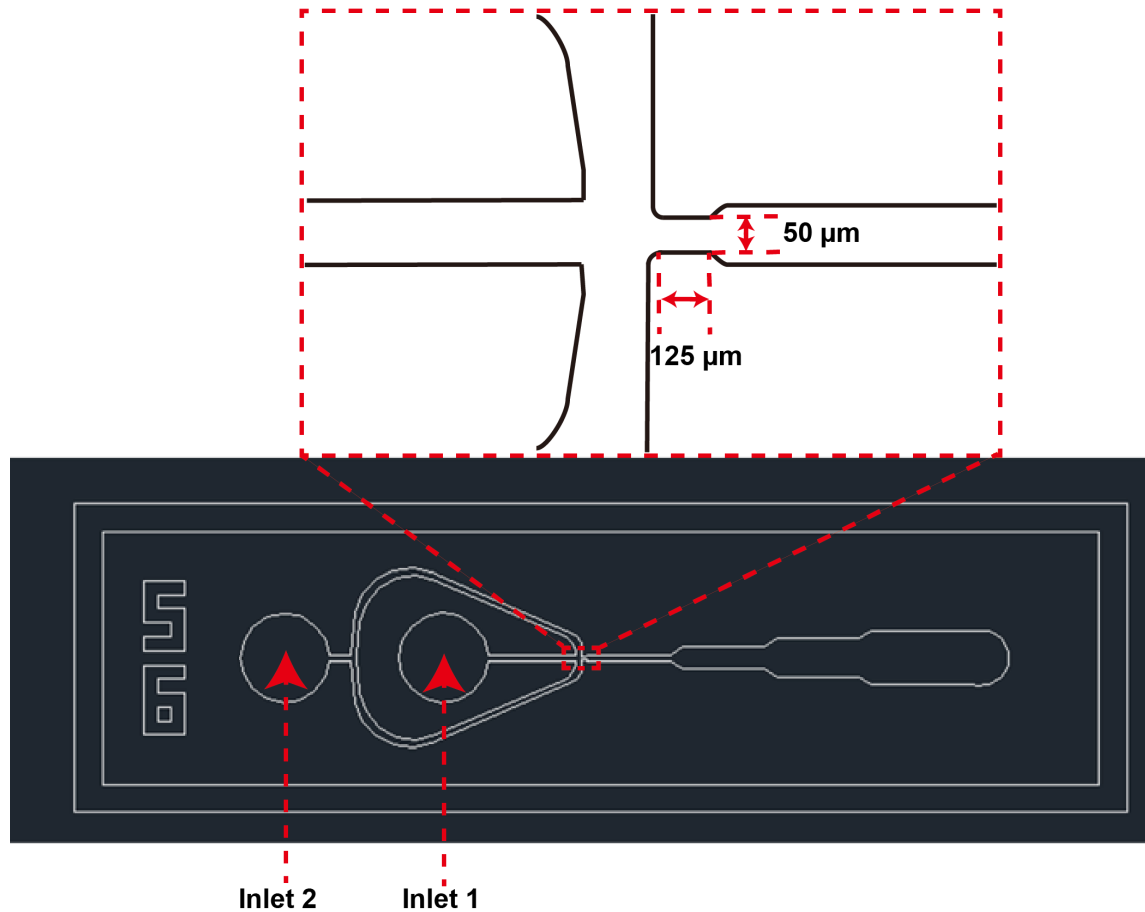


Figure 3.1: Schematics of the droplet-generating device. The generating nozzle has dimensions $125 \mu\text{m} \times 50 \mu\text{m}$ (width \times depth).

Fabrication of this prototype polydimethylsiloxane (PDMS) microfluidic device for droplets generation followed a standard soft-lithography approach[100]. The device was then attached to a glass slide. Bonding between the PDMS device and the glass slide was enhanced by putting the device in the oven under $80 \text{ }^\circ\text{C}$ for 8 hours. Treatment with

1H,1H,2H,2H-Perfluorooctyltriethoxysilane (Sigma-Aldrich, St. Louis, MO) is necessary to render the microchannel surfaces with proper hydrophobicity before use.

3.3 Droplets generation and cell encapsulation

In order to encapsulate cells in droplets, a cell suspension was injected into inlet 1 as illustrated in Figure 3.1 and a carrier oil (a mixture of fluorinated oil FC-40 with 5.0 wt% of Dolomite Surf-2 surfactant) was injected into inlet 2 as show in Figure 3.1. The cell suspension was broken up into discrete droplets near the nozzle region when the viscous shear stress overcomes the interfacial tension. As a result, droplets with cells encapsulated inside were generated as show in Figure 3.2A. The general procedure for droplet generation in this thesis work is listed as follow.

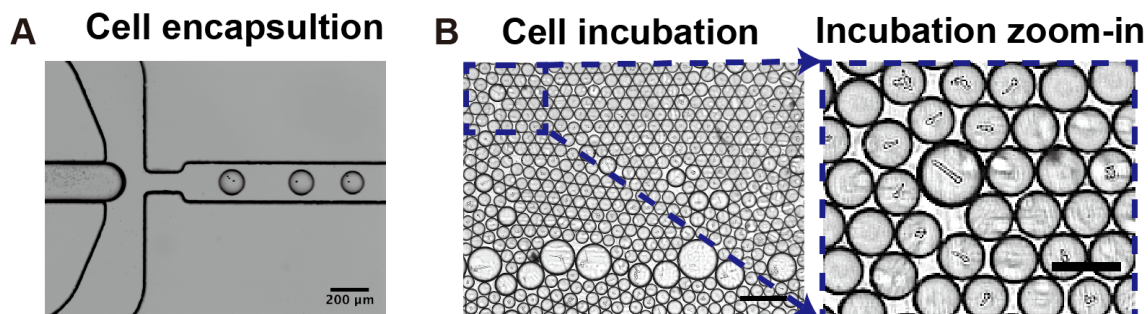


Figure 3.2: Droplet generation and cell incubation. (A) Generation of droplets. Scale bar is 200 μm . (B) A bright-field microscopy image and its zoom in image shows droplets containing *N. crassa* stored in the incubation chamber. Scale bar is 500 μm and 200 μm for the zoom-in figure.

1. Take the needed amount of the original cell suspension, growth media and Percoll(Sigma-Aldrich, St. Louis, MO) with pipette and inject them into a 1.5 mL conical tube.
2. Mix the three by putting the conical tube in the vortex mixer under a speed level of 3 for 30 seconds.

3. Insert ~ 2 cm of PE tubing into the two inlets of the device. Flush the device with DI water for the outlet to get rid of the PDMS debris.
4. Load the continuous phase into a 1 mL syringe. The continuous phase is a mixture of fluorinated oil FC-40 with 5.0 wt% of Dolomite Surf-2 surfactant. The surfactant is used to prevent droplets from coalescing.
5. Load the final cell suspension into a 1 mL syringe.
6. Connect the loaded syringes to the inlets of the devices with PE tubing and tygon tubing.
7. Put the devices onto the stage of the microscope, and secure the syringes to the slot of the syringe pump. Set the flow rate of the continuous phase to be 13 $\mu\text{L}/\text{min}$ and that of the dispersed phase to be 0.5 $\mu\text{L}/\text{min}$. and then run the syringe pump.
8. Connect the outlet of the device with a 1.5 mL conical tube using a PE tubing to collect the droplets in the conical tube.
9. After enough droplets are collected in the conical tube, use a syringe to take out the redundant carrier oil (the fluorinate oil). Then use a capillary tube to retrieve the droplets for observation by submerging one end of the capillary tube in the droplets layer in the conical tube.
10. Put the capillary tube onto a clean glass slide, and seal the tube with Epoxy glue.

The flow rates are decided by a series of experiments in order to achieve large amounts of single-cell encapsulation. That is, decent percentage of the collected droplets encapsulating one cell ($\sim 30\%$ is the highest fraction of droplets initially encapsulating one cell shown in [94]). This is for the purpose of monitoring large amounts of single-cell simultaneously. The flow rates can be adjusted to change the number of cells encapsulated in droplets and

the percentage of those droplets. Table 3.1 shows the results of these series of experiments with cell suspension flow rate as a changing parameter (Droplets were collected in capillary tubing with depth of 50 μm). When the carrier oil flow rate is 13 $\mu\text{L}/\text{min}$, cell suspension flow rate is 0.5 $\mu\text{L}/\text{min}$ and final cell concentration is 1.2×10^7 cell/mL, over 30% of the collected droplets encapsulating single-cells can be achieved.

Table 3.1: Number of cells per droplet distribution with cell suspension flow rate as a changing parameter

	Experiment 1	Experiment 2	Experiment 3	Experiment 4
Oil flow rate ($\mu\text{L}/\text{min}$)	13	13	13	13
Cell suspension flow rate ($\mu\text{L}/\text{min}$)	1	1.2	1.4	1.6
Cell concentration (cell/ml)	1.2×10^7	1.2×10^7	1.2×10^7	1.2×10^7
Total droplet number	907	887	833	506
Single-cell	303(33.41%)	227(25.29%)	211(25.33%)	72(14.23%)
Two cells per droplet	111 (12.24%)	173(19.50%)	192(22.93%)	81(16.01%)
Three cells per droplet	71 (7.83%)	77(8.68%)	80(9.60%)	42(8.30%)
\geq four cells per droplet	76 (8.38%)	147(16.57%)	139(16.69%)	196(38.74%)
Droplet with cells	561 (61.85%)	624(70.35%)	621(74.55%)	391(77.27%)

Percoll was used as a dispersant to prevent the cells from settling down in the syringe during cell encapsulation. Percoll is a registered trademark of GE Healthcare. It is a well-referenced media for density gradient centrifugation of cells, viruses, and subcellular particles[101]. Percoll is composed of colloidal silica nanoparticles coated with polyvinylpyrrolidone (PVP). It has low osmolality for extremely high cell viability and intact morphology. Downstream processes are unaffected by Percoll treatment. Different percoll concentrations was tested for the viability of *N.crassa* as shown in Table 3.2.

Table 3.2: *N.crass* cell viability after incubated in the media with different concentrations of Percoll for 6 days

Percoll concentration (v/v)	Viability
0%	84%
1%	85%
5%	83.1%
10%	82.5%
15%	85.6%
20%	81.5%

Percoll also has the effect of restricting cell movement and hence facilitates the tracking of cells later on during image processing. The moving distance of cells between sampling time points was calculated for experiments used different concentrations of percoll. Figure 3.3 shows the results of the moving distance of cells between sampling time points affected by the percoll concentration. The movement of the cells does not

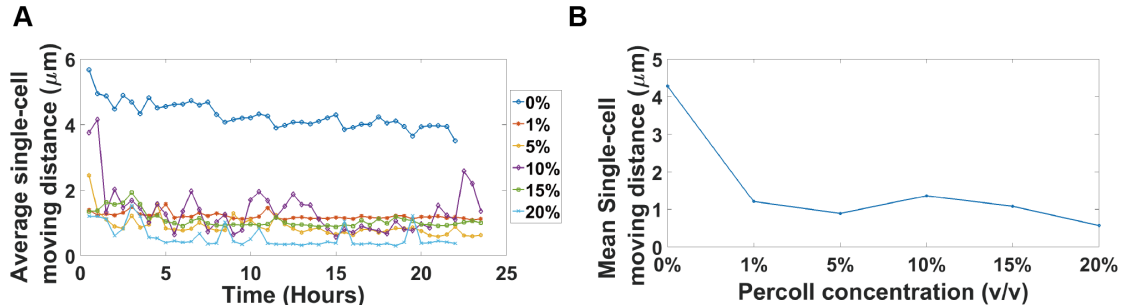


Figure 3.3: Percoll stabilizes the cell movement. (A) Single-cell moving distance between time frames (a 30 minutes interval) over time. (B) Single-cell moving distance between time frames average overtime and cells as a function of percoll concentration.

change too much overtime. However, as the percoll concentration increases, the movement of the cells is reduced. When the percoll concentration is 5% (v/v), the moving distance is reduced to a very low value, 0.887 μm , closed to that when percoll concentration is 20% (v/v). Meanwhile, percoll could bring an adverse effect on the stabilization of the droplets,

causing the droplets to coalesce since percoll may affect the surfactant used to prevent droplets from coalescing. Therefore as less as percoll should be used in order to maintain the uniformity of the droplet size. In order to choose the optimum concentration of percoll, the droplet size was calculated for experiments using different concentrations of percoll, and the results are summarized in Table 3.3. Without percoll added to the droplets, the standard deviation of the droplet size is the smallest. As percoll concentration increased, the standard deviation of the droplet size increase very slightly. Based on these results, 5% (v/v) percoll was chosen for later experiments.

Table 3.3: Droplet size distributions when using different concentrations of percoll

Percoll concentration (v/v)	Mean (μm)	Std (μm)	Min (μm)	Max (μm)
0%	77.4336	9.0601	51.816	179.5953
1%	78.0317	14.8222	51.6075	316.0851
5%	74.1416	15.0417	51.6075	348.1067
10%	77.7925	22.2272	51.628	381.4085
15%	81.0532	17.8227	51.6075	316.0918
20%	75.4457	16.9823	51.628	275.6372

3.4 Time-lapse imaging

Before fluorescence time-lapse imaging, the cells encapsulated in droplets were put under a LED white light source (color temperature 6500K) for 26 hours. This is to synchronize the clock of the individual cells. Since the excitation and emission wavelength for mCherry protein is ~ 580 nm and ~ 610 nm, Carl Zeiss filter Set 43 HE was used. To reduce photobleaching, a short exposure time was used for imaging. The procedures for the long-term time lapse-image recording for this thesis work is as follow:

1. Choose the objective with magnification to be used. See detail in section 3.7

2. Use the ‘Mark and find’ module in the software AxioVision (Carl Zeiss Microscopy, LLC, Thornwood, NY) to generate the positions list of the field of views of the capillary tubing.
3. Take white field images of each field of view for automatic cells grouping in the the image analysis procedure.
4. Turn on the mercury lamp and the shutter controller. The intensity level of the lamp should be tuned to get a fluorescence image with good quality.
5. Follow the procedures described in the “Correction of CCD Image Imperfections” in the Image processing section below to take images needed for the correction.
6. Set the exposure time to be fixed in the multidimensional experiment panel for the time-lapse experiment.
7. Set the interval between taking consecutive images to be 30 minutes.
8. Set the total number of the time-lapse images to be taken.
9. Set the shutter to be opened before each image taking time point and closed after each image taking a time point.
10. Start the time-lapse experiment.
11. Save all the images into 16bit tiff format.

3.5 Correction of CCD image imperfections

Correcting the obtained fluorescence images for imperfections in the CCD detector is important for the goal of providing an image that is the closest match to the specimen[102]. Generally, the procedures are as follows:

1. Dark current correction: Take a couple of images with the same exposure time as the time-lapse experiment before each experiment but with the shutter closed. Average these images to create a dark current image. Subtract each fluorescence image by the dark current image.
2. Bias correction: Take a couple of images with zero exposure time and with the shutter closed. Average these images to create a bias image. Subtract each fluorescence image (corrected for dark current) by the bias image.
3. Flat field correction: Take a couple of images with quite short exposure time of uniformly illuminated screen/field of view (For example, a commercial green luminescent liquid in a 35 mm culture dish is suggested in [102]). Average these images to create a flat field image. Obtain the average pixel value within the (dark/bias corrected) flat field image (call it α). Then, for each fluorescence image (dark/bias corrected), multiply all pixels by α and then divide (pixelwise) by the flat field image. Flat field image should be created each time, changing optical properties of the illumination and lens system. For example, use different flat field image for different magnification.

3.6 Image processing

A Matlab routine was developed to sort droplets according to the number of cells in them and to track the fluorescence intensity of individual cell frame by frame. Locations of cells are determined by finding a local maximum in fluorescence intensity. The sorting is based on the difference of distance between cells and droplet and the radius of the droplet. The tracking is mainly based on the minimum distance between cells in consecutive frames.

The quality control filter to filter out cells that are not linked properly is based on comparing values of the extracted fluorescence intensity in consecutive time for one cell and between cells. The quality control filter marks the cells that are not linked properly as bad cells and they are not considered later in the analysis.

The fluorescence images are shown in Figure 3.4. Different numbers of cells were encapsulated in droplets. Figure 3.4A-D are images taken at 0 hours, 50 hours, 100 hours, and 150 hours. The droplets are very stable as no movement and merging of the droplets are seen, which facilitates the tracking of cells. The cells grouping based on how many neighboring cells they have in their droplets is shown in Figure 3.5. For example, single-cells are those alone in their droplets in Figure 3.5A. 3 cells per droplet, 6 cells per droplet, and 12 cells per droplet are shown in Figure 3.5B, C, and D. The lines with a '+' end point to the cells they track through the time-lapse. Tracking at 0 hours, 50 hours, 100 hours and 150 hours is shown here. Figure 3.5D shows the 9 cells that are successfully tracked in a 12 cells droplet since that cells that are not properly tracked are excluded from later analysis.

3.7 Control experiments for choosing objective magnification

The magnification of the objective is a parameter that should be optimized for the purpose of improving the accuracy of the results and getting enough data points (large amount of cells monitored) at the same time. Collection of photons by the objective lens must be maximized. It is critical to use a lens with high light gathering power (*LGP*), which depends on numerical aperture (*NA*), magnification (*Mag*), and the mode

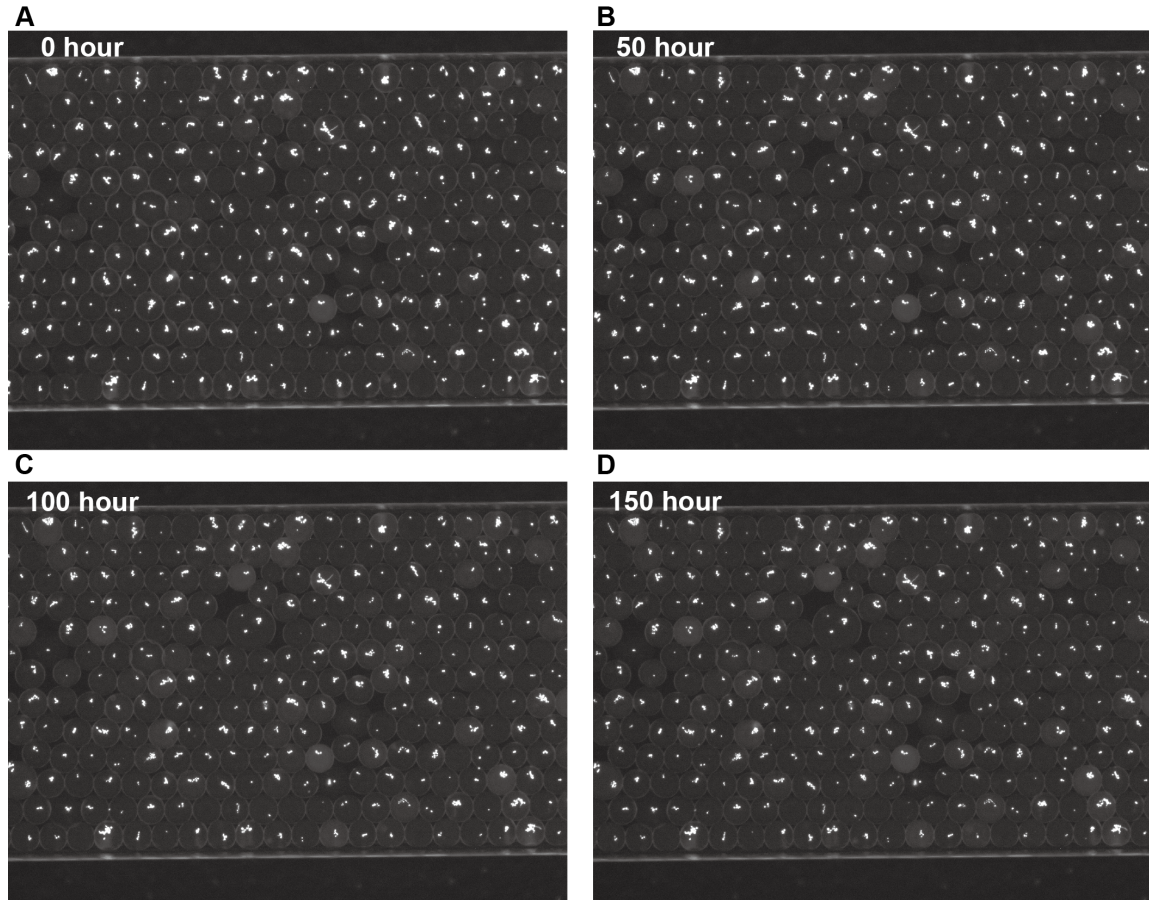


Figure 3.4: Droplets are very stable during time-lapse imaging. Fluorescence images showing cells encapsulated in droplets at 0 hours(A), 50 hours(B), 100 hours(C), and 150 hours(D)

of illumination[102] as show in Equation 3.1 or Equation 3.2:

$$LGP_{\text{for epifluorescence}} = (NA^2/Mag)^2 \times 10^4 \quad (3.1)$$

$$LGP_{\text{for luminescence}} = (NA/Mag)^2 \times 10^4 \quad (3.2)$$

Table 3.4 shows the (LGP) objective lens installed in the microscope.

Table 3.4 shows that 50X magnification has a high LGP , and it is the largest magnification that will provide high resolution. However, with 50X magnification, the number of cells can be observed in one field of view will be only a few. That is, there is a trade off between high resolution and number of cells that can be monitored. Therefore,

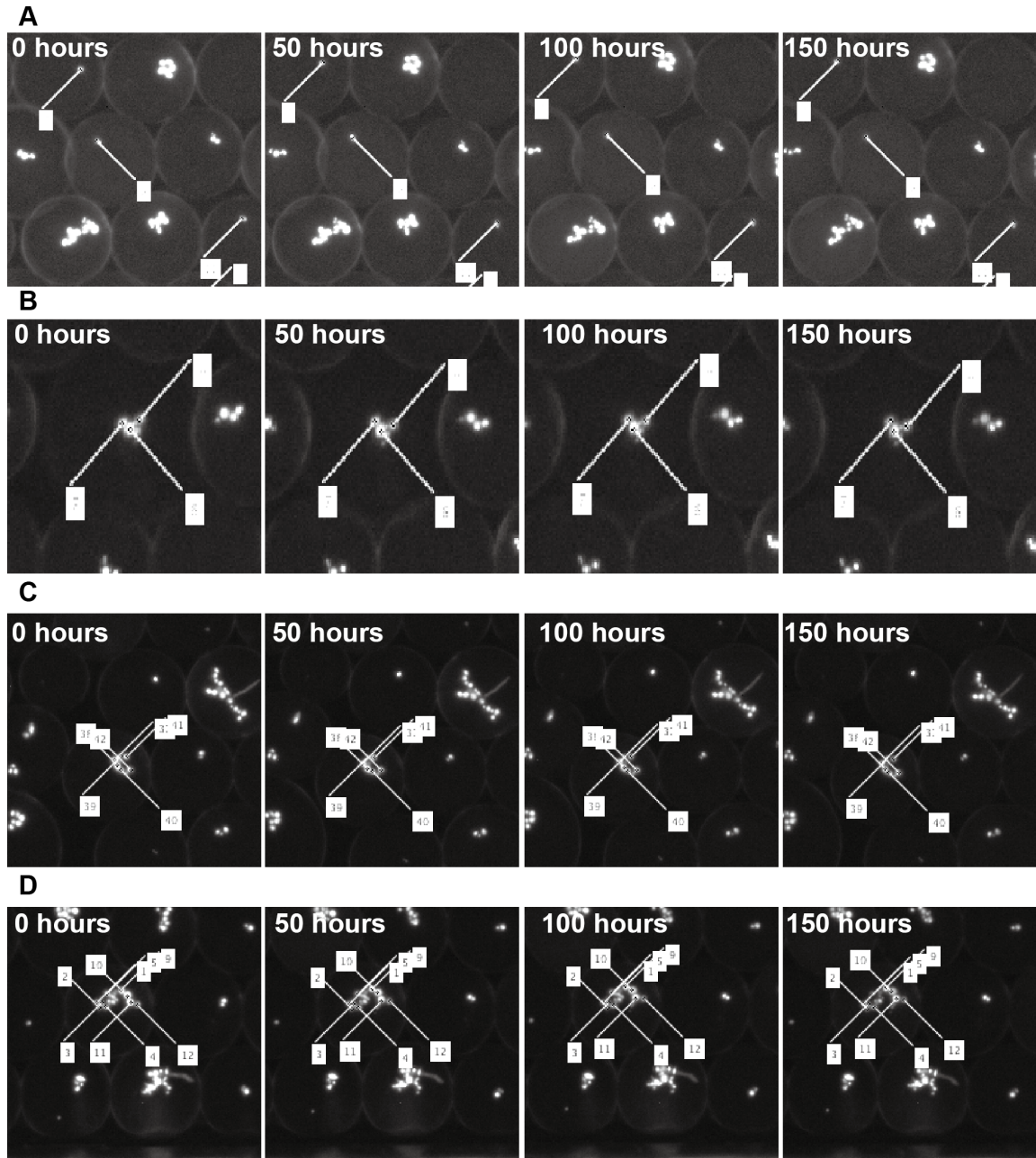


Figure 3.5: Cell grouping and tracking. Cells were grouped based on how many neighboring cells they have in the corresponding droplets. Single-cells are those with 0 neighboring cells and only 1 cell in each droplet(A), 3 cells per droplet with each cell has 2 neighboring cells(B), 6 cells per droplet (C), and 12 cells per droplet(D). The lines with a '+' end points to the cells they track through the time-lapse. Tracking at 0 hours, 50 hours, 100 hours and 150 hours is shown here.

Table 3.4: *LGP* for objective lens with different magnifications

NA	MAG	LGP
0.16	5	0.262144
0.25	10	0.390625
0.22	20	0.058564
0.55	50	0.366025

a control experiment was done to choose a reasonable lower magnification so that large numbers of cells can be observed at the same time without compromising the accuracy. This control experiment was conducted by measuring the same 62 single-cells in droplets under different magnification: 5X, 10X, 20X, and 50X for 4 days. At each time point, the objective magnification was changed manually and the fluorescence images were taken under the four different objective magnifications for the same 62 cells. The fluorescence intensity time series for the 62 cells measured under different objective magnifications are shown in Figure 3.6. Considering 50X magnification as the standard, the coefficient of determination, R-square, was calculated by fitting a linear regression on the fluorescence intensity of the cells measured under 50X, as the dependent variable, against that measured under the lower magnifications, 5X, 10X, and 20X, as the independent variable. The histograms of the R-square for the 62 cells under 5X, 10X, and 20X are shown in Figure 3.7. The R-square values are also summarized in Table 3.5. The average of the R-square values of all the cells for all the magnifications are over 0.8, which means over 80% of the variation measured under 50X magnification is predictable from the data measured under the lower magnifications. This means measuring under 5X, 10X, or 20X will give us as good accuracy as measuring under 50X. Therefore, 5X magnification was chosen for all the experiments (unless stated otherwise) for this dissertation for the purpose of monitoring as many cells as possible.

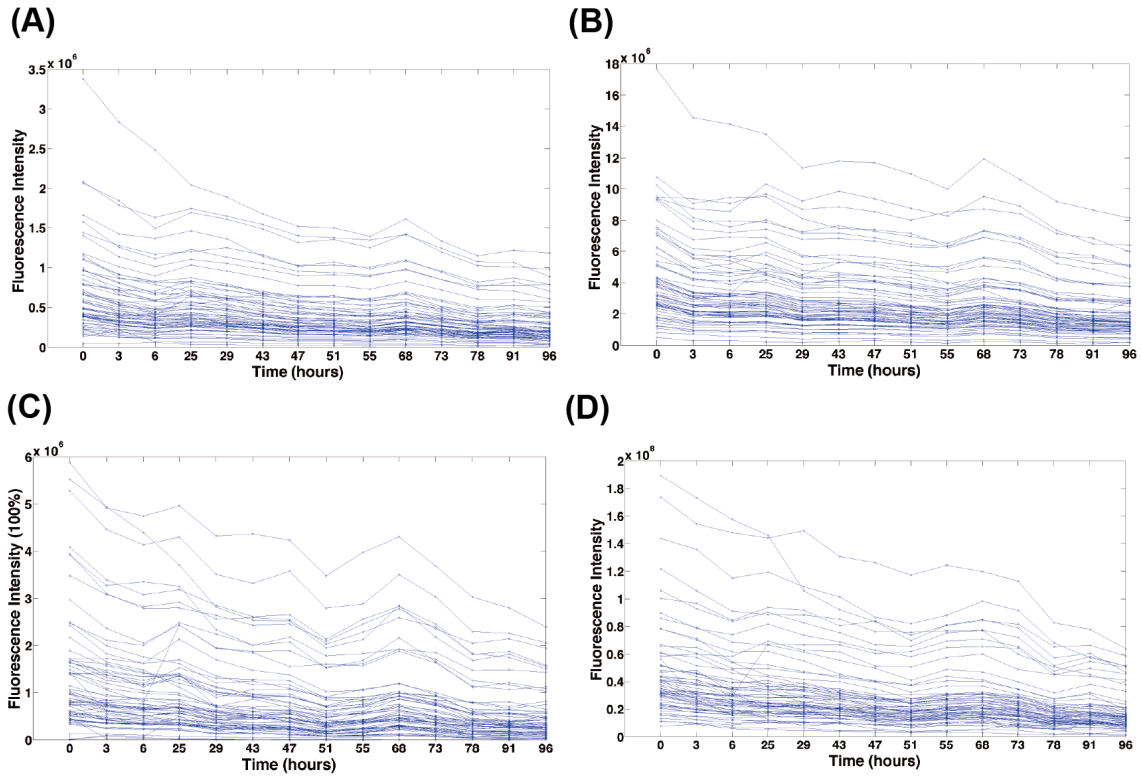


Figure 3.6: 62 single-cell fluorescence intensity time series under different magnifications. (A)5X. (B)10X. (C)20X. (D)50X.

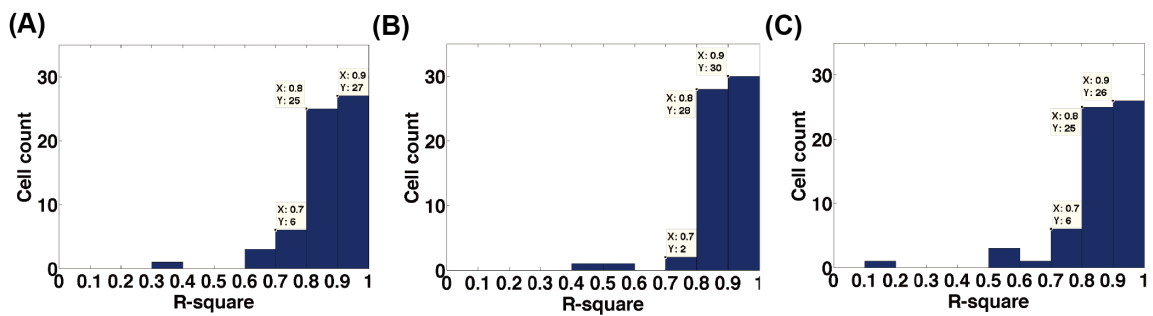


Figure 3.7: Coefficient of determination, R-square, was calculated by fitting linear regression on the fluorescence intensity of the cells measured under the lower magnifications, 5X, 10X, and 20X, against that measured under 50X. (A)5X. (B)10X. (C)20X.

Table 3.5: R-square under different magnifications

Magnification	Average R-square for 62 cells	Number of cells with R-square over 0.8
5X	0.8643	52
10X	0.8814	58
20X	0.8552	51

3.8 Data analysis

All of the cell fluorescence intensity time series are divided by a Rhodamine B intensity time series measured concurrently with the cell. This Rhodamine B normalization step is for the purpose of correcting for fluctuations in the microscope's excitation intensity. The first 30 hours of data are excluded from the timeseries for later analysis due to the biological clock needing a certain amount of time to run into a stable limit cycle after the cells are transferred to the dark from light. A 24-hour moving average detrending method was applied to remove any nonstationarities on large time scales (*e.g.* photobleaching of the fluorescence protein)[103].

Additional controls were done to examine a set of time lapse images for detecting germination, fusion of cells, and cell division. ~200 single-cells were monitored for their surface area over time for germination and cell division (10 are shown in Figure 3.8A). In addition, ~200 random pairs of cells were tracked over time to see if there was any change in distance between them that might be evidence of cell fusion (10 are shown in Figure 3.8B). No obvious surface area and cell to cell distance changes were seen, suggesting that there is no germination, cell fusion and cell division happening.

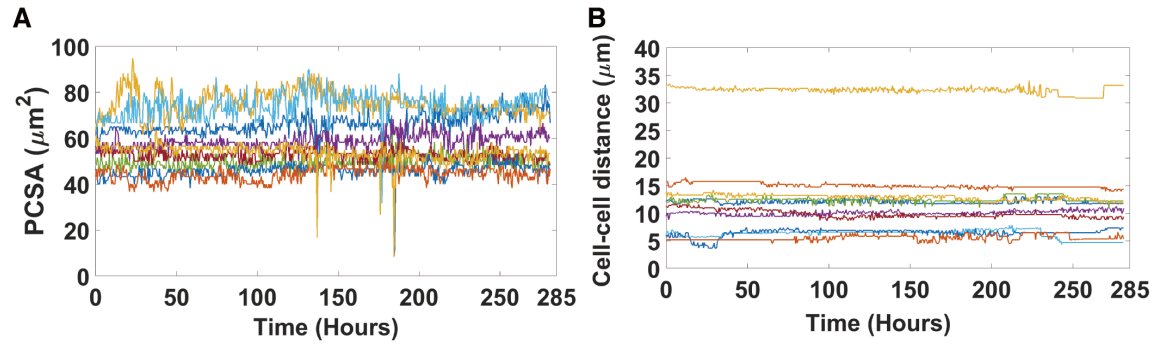


Figure 3.8: No change in Projected Cell Surface Area (PCSA) indicates no germination, and no change in cell-to-cell distance indicates no cell fusion. (A) For 10 randomly chosen cells PCSA is followed over 285 h. (B) For 10 randomly chosen cells cell-to-cell distance is tracked over 285 h. Each of these 10 cells and 10 cell pairs were drawn randomly from a larger random sample of 200 cells or cell pairs that were examined.

3.9 Experimental noise calibration with fluorescence beads

It is necessary to quantify the noise from the experimental detection process as compared to the stochastic intracellular noise. There are six sources of detection randomness in single cell measurements that are associated with the fluorescent signal generation and detection from a cell, as follows:

1. the quantum randomness of fluorescent photon generation in the cell;
2. the cell's random focal plane excursions;
3. the quantum randomness of photo-electron generation in the CCD camera;
4. CCD random pixel-to-pixel variations in each pixel's photon-to- electron conversion yield;
5. CCD image pixel summation;
6. CCD bias and dark current subtraction.

The detection noise variance is dependent on the input signal to the CCD camera and it is estimated by a simple quadratic relation with the CCD output signal, $\tilde{S}_k(t_j)$,

measured from the cells at time t_j :

$$(\sigma_{\xi,j})^2 = \frac{1}{1+B} [C + A \langle \tilde{S}_k(t_j) \rangle_{e,c} + B \langle (\tilde{S}_k^2(t_j))^2 \rangle_{e,c}] \quad (3.3)$$

and $\langle \tilde{S}_k(t_j) \rangle_{e,c}$, $\langle (\tilde{S}_k^2(t_j))^2 \rangle_{e,c}$ is calculated by sample average of all the cells' fluorescence intensity at each time point t_j as follow:

$$\langle \tilde{S}_k(t_j) \rangle_{e,c} \cong \frac{1}{K} \sum_{k=1}^K \tilde{S}_k(t_j) \quad (3.4)$$

$$\langle (\tilde{S}_k^2(t_j))^2 \rangle_{e,c} \cong \frac{1}{K} \sum_{k=1}^K (\tilde{S}_k(t_j))^2 \quad (3.5)$$

The parameters, A , B , and C in Equation 3.3 can be estimated by fitting a quadratic function as shown in Equation 3.6 to the fluorescent beads data measured in six bead experiments and by Equation 3.7.

$$(\sigma_{\eta,j}^{(b)})^2 = C^{(b)} + A^{(b)} S^{(b)}(t_j^{(b)}) + B^{(b)} (S^{(b)}(t_j^{(b)}))^2 \quad (3.6)$$

$$A = A^{(b)}, C = C^{(b)}, B = \frac{B^{(b)} - \sigma_B^2}{1 + \sigma_B^2} \quad (3.7)$$

In Equation 3.6, $(\sigma_{\eta,j}^{(b)})^2$ is estimated from the variance of the beads fluorescence intensity at time t_j , $S^{(b)}(t_j^{(b)})$ is estimated from the sample mean of the beads fluorescence intensity at time t_j . σ_B^2 is the relative variance of the emitted fluorescent photon count per bead, due to bead size variability only, in the absence of any detection noise and can be estimated by reasonable constraints[104]. Six bead experiments were done by replacing droplet-encapsulated cells with a nearly mono-dispersed sample of small, droplet-encapsulated, fluorescent beads. The beads were polymer microspheres internally doped with fluorescent dye, (Bangs Laboratories, Inc., Cat. Code: FS06F, Envy Green,

Excitation/Emission:525 nm/565 nm), with mean diameter 9.94 μm and diameter standard deviation 0.76 μm , as provided by the manufacturer. The exposure times of the CCD camera for each of the six bead experiments was different so that the mean fluorescence intensity of the beads read out by the CCD spanned over a range that covered that of the cells. Figure 3.9 shows a plot of $(\sigma_{\eta,j}^{(b)})^2$ vs. $S^{(b)}(t_j^{(b)})$ for the six bead experiments and its quadratic fit. The detection noise variance estimated from Equation 3.3 can then

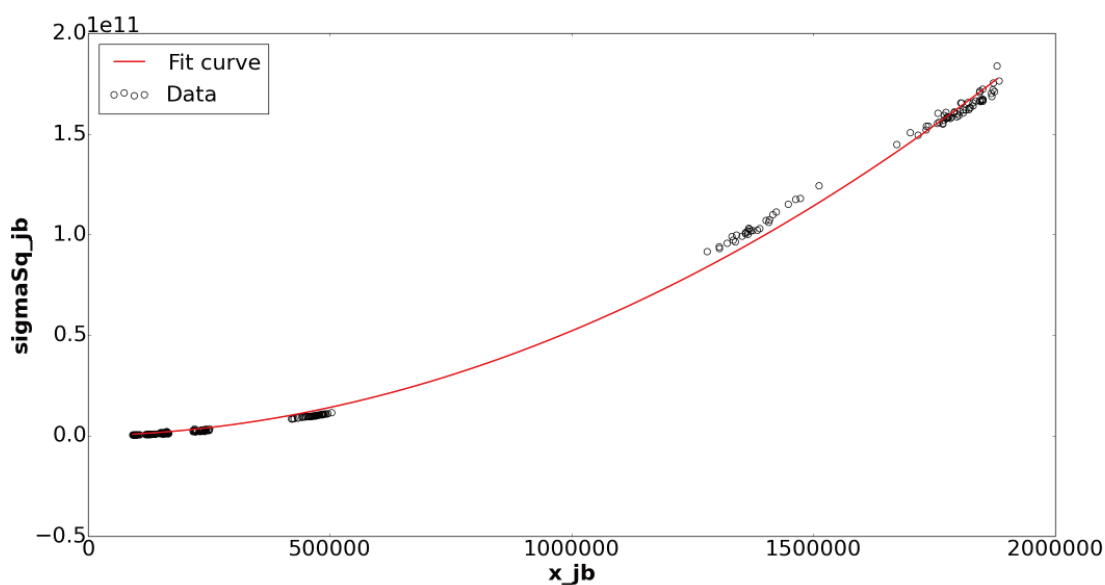


Figure 3.9: The bead signal variance $(\sigma_{\eta,j}^{(b)})^2$ varies quadratically with the mean bead fluorescence signal, $S^{(b)}(t_j^{(b)})$ in the six-experiment bead data set. The fitted red curve is the best fit to the data, subject to the positive constraints $A(b) \geq 0$, $B(b) \geq 0$, and $C(b) \geq 0$.

be used to calculate the contribution from the detection noise to the variance of average of the periodogram of cells (calculated from Rhodamine B-normalized and detrended cell fluorescence time series) at frequency f_l as in Equation 3.8[104], the propagation of detection noise to the periodogram of single-cell measurement:

$$(\sigma_l^e)^2 = \frac{2\sigma_\epsilon^2}{KL} [\langle \tilde{Q}(f_l) \rangle_{e,c} \gamma_Q(l) + \text{Re}(\langle \tilde{R}(f_l) \rangle_{e,c} \beta_Q(l)^*)] - \frac{\sigma_\epsilon^4}{KL^2} [|\gamma_Q(l)|^2 + |\beta_Q(l)|^2] \quad (3.8)$$

Where K and L are number of cells and number of time points in the fluorescence time series. $\langle \tilde{Q}(f_l) \rangle_{e,c}$ and $\langle \tilde{R}(f_l) \rangle_{e,c}$, are, respectively, the population means of average periodogram and average squared Fourier transform of the Rhodamine B-normalized and detrended cell fluorescence time series. $\gamma_Q(l)$ and $\beta_Q(l)$ are determined by functions of weights used in the 24-hours moving average detrending process[105] and the detection noise variance. σ_ϵ^2 is the variance of the Rhodamine B-normalized fluorescence time series due to detection noise averaged over all cells and time points as shown in Equation 3.9.

$$\sigma_\epsilon^2 = \frac{1}{L} \sum_{j=1}^L \sigma_{\epsilon,j}^2, \sigma_{\epsilon,j}^2 = \frac{\sigma_{\xi,j}^2}{(Z(t_j))^2} \quad (3.9)$$

Where $Z(t_j)$ is fluorescence intensity of Rhodamine B at time point t_j . $\sigma_{\xi,j}^2$ is the detection noise variance in Equation 3.3.

The total variance in the Rhodamine B-normalized and detrended series, $(\sigma_l)^2$, was estimated by bootstrapping 5000 times, the $K = 1591$ cell trajectories, from the replicate experiment in Figure 5.5A. The stochastic intracellular variance, $(\sigma_l^c)^2$, was obtained by subtraction, using $(\sigma_l^c)^2 = (\sigma_l)^2 - (\sigma_\epsilon^c)^2$. The proportion of variation in a cell oscillator fluorescent signal attributable to detector noise (i.e., experimental error) was then: $(\sigma_\epsilon^c)^2 / (\sigma_l)^2 < 6\%$ for all frequencies f_i [104].

The detection noise variance also introduce a bias into the average periodogram of the cells. The bias is obtained as:

$$Q^{bias}(f_l) = \frac{\sigma_\epsilon^2}{L} \gamma_Q(l) \quad (3.10)$$

3.10 Temperature stability verification of the measuring setup

A thermal stage was used to maintain the temperature of the cells experienced in temperature compensation experiments. The capillary tubing encapsulated with cells

(in droplets) was put directly onto the thermal stage. The temperature stability of the thermal stage was first verified to confirm that the temperature was maintained at the set temperature during each temperature compensation experiment. A thermal coupling was used to measure the temperature within the capillary tubing where the cell sample or the Rhodamine B solution is held. Figure 3.10A shows the temperature within the capillary tubing (red curve, T_s) and Room temperature (blue curve, T_R) where the thermal stage was exposed to. Although the Room temperature (blue curve, T_R) fluctuated about 4 °C, the temperature inside the capillary tubing (red curve, T_s) was very stable with a fluctuation less than 0.2 °C around the set temperature. This is confirmed also by the weak linear relationship between ΔT_s and $T_{SN} - T_R$ with a slope of 0.014 as shown in Figure 3.10B. ΔT_s is the temperature difference between the set temperature of the stage ($T_{SN} = 25^\circ\text{C}$) and the actual temperature in the capillary tubing (T_s).

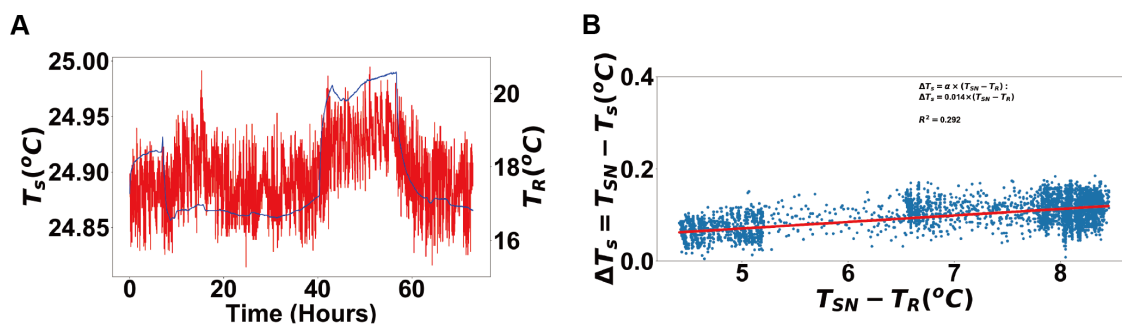


Figure 3.10: Temperature stability of the thermal stage. (A) Temperature within the capillary tubing (red curve, T_s) and Room temperature (blue curve, T_R) where the thermal stage was exposed to. (B) The difference (ΔT_s) between the set temperature of the stage ($T_{SN} = 25^\circ\text{C}$) and the actual temperature in the capillary tubing (T_s) as a function of the difference between the set temperature of the stage ($T_{SN} = 25^\circ\text{C}$) and the Room temperature (T_R). Blue dots are the data and red straight line is the linear regression.

After confirming that the temperature inside the capillary tubing is stable, a large fluctuation ($\sim 10\%$) in the Rhodamine B (RB) was still observed, and the fluctuation correlates with the Room temperature measured concurrently as show in Figure 3.11. As mentioned in chapter 3 section section 3.8, the Rhodamine B intensity was used as a standard to eliminate the variations in the illumination from the light source. The Rhodamine B intensity has been known for having high temperature sensitivity[106–108]. Since the thermal stage temperature fluctuates only $0.2\text{ }^{\circ}\text{C}$, according to the literature [106–108] that reported the Rhodamine B intensity temperature coefficient, the Rhodmine B intensity change due to this thermal stage temperature fluctuation will only be 0.1% . On the other hand, the output intensity of the LED light source used to illuminate the fluorescence protein in the cells is also temperature sensitive[109, 110]. Since the Room temperature fluctuated about $4\text{ }^{\circ}\text{C}$ (Figure 3.11A), which could cause the output of the LED light source to fluctuate accordingly hence the Rhodamine B intensity measured also would fluctuates with high correlation to the Room temperature(Figure 3.11B). Therefore, a control experiment was done by only measuring the output of the LED light source to see whether it correlates to the change in the Room temperature and whether the amount of change matches that in Figure 3.11A, that is 1.84% per $1\text{ }^{\circ}\text{C}$ (Figure 3.12A). The LED light source output was measured by imaging an empty capillary tubing under the same experimental set up for measuring the cells and Rhodamine B. The result is shown in Figure 3.12B with the orange curve in the right y axis showing the LED output intensity (normalized by the maximum intensity in the time series) and the blue curve in the left y axis showing the Room temperature measured concurrently. The fluctuation of the LED output intensity is 1.11% per $1\text{ }^{\circ}\text{C}$ which matches the change amount seen in the Rhodamine B

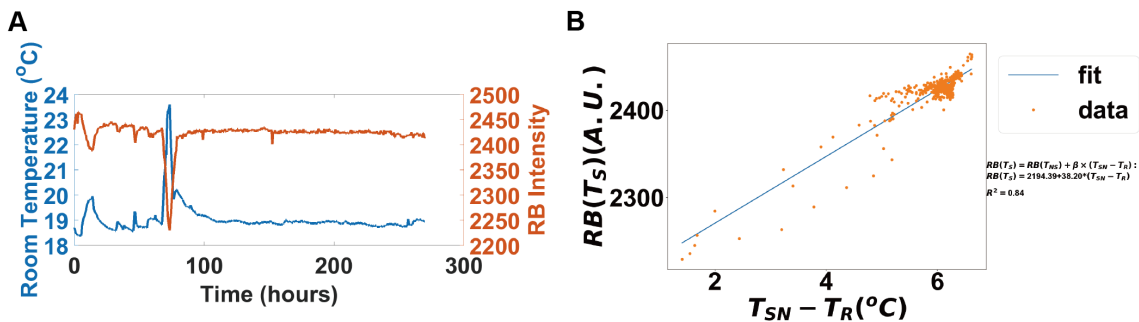


Figure 3.11: Rhodamine B intensity correlates with room temperature. (A) Time series of Room temperature (blue curve, left y axis) and Rhodamine B intensity (orange curve, right y axis) measured when the thermal stage was set at 25 °C. (B) Linear regression between Rhodamine B intensity ($RB(T_s)$) and the difference between stage set temperature (T_{SN}) and Room temperature (T_R)

intensity in Figure 3.12A. The conclusion is that the correlation between the Rhodamine B intensity and the Room temperature is due to the fact that the output intensity of the LED

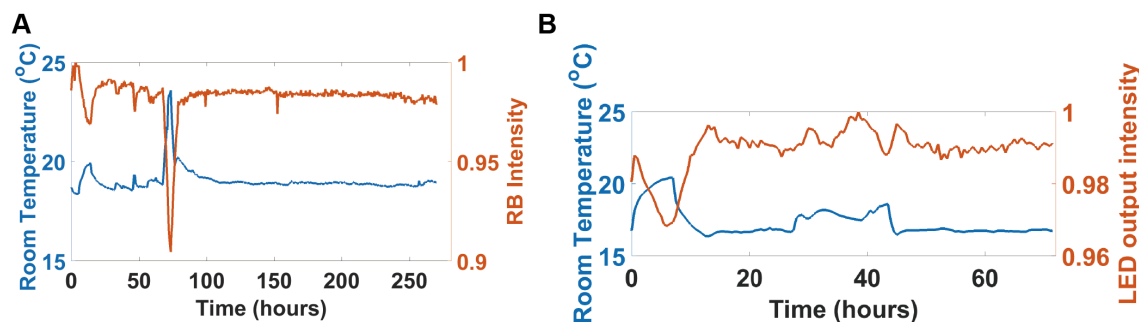


Figure 3.12: LED light source output correlates with room temperature. (A) Time series of Room temperature (blue curve, left y axis) and Rhodamine B intensity (orange curve, right y axis) measured when the thermal stage was set at 25 °C. Rhodamine B intensity is normalized by the maximum intensity in the time series. (B) Time series of Room temperature (blue curve, left y axis) and LED light source output (orange curve, right y axis) measured when the thermal stage was set at 25 °C. LED light source output is normalized by the maximum intensity in the time series.

light source is affected by the Room temperature. Therefore the Rhodamine B intensity can be used as a standard to eliminate any variations come from the LED light source including

that due to the Room temperature fluctuation and that due to any other reasons that may cause instability in the LED light source intensity output.

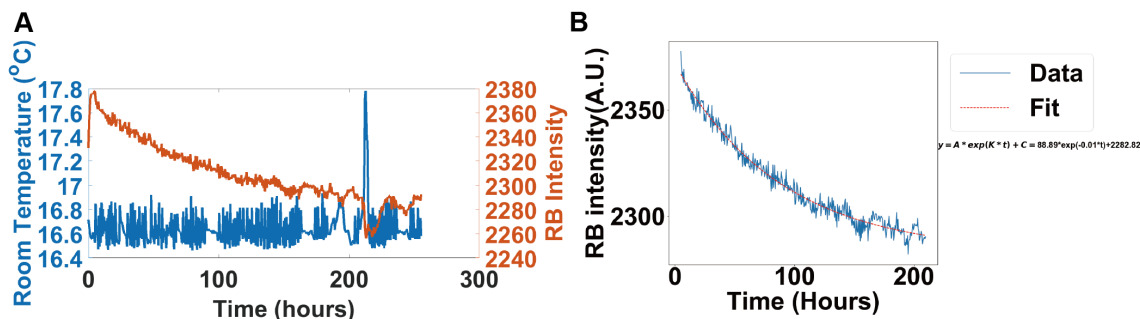


Figure 3.13: Photobleaching decay in the Rhodamine B intensity. (A) Time series of Room temperature (blue curve, left y axis) and Rhodamine B intensity (orange curve, right y axis) measured when the thermal stage was set at 30 °C. (B) Exponential fit of the Rhodamine B data from (A) in the Room temperature stable range. Blue curve is the experimental Rhodamine B data and the red dashed line is the exponential fit of blue curve.

However we are also concerned that the photobleaching decay (Figure 3.13A) in the Rhodamine B intensity will affect the results if it is used directly to normalize the cell data. Figure 3.13A shows the Rhodamine B fluorescence intensity measured when the thermal stage is set at 30 °C and the Room temperature measured concurrently is relatively stable. Here an obvious exponential decay trend due to photobleaching is shown in the Rhodamine B intensity time series. An exponential function is used to fit the Rhodamine B intensity data in Figure 3.13B and the resulting function, Equation 3.11, is used to detrend the Rhodamine B data to eliminate the effect introduced by photobleaching of the Rhodamine B dye. To detrend the Rhodamine B data, each data point in the Rhodamine B intensity time series is divided by the value calculated by Equation 3.11 at the same time point. The detrended Rhodamine B time series are shown in Figure 3.14A-E orange curves for different temperature compensation experiments and the exponential trend due

to photobleaching is diminished after detrending. The detrended Rhodamine B intensity time series were then used to normalize cell fluorescence intensity data.

$$y = A * \exp(K * t) + C = 88.89 * \exp(-0.01 * t) + 2282.82 \quad (3.11)$$

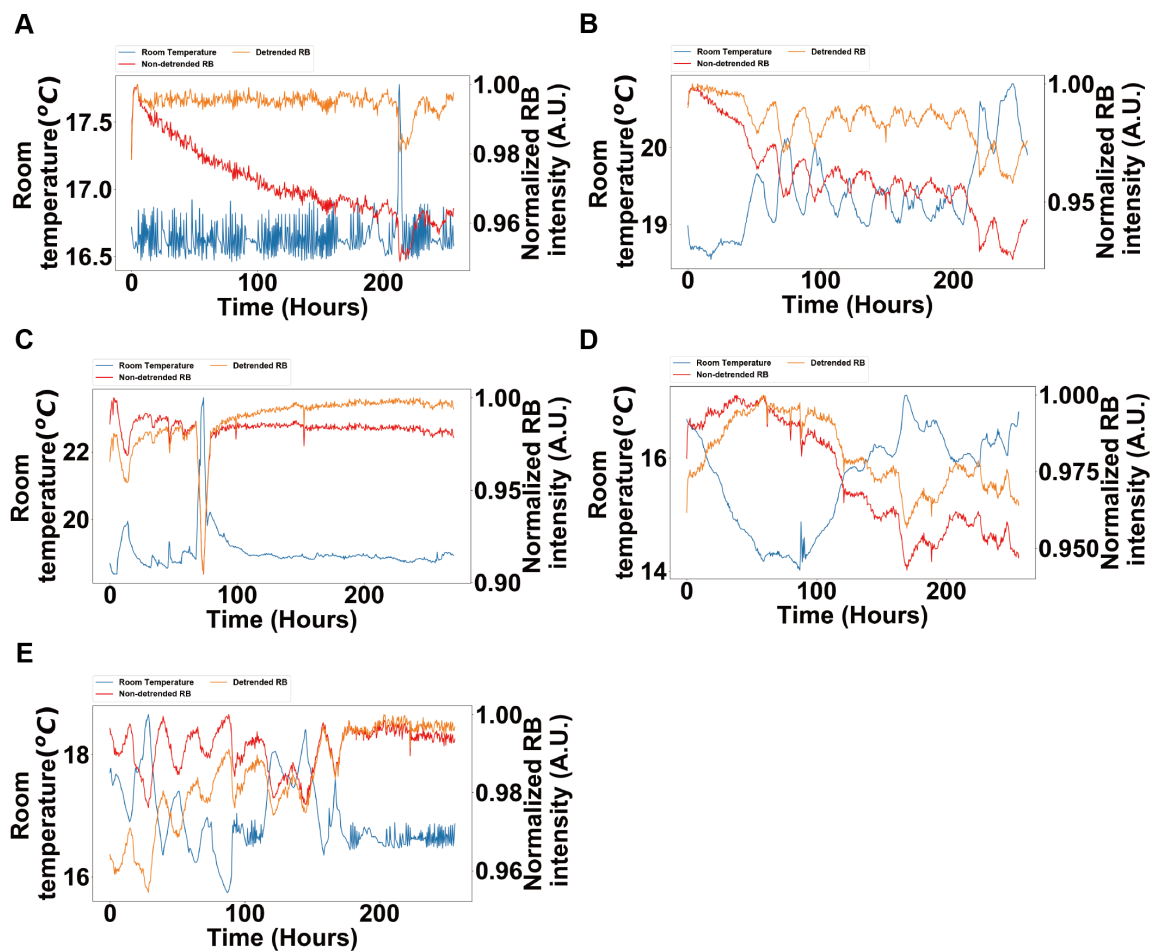


Figure 3.14: Detrended Rhodamine B time series for temperature compensation experiments. (A), (B), (C), (D), and (E) are Non-detrended Rhodamine B intensity (red curve, right y axis), detrended Rhodamine B intensity (orange curve, right y axis), and Room temperature (blue curve, left y axis) for the temperature compensation experiment at 30 °C, 27 °C, 25 °C, 22 °C, 20 °C. Rhodamine B intensity time series are normalized by the maximum intensity in each time series.

CHAPTER 4

SINGLE-CELL CIRCADIAN OSCILLATORS IN *NEUROSPORA CRASSA*

While the biological clock is a universal mechanism used by a variety of organisms(*e.g.*, animals, plants, fungi and bacteria) to tell time in constant or a changing environment (in terms of changing of light or temperature)[21], whether a single-cell has a biological clock to do so has yet to be investigated. An even more fundamental question is whether a single-cell has a circadian oscillator is the first step for finding out the answer for whether or not a single-cell has a biological clock. This answer will facilitate answering more challenging questions like, does the biological clock of individual cell communicate with each other; what mechanism they use to communicate if so; and how the biological clock in single cells synchronize with each other to achieve a deterministic clock ticking precisely as seen in organisms. On the technology aspect, measurement of the biological clock at the single-cell level and control of the micro-environment that the cells are in could bring new possibilities to investigate these above topics. While single cell measurements have been made on the clocks of cyanobacterial cells[23] and on synthetic oscillators in *E. coli* by microfluidics[111], such measurements have been rare on a eukaryotic clock, but when performed, have uncovered new phenomena about the clock[112, 113]. Some initial synchronization studies have been conducted in tissue culture of neuronal cells from the suprachiasmatic nucleus (SCN) constituting the master clock of mammalian cells[114], and candidate signaling molecules for synchronization have been identified[115, 116], but

the mechanism of synchronization is missing. The number of single-cell trajectories in such studies is typically 100 or less, precluding a test of a synchronization mechanism.

Single cell measurements have yet to be made on one of the most fully explored biological clocks in the model fungal system, *N. crassa*. Specifically, little is known about how the oscillators of *N. crassa* behave at the single cell level, whether the oscillators are stochastic in nature, and whether or not the oscillators of different cells communicate to overcome their stochastic asynchrony. The microfluidic droplet platform described in this thesis work is capable of measuring the biological clock of *N. crassa* at the single-cell level by isolating single-cells in individual droplets and keeping them very stable for long-term periods of observation (up to 10 days). This platform can measure the circadian rhythm of a large number (>1000) of single-cells, demonstrating a great potential to help our understanding of some of the fundamental aspects about the biological clock of *N. crassa*.

4.1 Measurements of expression on single cells over 10 days

A summary of the workflow of the microfluidic droplet system developed here is shown in Figure 4.1. In step 1 a flow-focusing microfluidic device is used to encapsulate cells in droplets. A stream of the *N. crassa* cell suspension meets two streams of fluorinated oil at the intersection as shown in the zoom-in figure entitled ‘Cell encapsulation’. As a result the stream of cell suspension is divided into dispersed droplets with various numbers of cells. Afterwards, the droplets are collected into a capillary tube in step 2. The two ends of the capillary tube are then sealed, and the capillary tube is put onto a motorized microscope stage. A CCD camera is used to record the fluorescence images of the encapsulated cells in step 3. A single layer of droplets is formed in the capillary

tube, and the droplets are very stable over ten days, which makes it possible to track the fluorescent intensity of individual cells over time. Figure 4.1B and C show the photos of the microfluidic device and the sealed capillary tube, respectively. The ability of the droplet

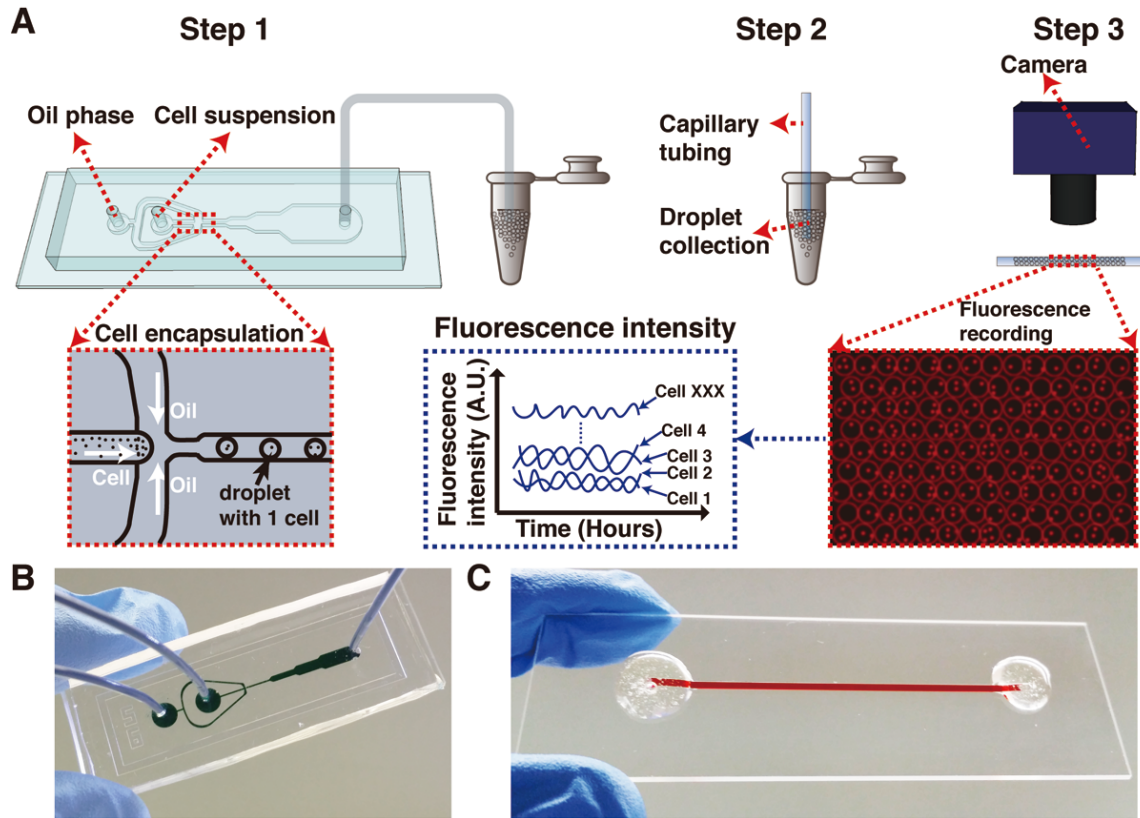


Figure 4.1: Oscillators of single cells can be measured with the workflow involving droplet microfluidics devices and fluorescent recorders of a clock output gene. (A) There are 3 steps for capturing cells in droplets so that fluorescence data can be measured on each cell. In Step 1 cells are encapsulated in droplets by a microfluidics device with flow-focusing geometry. In Step 2: droplets are collected from step 1 into capillary tubing. In Step 3: encapsulated cells are viewed by time-lapse fluorescence imaging, and single cell fluorescence data are extracted. (B) Photo of the microfluidics device for cell encapsulation. The channel is dyed green. (C) Photo of capillary tubing. The capillary tubing is dyed red.

microfluidics platform to measure expression of the *clock controlled gene* (*ccg-2*) on each of 868 single cells over 10 days is shown in Figure 4.2. A fluorescence recoder (mCherry) driven by *ccg-2* promoter in MFNC9[30] strain was used to visualize the expression of the

ccg-2. A total of 868 single cells fluorescence intensity time series can be tracked over 10 days. Droplet stability was dependent on the surfactant used to coat the droplets[94], and the stability of cell location was in part due to the microfluidics device as well as media derived previously[96]. A recently developed automated cell counting technique was used to verify that 80%+/- 2% of the cells were still viable at the end of the ten day experiment[117].

4.2 Stochastic oscillators in single-cells

Some sample fluorescence intensity trajectories of single cells are shown in Figure 4.2A. They all show a rhythm with a period ~ 21 hours. There is some variation in amplitude and phase among them. Single cells here are those for which only one cell (singletons) is isolated in a droplet. This excludes the complication of synchronization of multiple cells within droplets. All cells were transferred to the dark (for ten days) to allow circadian rhythms to develop, interrupted only briefly during imaging of cells (every 30 min). It is evident that there is substantial variation in the trajectories of *ccg-2* expression in different isolated cells in Figure 4.2B. A summary of the periods of all trajectories is captured in the periodogram of each cell in a heat map (Figure 4.2C). The principal period is 21 hours with limited variation about this mean as expected[30].

In each trajectory there are two components of variation in fluorescence intensity, stochastic variation in *ccg-2* gene expression and variation due to experimental detection noise; the stochastic variation can be further decomposed into intrinsic variation in *ccg-2* expression and extrinsic variation due to other cellular components[119]. Both sources of variation, stochastic and that due to experimental detection noise, can be quantified

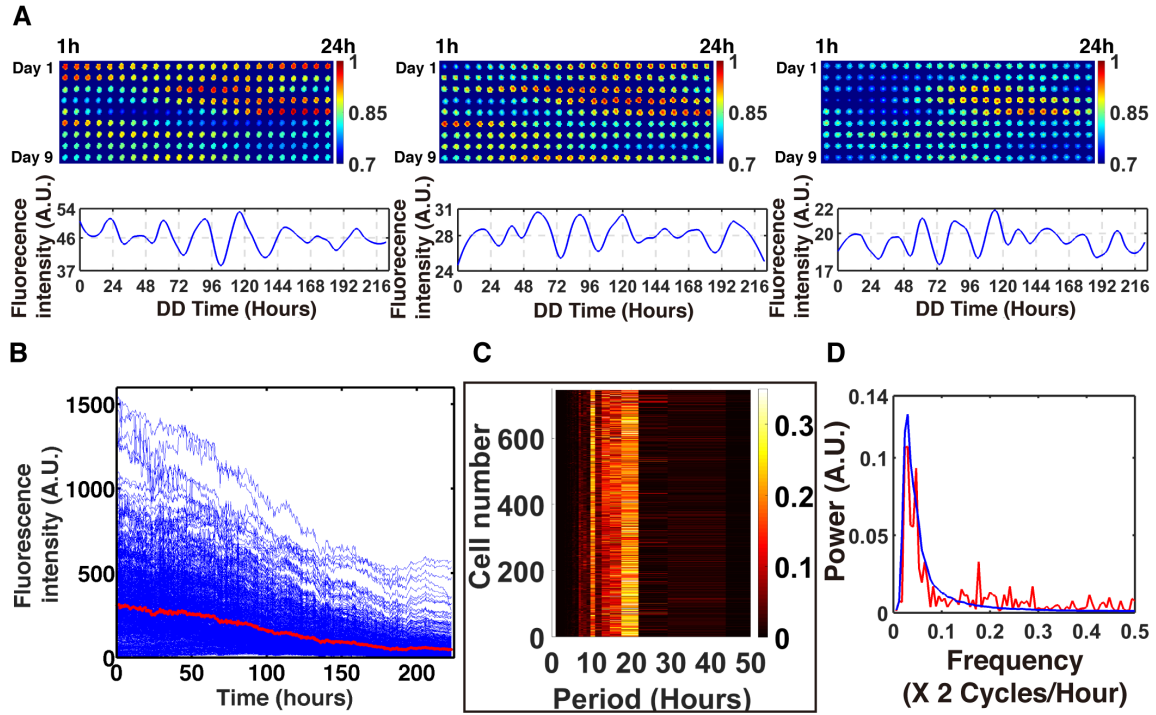


Figure 4.2: The oscillators in single cells of *N. crassa* are circadian with a period of 21 h in the dark (D/D), but there is substantial variation in phase and amplitude captured in a stochastic genetic network fitting the single cell clock data. The scales in A (bottom panel of temporal traces) do vary so that it is easier to examine the variation in periods of the three trajectories. Trajectories were normalized and detrended as described in chapter 3 experimental method. (A) Circadian oscillation of fluorescence data on *cgc-2* gene expression recorder is shown from individual *N. crassa* conidia with substantial variation in amplitude and phase. Scale bar, 20 μm . (B) Stochastic variation in 868 cells in one microscope view is shown with only a slight photobleaching effect for the mCherry recorder used. The curve in red is an average of all 868 trajectories (in blue). (C) A heat map of 868 cells is shown representing the periodogram of each of 868 cells on the Y-axis and the period, on the X-axis. Yellow is indicative of higher power at a particular period. The period varies about 20-21 h in the heat map. The sum of the periodogram values is used to normalize the power output of each period so that the power can be interpreted as the fraction of oscillators of a particular frequency. (D) The average periodogram of a stochastic clock network (in blue) derived from a working ensemble of deterministic models[118] fits the average periodogram of 868 cells (in red) derived from the individual periodograms in panel C.

with a control experiment in which cells are replaced with fluorescent beads of diameter, comparable to the mean size of macroconidial cells. The latter was measured with

automated cell counting of 636 cells to be $8 \mu\text{m}$. The stochastic trajectories do display a slight negative trend due to the photobleaching of the mCherry recorder gene. To control the photobleaching, the time between measurements was limited to 30 minutes. The result was 480,000 fluorescent measurements of *ccg-2* expression on the circadian oscillators of 1,000 cells.

It would be desirable to know the sources of variation in the rhythms of individual cells. First, a number of steps were taken to reduce the variation due to experimental error in trajectories. For example, the depth of the observation chamber in Figure 4.1 was $50 \mu\text{m}$ in size to prevent cells from drifting in or out of focus (chapter 3). Rhodamine B was introduced as an internal standard so that the measured fluorescence of cells was made relative to the Rhodamine B standard to reduce experimental error. The media was selected to inhibit cell division, and direct observation was used to confirm that no cell division occurred during the 10 day experiment. An image processing routine including a quality control filter was applied to ensure that particle (cell) tracking from frame to frame was carried out correctly. Using an automated cellometer (Nexcelom, Inc., Lawrence, MA), the mean cell size was estimated to be $\sim 8 \mu\text{m}$, and so a 10 day control experiment with $9.94 \mu\text{m}$ fluorescent beads replacing cells was conducted in the same way, allowing us to estimate separately the variation due to experimental error from the stochastic variation between genetically identical cells.

Westermarck et al.[29] recognized the importance of an error model for single cell measurements. A noise detection model was developed to get an understanding of how the stochastic variation from the cells' clock and experimental detection noise were propagated to the periodogram[104]. An error model was identified with six bead experiments. The

stochastic noise from the cell's clock and the experimental detection noise were then estimated separately. A sizeable >94% of the variation was stochastic variation (as opposed to experimental detection noise) in expression between cells.

Having separated the stochastic variation measured in cells over ten days (Figure 4.2B) from the experimental error measured in control bead experiments (using fluorescent 9.94 μm beads), we wished to know if the oscillators were circadian. A separate periodogram was calculated for each cell in Figure 4.2C, and the average periodogram has a peak at 21 hours in Figure 4.2D (red curve) as expected[30] from both race tubes and fluorometry at the macroscopic level. The oscillators of individual cells were circadian, but they are clearly not in phase from Figure 4.2B. As an example of this, the periodicity of the average trajectory (Figure 4.2B in red) is very weak, if visible at all, but the periodograms of individual cells display a strong peak in the periodogram near 21 hours in Figure 4.2C. As with the suprachiasmatic nuclei (SCN) of mammalian cells, *N. crassa* cells have cell-autonomous oscillators

As the detection noise is only less than 6%, an ensemble of stochastic models derived from an working deterministic model[120] was developed based on fitting the average of the experimental single-cell periodograms in Figure 4.2D (red curve). The modeled CCG-2 trajectories are generated by the Gillespie Algorithm[121]. The average of the periodograms of simulated single-cells trajectories (blue curve in Figure 4.2D) fits the experimental periodogram quiet well. The oscillators of single cells of *N. crassa* are demonstrated here to be stochastic circadian oscillators. The origin of the stochasticity maybe in part due to the transcriptional bursting of the core clock genes themselves[32]. The random activation of the core clock genes (white-collar-1 (*wc-1*) and frequency (*frq*))

are likely to be responsible for generating phase and amplitude variation in the single cell circadian oscillators.

Some have hypothesized that the period of each circadian single cell oscillator should be independent of its amplitude[51]. We hypothesize that the amplitude and period of each single cell should be positively correlated because they are simply related features of the periodogram of each single cell oscillator (Figure 4.2C). We also predict that there should be an inverse relation between phase (i.e., the number of cycles completed in a fixed time period by a single cell oscillator) and the period of the oscillator. Since phase and period are expected to have a negative relation and period is expected to have a positive relation to amplitude, we also predict that phase should have a negative relation to amplitude. Plots of the phase, amplitude, and period of each single cell oscillator support our hypotheses (Figure 4.3). Period and amplitude are significantly positively correlated as expected (Figure 4.3A), and amplitude and phase are significantly negatively correlated as expected (Figure 4.3C). The ability of the droplet platform to detect a correlation between period and amplitude (Figure 4.3A) is probably due to observing 3.4 times as many single cell oscillators as the earlier experiment[51]. The histogram of the phase of the 868 single cells is shown in Figure 4.3D (blue curve) which is in good agreement with the modeled trajectories (red curve). The only difference is that the mean (\pm two standard errors) of the oscillator phases observed (17 ± 0.16 cycles/85 hours) is slightly higher than that predicted by the stochastic model (13 ± 0.16 cycles/85 hours). A Kolmogorov-Smirnov 2-sample test[122] comparing the two phase distribution after subtracting means barely reaches significance ($P = 0.02$)

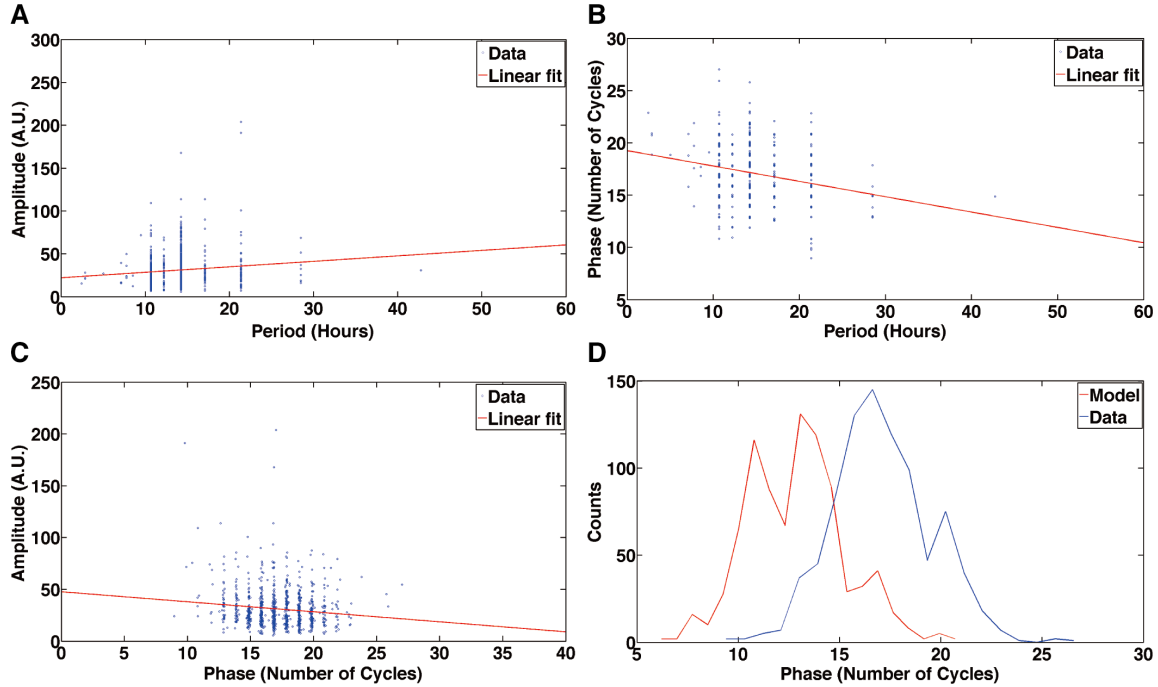


Figure 4.3: Relationship between period, amplitude, and phase of the circadian oscillator. (A) Plot of amplitude vs. period for 868 single cell oscillators in Figure 4.2B. The amplitude is the square root of the maximum power in the periodogram. The period is $1/2\pi f_l$, *i.e.*, the inverse of the frequency f_l at which the periodogram is maximum in power. The correlation (r) of amplitude and period is $r = 0.1095$ (Fishers $z = 0.1099$, $P < 0.001$)[123]. The Spearman rank correlation (r_s) is $r_s = 0.1101$ ($P < 0.01$)[122]. The straight line regression of amplitude on period (in red) is also shown. (B) Plot of phase vs. period for 868 single cell oscillators in Figure 4.2B. The discrete Hilbert phase $f^H(t)$ at time t is calculated from the Hilbert transform of each cell's trajectory after subtracting its mean over time[124]. The phase of an oscillator plotted here is defined as $M^C = [f^C(t_1) - f^C(t_0)]/2\pi$ in units of cycles, where $f^C(t)$ is the continuous Hilbert phase at time t . The phase can be thought of as the number of cycles, which a single cell oscillator completes in the time interval $t_1 - t_0 = 230 - 60$ in units of half hours. The continuous Hilbert Phase $f^C(t)$ is defined recursively by $f^C(t + 1) = f^C(t) + m^C(t)2\pi$ where $m^C(t)$ is the argument m that minimizes $Df_m = |f^H(t + 1) - f^C(t) + 2\pi m|$. The correlation (r) of phase and period is $r = -0.1986$ (Fishers $z = -0.2013$, $P < 0.001$)[123]. The Spearman rank correlation (r_s) is $r_s = -0.1376$ ($P < 0.001$)[122]. The straight line regression of phase on period (in red) is also shown. (C) Plot of amplitude vs. phase for 868 single cell oscillators in Figure 4.2B. The correlation (r) of amplitude and phase is $r = -0.1226$ (Fisher's $z = -0.1232$, $P < 0.001$). The Spearman rank correlation (r_s) is $r_s = -0.0880$ ($P < 0.02$)[122]. The straight line regression of amplitude on phase is shown (in red). (D) Histogram of the phase of 868 single cell oscillators in Figure 4.2B and 868 Gillespie simulated trajectories of the stochastic model. The phase is functionally independent of the periodogram. Trajectories in both model and data are detrended.

4.3 Single-cells circadian oscillators in *Neurospora Crassa* can be entrained by light

In the last section, we have shown that *N. crassa* single-cells have an circadian oscillator by measuring the clock control gene (*ccg-2*) expression over 1000 single-cells up to 10 days with the develop microfluidics droplet platform. While these oscillators in single-cells of *N. crassa* have been demonstrated to generate circadian rhythms in Figure 4.2, these oscillators have not be shown to be light entrained. Circadian rhythm, light entrainment, and temperature compensation are the three major properties that define a biological clock[20]. In fact, the presence of a clock in a single cell has not been demonstrated.

The presence of such a clock in *N. crassa* would help to establish how synchronized circadian behavior originates at the macroscopic level of 10^7 cells in eukaryotic systems, where most measurements on the clock are performed[125]. Because of the substantial stochastic intracellular variation within single cells, it is not clear how ensembles of cells overcome stochastic intracellular variation in circadian rhythms to display highly synchronized behavior at the macroscopic level. There could be a variety of mechanisms. For example, single cells with a functioning clock could function as “pacemakers” to synchronize the behavior of surrounding cells in fungi, animals, and plants and provide an explanation for how circadian rhythms are coordinated at the multiellular level[126]. Alternatively there could be no leaders but chemical signals that synchronize the oscillators[127]. There also may be a positive role for stochastic intracellular noise in synchronizing single cell oscillators[128, 46]. The light conditions are considered to be very useful experimental setting for observing the biological system’s endogenous dynamics[129].

Synchronization of organisms with their environment is aided by their biological clock[130]. The biological clock of higher organisms can be entrained very efficiently to the 24-light dark cycle[131]. Light entrainment is a primary capability a biological clock has to help synchronize the organism to the surrounding environment. With light entrainment, the rhythms that generated/controlled by the biological clock are in phase with the light signal and have the same period as the light signal, which the biological clock receives. It would be very interesting to learn whether on the single cell level, the circadian oscillator possesses light entrainment properties, or is it the emerging phenomena from coupled cells like those in the macroscopic level[120]. Only single cell measurement on the biological clock under light entrainment conditions could help answer this question and may provide some insights about whether the coupling would affect the light entrainment of the biological clock.

While light entrainment studies have been done on the uncoupled mammalian suprachiasmatic nuclei (SCN) cells[132], light entrainment of the biological clock of single *N. crassa* cell has never been demonstrated. Under cell-to-cell coupling condition, imaging of single cells of Zebrafish tissues[133] and plants[44] have shown that cells shift their phases to a common phase while responding to the light signal.

Using the microfluidic droplet platform developed in this thesis, we measured the oscillators of > 1000 single *N. crassa* cells under different light entrainment conditions and begin to test some of the hypotheses about the origin of the biological clock. For example, one hypothesis is that clock is a property of single cells. Each cell has its own clock. Alternative hypotheses are that clock-like properties, such as circadian rhythms,

light entrainment, and temperature compensation are orchestrated by a few pacemaker cells or are emergent properties of cell-to-cell synchronization.

We investigated whether the single cells of *N. crassa* can be entrained by light by exposing them under three different light entrainment conditions and measuring the fluorescence intensities of single cells at the same time. A LED light was used to control the light/dark (LD) cycles the cells experienced during measurement as show in Figure 4.4. At the macroscopic level, millions of *N. crassa* cells can be entrained to light-dark cycles of different period length[120, 134]. Here we used a quasi-square-wave light intensity profile with different light/dark (LD) cycles, 3 hours light on/ 3 hours light off, 6 hours light on/ 6 hours light off, 18 hours light on/ 18 hours light off. The light intensity is 5300 lux and has a spectrum of sunlight (6500K)

It has been demonstrated elsewhere in the literature that *N. crassa* can form conidiation bands under very short day cycles[120, 135]. The auto-feedback loops for WCC activating *wc-1* and *wc-2* were predicted and confirmed to be a mechanism that enables *N. crassa* to entrain to an artificial day as short as 6 hours[120]. The effect of bluelight photoreceptor VVD induced by light-activated WCC inhibiting the function of the WCC itself is believed to in part be responsible for entrainability of the clock *N. crassa* to LD cycles with short photoperiod[129, 136]. With the possibility to measure the response of single cells of *N. crassa* to different LD cycles we are able to look at whether single cells of *N. crassa* has the same entrainability as cells forming banding in racetubes when there are large amounts of them[120]. A total of 1330 single cell *N. crassa* fluorescence intensity time series are shown in Figure 4.5A (blue curves). They are obtained by measuring the fluorescence intensities of single cells that are exposed to a 3 hours light on and 3 hours light

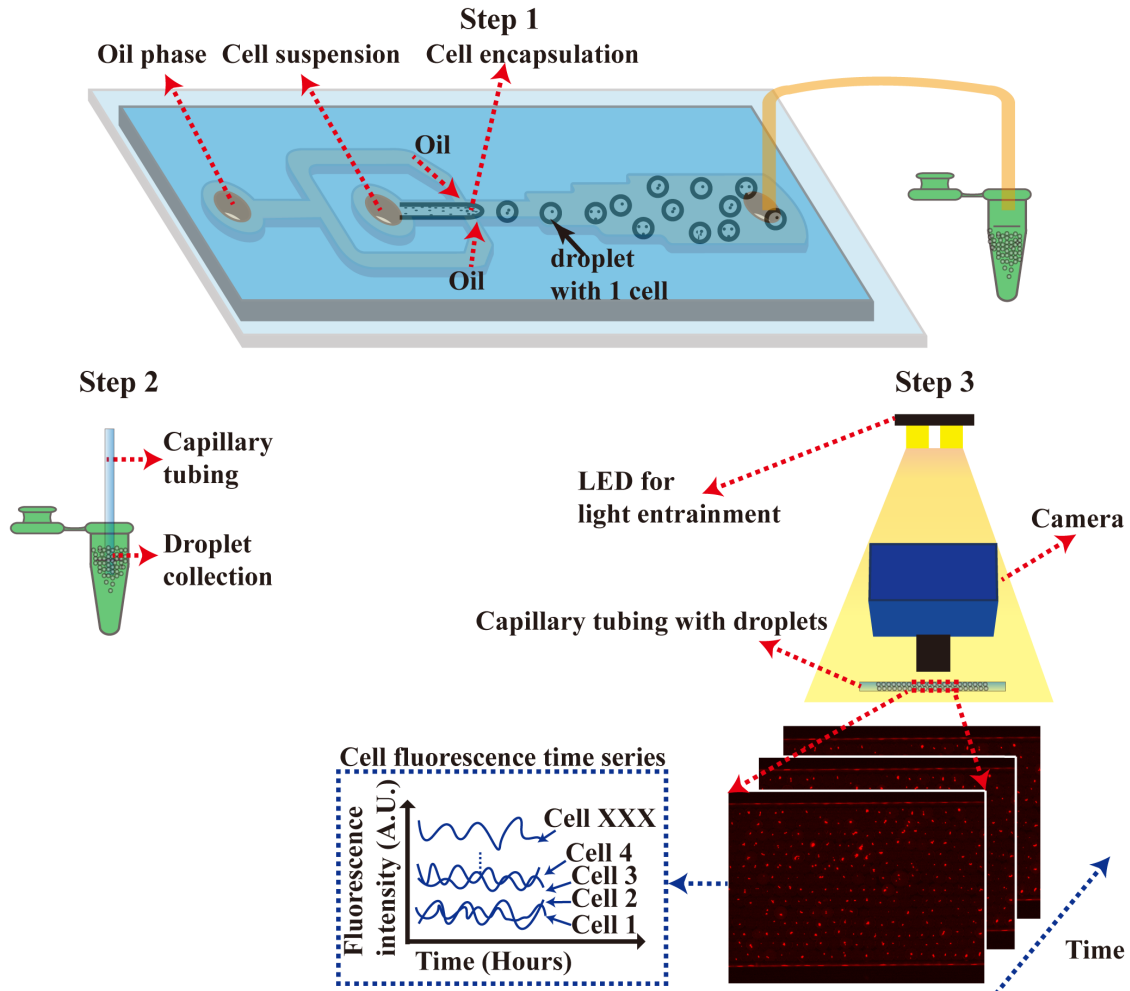


Figure 4.4: The microfluidic droplet platform integrated with a LED light to control the light-dark cycles that the cells experienced. Step 1: A droplet generation device for cell encapsulation. Step 2: Droplets are collected into capillary tubing. Step 3: Time-lapse fluorescence imaging by a CCD camera through a microscope under light entrainment and fluorescence data extraction.

dark cycles. The average of all the single cell fluorescence intensity time series is the red curve in Figure 4.5 which shows oscillations along the LD cycles. The yellow background indicates when the light was on and the grey background indicates when the light was off. Figure 4.5B shows 10 sample fluorescence intensity trajectories (color curves) from Figure 4.5A after normalization by Rhodamin B intensity and detrended by a 24-hours moving average[105]. The thicker black curve in Figure 4.5 is the average of the 10

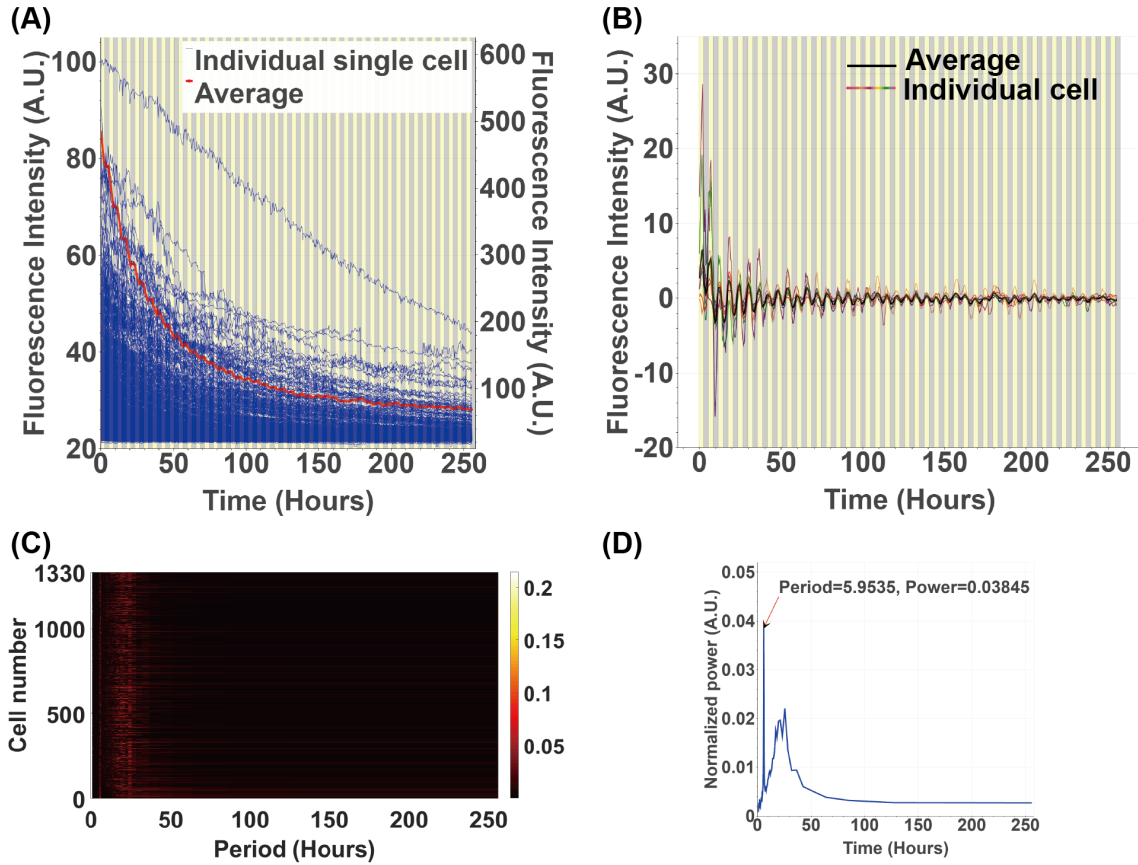


Figure 4.5: Entrainability of Single cell *N. crassa* to a 6 hours artificial day with 3 hours light on and 3 hours light off. (A) 1330 single cell fluorescent intensities (blue curves, right y axis) and the average of all the single cell fluorescent intensities (red curve, left y axis). Yellow background indicates light on, and grey background indicates light off. (B) Sample of 10 single-cell fluorescence intensity time series from (A) after normalization and detrend (color curves) and their average (black curve). (C) A heat map showing the periodogram of each of the 1330 single cells fluorescence trajectories from (A). On the Y-axis is the cell number of the 1330 single cells and on the X-axis is the period. Yellow is indicative of higher power at a particular period. (D) Average of the periodograms of all the single cells fluorescent time series in (A). The periodogram is normalized so that for each periodogram, the sum of periodogram values is used to normalize the power output of each period so that the power can be interpreted as the fraction of oscillators of a particular frequency.

sample trajectories. There is still some heterogeneity among these 1330 single cells in their amplitudes and phase even when they were subjected to the same LD cycles. It is obvious that the light entrainment of single cells is able to limit occurrences of stochastic noise induced phase drifting of individual cells. As a result, the average output of the clock oscillates regularly along the 3 hours light on and 3 hours light dark cycles. We calculated the periodograms of all the 1330 single cell fluorescence intensity time series and summarized it in Figure 4.5C. Each periodogram of a single cells is a row in the heat map of Figure 4.5C. A very narrow band around the period value of 6 hours is shown in Figure 4.5C, indicating that most of the isolated cells has a period of 6 hours corresponding to the period of the LD cycles used to entrain them. The average of all the single cells' periodogram is also shown here in Figure 4.5D. The highest averaged periodogram power comes from the period ~ 6 hours. These results demonstrate that single *N. crassa* circadian oscillator can be entrained to the 3 hours light on and 3 hours light off cycles.

Single cells were also exposed to a 6 hours light on and 6 hours light dark cycles. Fluorescence intensity time series of 1626 single cells are shown in Figure 4.6A blue curves. The average of all the single cells fluorescence intensity traces is the red curve in Figure 4.6 which shows oscillations consistent with the alternation of light on and light off. Again 10 sample fluorescence intensity trajectories after normalization and detrending are presented in Figure 4.6B color curves with their average shown as the black curve. There is also phase and amplitude variation among individual cells. A periodogram heat map, Figure 4.6C, shows a bright band around 12 hours, demonstrating that most of the single-cells are entrained to a 12 hour period. A peak at ~ 12 hours is also shown in the

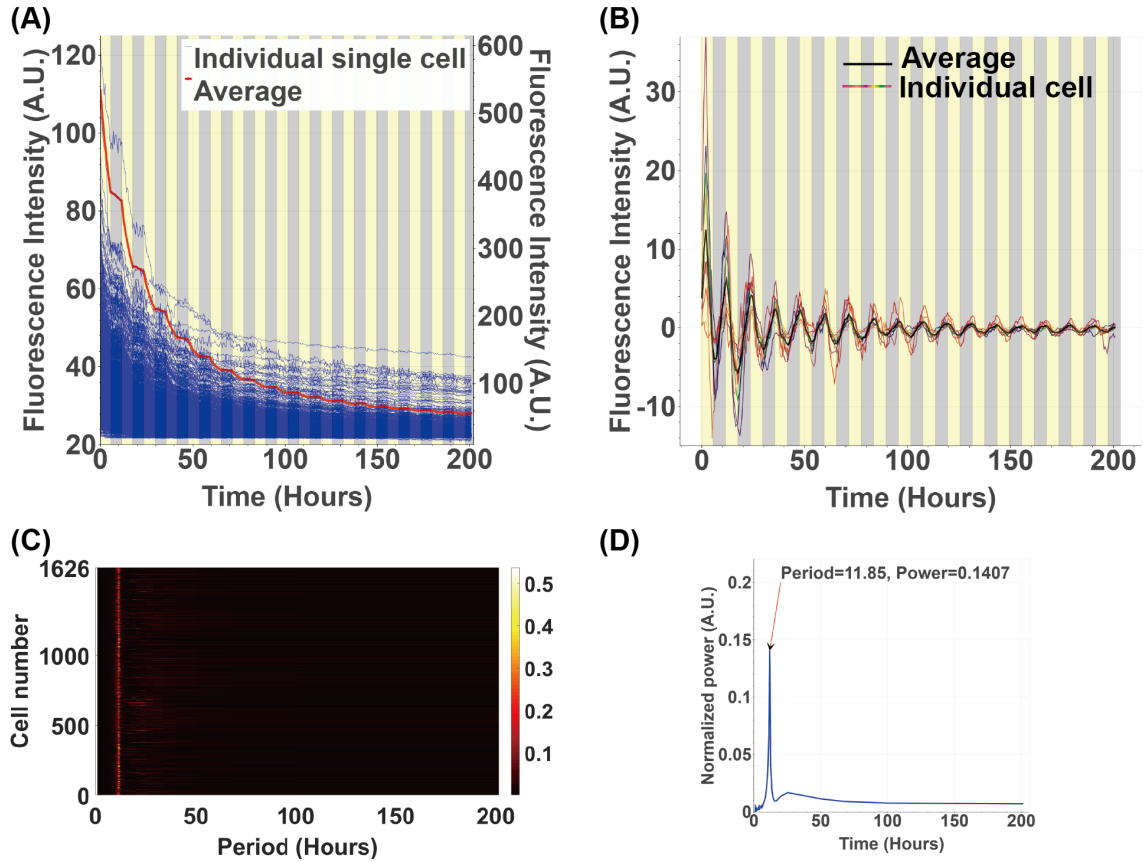


Figure 4.6: Entrainability of Single cell *N. crassa* to a 12 hours artificial day with 6 hours light on and 6 hours light off. (A) 1626 single cell fluorescent intensities (blue curves, right y axis) and the average of all the single cell fluorescent intensities (red curve, left y axis). Yellow background indicates light on, and grey background indicates light off. (B) Sample of 10 single-cell fluorescence intensity time series from (A) after normalization and detrended (color curves) and their average (black curve). (C) A heat map showing the periodogram of each of the 1626 single cells fluorescence trajectories from (A). On the Y-axis is the cell number of the 1626 single cells and on the X-axis is the period. Yellow is indicative of higher power at a particular period. (D) Average of the periodograms of all the single cells fluorescent time series in (A). The periodogram is normalized so that for each periodogram, the sum of periodogram values is used to normalize the power output of each period so that the power can be interpreted as the fraction of oscillators of a particular frequency.

average periodogram of all the single cells, Figure 4.6D. Thus, single *N. crassa* cells can be entrained to the 12 hour artificial day with 6 hours light on and 6 hours light off.

We also examined the entrainability of single cells of *N. crassa* to a long LD cycles with period much larger than its intrinsic period[104]. Therefore the cells were subjected to a 18 hours light on and 18 hours light off. Again 1969 single cell fluorescence intensity traces are plotted as blue curves in Figure 4.7A. The red curve in Figure 4.7B is the mean of the blue curves. The normalized and detrended trajectories of 10 sample cells in Figure 4.7B shows more fluctuation as compared to the trajectories in Figure 4.5B and Figure 4.6B. These may due to the single cells being in longer constant conditions (18 hours) , and the intrinsic stochastic noise of single cells may introduce more amplitude variation and phase shifting during long constant conditions. The average of the 10 sample traces is also noisier in Figure 4.7B. Shown in the periodogram heat map Figure 4.7C, most of the cells have a fundamental period around 36 hours corresponding to the entrainment period. The average periodogram of all the single cells in Figure 4.7D has a peak at 36.57 hours with a broader spectrum as compared to that in Figure 4.5D and Figure 4.6D. These results indicate that single *N. crassa* cell can be entrained to the 36 hours artificial day with 18 hours light on and 18 hours light off.

We also looked at the amplitude, phase and period relationships of the single cell oscillators in the 3 light entrainment experiments. For single cell in DD condition, we saw that amplitude and period is positively correlated. We argue that the amplitude and the period of single cells is still correlated under light entrainment conditions. For the 6 hour artificial day data, however, the amplitude and period show a slight negative correlation (Figure 4.8A), which is different than that under DD condition. This may due to the LD

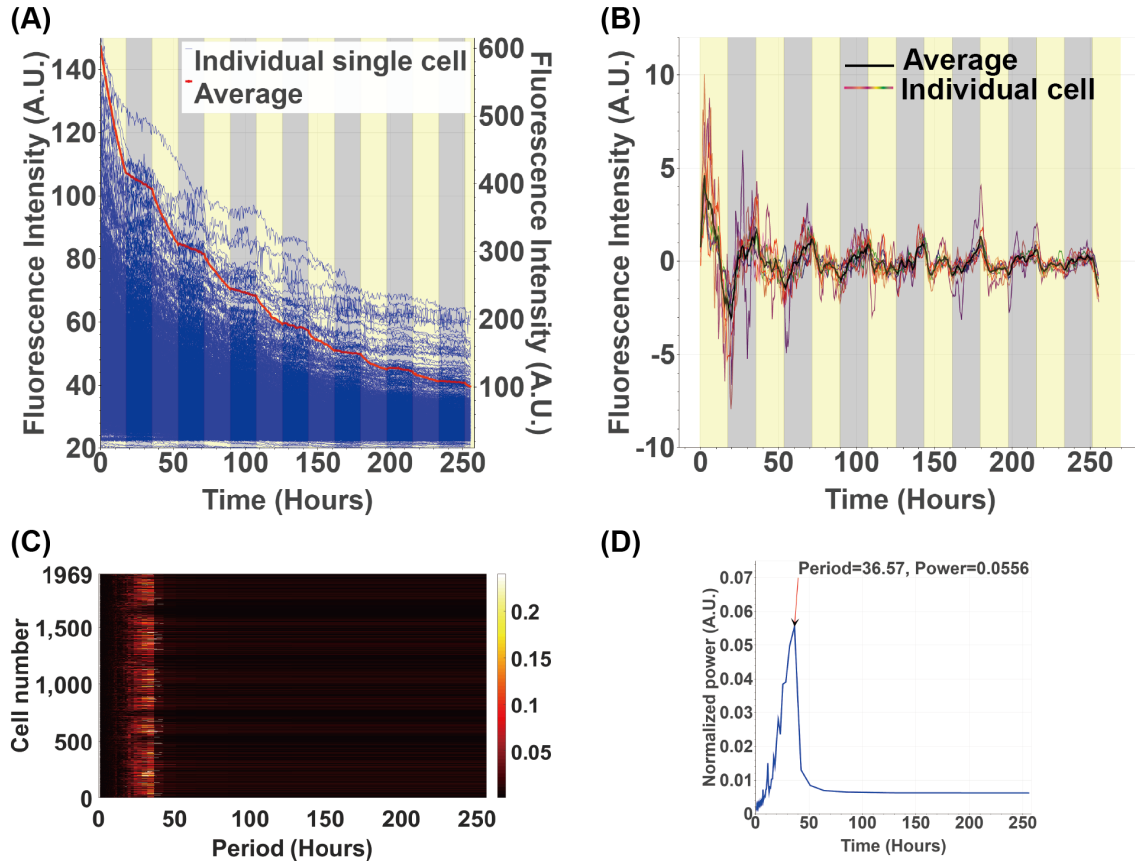


Figure 4.7: Entrainability of Single cell *N. crassa* to a 36 hours artificial day with 18 hours light on and 18 hours light off. (A) 1969 single cell fluorescent intensities (blue curves, right y axis) and the average of all the single cell fluorescent intensities (red curve, left y axis). Yellow background indicates light on, and grey background indicates light off. (B) Sample of 10 single-cell fluorescence intensity time series from (A) after normalization and detrended (color curves) and their average (black curve). (C) A heat map showing the periodogram of each of the 1969 single cells fluorescence trajectories from (A). On the Y-axis is the cell number of the 1969 single cells and on the X-axis is the period. Yellow is indicative of higher power at a particular period. (D) Average of the periodograms of all the single cells fluorescent time series in (A). The periodogram is normalized so that for each periodogram, the sum of periodogram values is used to normalize the power output of each period so that the power can be interpreted as the fraction of oscillators of a particular frequency.

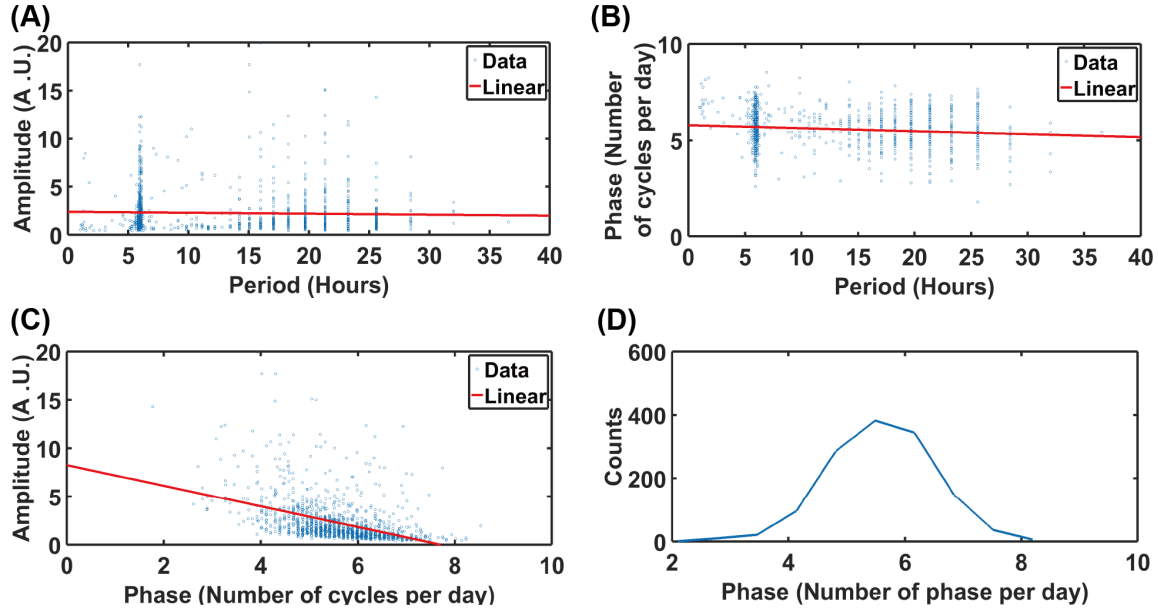


Figure 4.8: Period, amplitude and phase of the entrained oscillators under 3 hours light on and 3 hours light off. (A) Amplitude vs. period of 1330 single cell oscillators in Figure 4.5. The amplitude is half of the square root of the maximum power in the periodogram. The correlation (r) of amplitude and period is $r = -0.035$ (Fishers $z = -0.035$, $P = 0.2016$)[123]. The Spearman rank correlation (r_s) is $r_s = -0.057$ ($P = 0.0378$)[122]. The straight line regression of amplitude on period is shown in red. (B) Plot of phase vs. period of 1330 single cell oscillators in Figure 4.5. The phase is defined as described in Figure 4.3 but also normalized by dividing the number of days of the measurement. The correlation (r) of phase and period is $r = -0.1373$ (Fishers $z = -0.1382$, $P < 0.001$)[123]. The Spearman rank correlation (r_s) is $r_s = -0.1221$ ($P < 0.001$)[122]. The straight line regression of phase on period is shown in red. (C) Plot of amplitude vs. phase for 1330 single cell oscillators in Figure 4.5. The correlation (r) of amplitude and phase is $r = -0.4310$ (Fishers $z = -0.4612$, $P < 0.001$)[123]. The Spearman rank correlation (r_s) is $r_s = -0.5644$ ($P < 0.001$)[122]. The straight line regression of phase on period is shown in red. (D) Phase histogram of 1330 single cell oscillators in Figure 4.5. The mean phase (\pm two standard errors) of the entrained oscillators is $5.5868 (\pm 0.0485)$ cycles per day

cycles period (6 hours) are much shorter than the intrinsic oscillation period (~ 21 hours), or not enough data. The amplitude has a positive correlation with the period for the 12 hours artificial day and 36 hours artificial day (Figure 4.9A and Figure 4.8A). Single cells oscillators that are entrained to the corresponding LD cycle period here show large amount of variation in their amplitudes. The mean amplitudes (+/- two standard errors) of the single cell oscillators with period at ~ 6 hours, 12 hour and 36 hours are 2.5190 (+/- 0.2040), 4.2929 (+/- 0.1515), and 3.8674 (+/- 0.1936). The phase has a negative correlation with the period (Figure 4.8B, Figure 4.9B and Figure 4.10B) as expected since slower oscillators with longer period complete less number of cycles in a fix period of time. The amplitude is also negatively related to the phase (Figure 4.8C, Figure 4.9C and Figure 4.10C). Histograms of phase distributions are shown in Figure 4.8D, Figure 4.9D and Figure 4.10D with mean phase (+/- two standard errors) of 5.5868 (+/-0.0485), 4.5816 (+/- 0.0626) and 5.1177 (+/- 0.0656).

4.4 Temperature compensation is observed in single cells of *Neurospora crassa*

In addition to light entrainment, a biological clock also has a characteristic called temperature compensation[20]. Temperature compensation means the clock period does not change over the physiological temperature range (15 °C to 34 °C)[137]. Many mechanisms for temperature compensation have been proposed based on the logic that stable period across large range of temperature change is achieved by balancing positive and negative contributions in the circadian oscillator[138–140]. Another adaptive mechanism was proposed that the ratio of two FRQ forms are regulated by temperature and thus the required threshold of FRQ for robust circadian rhythmicity can be maintain across

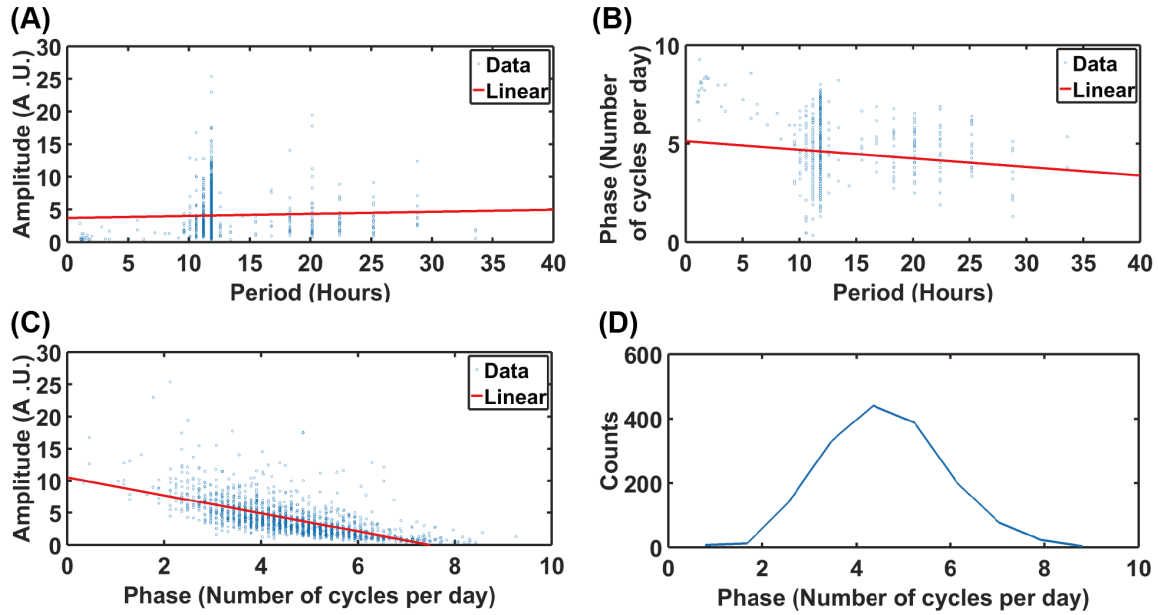


Figure 4.9: Period, amplitude and phase of the entrained oscillators under 6 hours light on and 6 hours light off. (A) Amplitude vs. period of 1626 single cell oscillators in Figure 4.6. The amplitude is half of the square root of the maximum power in the periodogram. The correlation (r) of amplitude and period is $r = 0.0358$ (Fishers $z = 0.0359$, $P = 0.1485$)[123]. The Spearman rank correlation (r_s) is $r_s = 0.0935$ ($P = 0.0002$)[122]. The straight line regression of amplitude on period is shown in red. (B) Plot of phase vs. period of 1626 single cell oscillators in Figure 4.6. The phase is defined as described in Figure 4.3 but also normalized by dividing the number of days of the measurement. The correlation (r) of phase and period is $r = -0.1079$ (Fishers $z = -0.1083$, $P < 0.001$)[123]. The Spearman rank correlation (r_s) is $r_s = -0.0406$ ($P < 0.001$)[122]. The straight line regression of phase on period is shown in red. (C) Plot of amplitude vs. phase for 1626 single cell oscillators in Figure 4.6. The correlation (r) of amplitude and phase is $r = -0.6543$ (Fishers $z = -0.7829$, $P < 0.001$)[123]. The Spearman rank correlation (r_s) is $r_s = 0.7409$ ($P < 0.001$)[122]. The straight line regression of phase on period is shown in red. (D) Phase histogram of 1626 single cell oscillators in Figure 4.6. The mean phase (\pm two standard errors) of the entrained oscillators is $4.5816 (\pm 0.0626)$ cycles per day

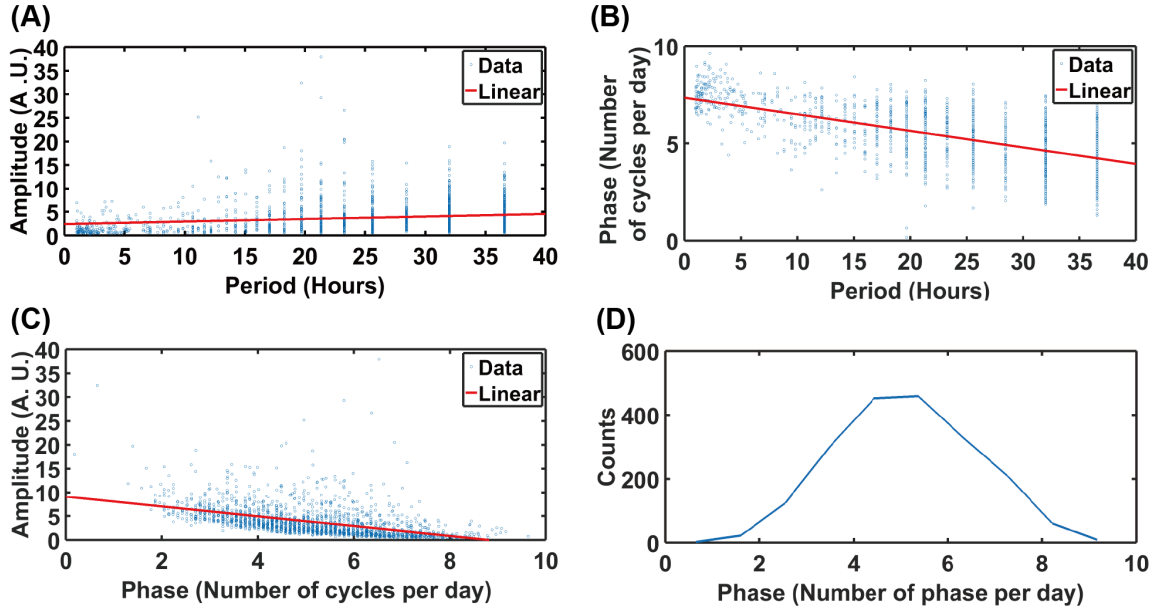


Figure 4.10: Period, amplitude and phase of the entrained oscillators under 18 hours light on and 18 hours light off. (A) Amplitude vs. period of 1969 single cell oscillators in Figure 4.7. The amplitude is half of the square root of the maximum power in the periodogram. The correlation (r) of amplitude and period is $r = 0.1852$ (Fishers $z = 0.1873$, $P < 0.001$)[123]. The Spearman rank correlation (r_s) is $r_s = 0.2843$ ($P < 0.001$)[122]. The straight line regression of amplitude on period is shown in red. (B) Plot of phase vs. period of 1969 single cell oscillators in Figure 4.7. The phase is defined as described in Figure 4.3 but also normalized by dividing the number of days of the measurement. The correlation (r) of phase and period is $r = -0.6248$ (Fishers $z = -0.7328$, $P < 0.001$)[123]. The Spearman rank correlation (r_s) is $r_s = -0.5600$ ($P < 0.001$)[122]. The straight line regression of phase on period is shown in red. (C) Plot of amplitude vs. phase for 1969 single cell oscillators in Figure 4.7. The correlation (r) of amplitude and phase is $r = -0.4752$ (Fishers $z = -0.5168$, $P < 0.001$)[123]. The Spearman rank correlation (r_s) is $r_s = -0.6510$ ($P < 0.001$)[122]. The straight line regression of phase on period is shown in red. (D) Phase histogram of 1969 single cell oscillators in Figure 4.7. The mean phase (\pm two standard errors) of the entrained oscillators is 5.1177 (± 0.0656)

a wide range of temperature[137]. Therefore it is likely that temperature compensation will present at the single cell level. In this section, we are going to investigate whether the circadian oscillator in *N. crassa* at the single cell level has the temperature compensation property.

If temperature compensation presents at the single cell level, the period length of the single cell will not change over a broad temperature range. In order to evaluate the period of single cells under different temperatures, a thermal stage was used to control/maintain the temperatures during each measurement. The temperature stability was verified in order to ensure the cells were kept at a constant temperature during each experiment as shown in chapter 3 section section 3.10. The single-cell fluorescence intensities were measured with the developed microfluidic platform under 5 different temperatures, *e.g.* 20 °C, 22 °C, 25 °C, 27 °C, and 30 °C.

Figure 4.11 shows the results for five temperature compensation experiments. In Figure 4.11, A, C, E, G, and I show the individual fluorescence intensity of single cells (blue curves) measured under the five different temperatures and the average of single cell fluorescence intensities are shown in red curves. Averages of the periodograms of single cells were calculated in Figure 4.11 B, D, F, H, and J for the single cells measured in Figure 4.11, A, C, E, G, and I. The peak at the average periodogram in Figure 4.11 B, D, F, H, and J indicates the period of the single cell circadian oscillators under the corresponding temperature. The period for each temperature compensation experiment is used to calculate the temperature coefficient Q_{10} (Table 4.1). The temperature coefficient Q_{10} is a measurement of the rate of change of period of the biological clock for every 10 °C increase in the temperature. In Table 4.1, all the Q_{10} values are close to or equal to 1,

indicating that the period of the circadian rhythm of single cell *N. crassa* are stable and efficiently temperature compensated.

Table 4.1: Temperature coefficient Q_{10} for single cell circadian oscillators. The temperature coefficient Q_{10} here is calculated using 30 °C as the reference temperature. $Q_{10} = \frac{P_1}{P_2} \frac{10}{T_1 - T_2}$. Q_{10} measures the rate of change of period of the biological clock for every 10 increase in the temperature.

T_1	20 °C	22 °C	25 °C	27 °C
Period (Hours)	22.6	20.55	21.17	20.55
Q_{10}	0.91	1.00	0.94	1.00

4.5 Conclusion

Most measurements on the biological clock are made macroscopically on $> 10^7$ cells. We illustrate a universal system of measurement on single cells. Oscillators in one cell can be measured by the developed microfluidics droplet platform. Single cells of *N. crassa* are shown to have cell-autonomous circadian oscillators in a fungal system with a biological clock well understood macroscopically. With the microfluidic droplet platform developed here, the light entrainment property is for first time demonstrated to present in the single cells *N. crassa* by measuring >1000 single cells under 3 different light entrainment conditions. The single cells of *N. crassa* can be entrained to a short artificial day with a 6 hours period as well as to a long artificial day with a 36 hours period. Single-cells of *N. crassa* was shown to have temperature compensation properties. Therefore, we demonstrated that single-cells of *N. crassa* have a biological clock.

What is missing from single cell measurements on biological processes, such as circadian rhythms, is a universal system of measurement. Such a system should be able

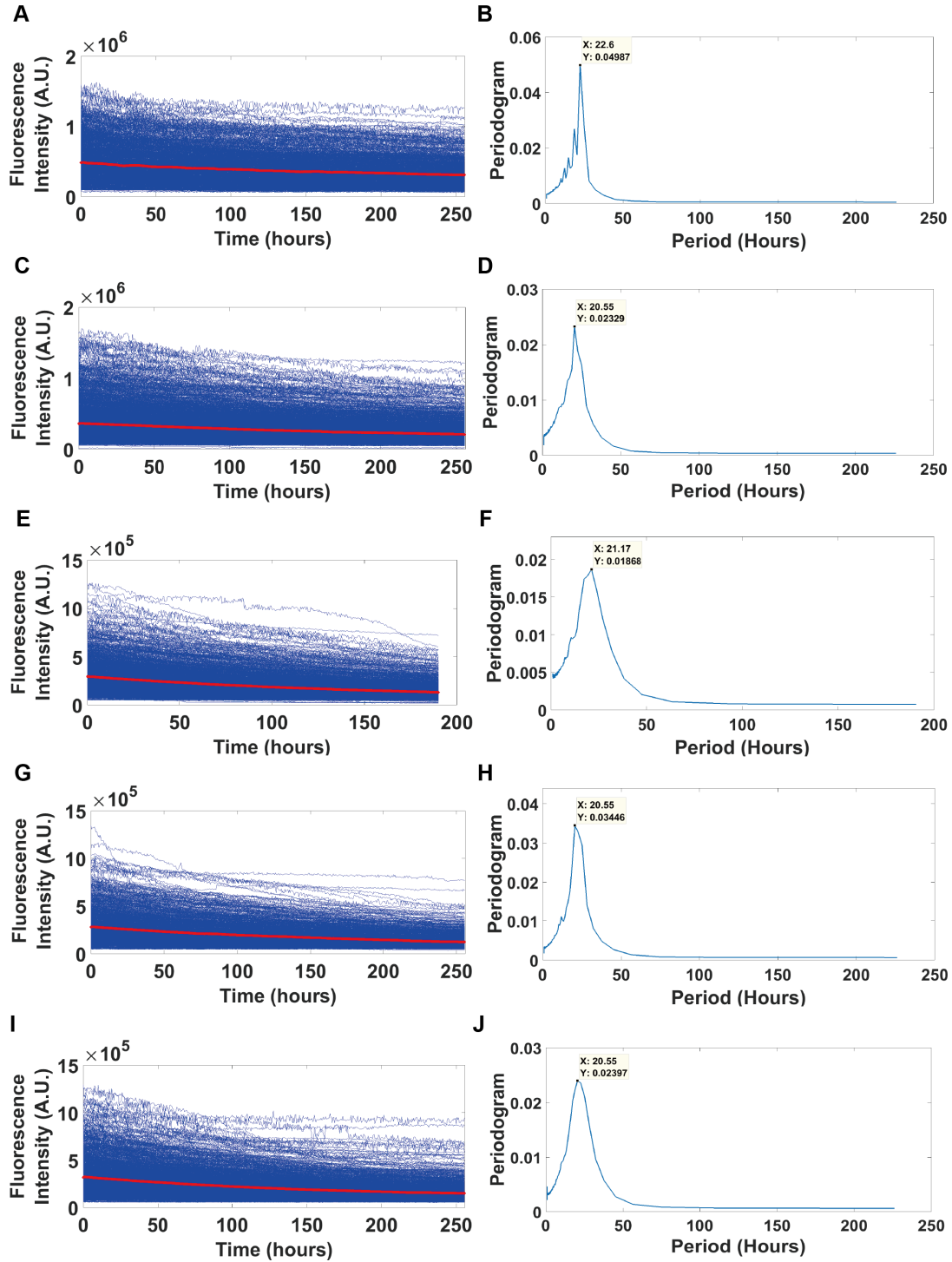


Figure 4.11: Single cell temperature compensation.(A), (C), (E), (G), and (I) are fluorescence intensity of single cells (blue curves) and the their average (red curve) under 20 °C, 22 °C, 25 °C, 27 °C, and 30 °C. (B), (D), (F), (H), and (J) are the average periodograms of single cells fluorescence intensities in (A),(C), (E), (G), and (I). The periodogram values are normalized by the sum of powers at all the frequencies or periods.

to identify both cellular stochastic variation and detection noise (i.e., experimental error). The detection model needs to be a well-grounded physical model to generate detection noise. Second, the cellular measurements should ideally be normalized against an internal control to capture uncontrolled factors. Such a system should also be able to propagate the sources of error (stochastic intracellular noise and detection noise) to the statistics used to test biological hypotheses of interest. Finally, the sources of error should have quantifiable effects on these statistics. With the single cell measurements made here by the microfluidics droplet platform, such a universal system of measurement can be achieved with a noise detection model[104]. Doped bead experiments were conducted on the microfluidics droplet platform instead of cells to capture the fluorescent detection noise. The two sources of error, intercellular stochastic noise and experimental noise, are each propagated through the analysis pipeline to the end statistics used to quantify the biological features, e.g. periodogram, amplitude, phase of the biological clock.

Single *N.crassa* cells were shown to have an stochastic circadian oscillator, and the mechanism for how the stochasticity is generated is hypothesized to be that involving transcriptional bursting of *frq* and *cgc-2* by WCC. At least 94% of the periodogram variation in oscillators from cell to cell is stochastic, a new result for the fungal circadian field.

CHAPTER 5

SYNCHRONIZATION OF THE BIOLOGICAL CLOCK *NEUROSPORA CRASSA*

5.1 Synchronization measures of the circadian stochastic oscillators.

In the face of substantial variation in the circadian stochastic oscillators within single cells (Figure 4.3), the question remains: how do they synchronize to produce the regular biological clock observed at the macroscopic level by race tubes or fluorescent or luciferase recorders? At some point the ensemble of oscillators overcomes stochastic asynchrony. We would like to look at whether there is synchrony among cells encapsulated within the same droplet, where they have a chance to communicate with each other. In order to demonstrate this synchronization we needed to be able to measure their collective behavior[141]. For example, Garcia-Ojalvo et al.[142] have suggested one way of measuring synchronization, namely in our context, the variance in the mean fluorescence of cells within a droplet divided by variance in fluorescence of a single cell (*i.e.*, the variance of the red curve over time divided by the variance in individual trajectories in blue in Figure 4.2B over time). They analyzed this measure in the context of a system of coupled repressilators related to our own working clock network[118]. What was missing from this measure is accounting for the between droplet variability in our experiment.

For other systems an array of synchronization measures have been utilized, such as the maximum of the cross-correlation between cells (with respect to frequency), mutual information, phase synchronization extracted by either Hilbert or Wavelet transform, or an index based on a circular variance[141, 124]. A careful study of the utility of such measures

has led some authors to conclude there is no universally best measure of synchronization, but the measure needs to be tailored to the problem at hand[124]. The focus of most of these measures is on phase synchronization.

A good synchronization measure should not only capture similarity in the phase of circadian oscillators, but also the similarity in their amplitude and period. Second, the measure should measure the synchrony or similarity of cell trajectories within a droplet relative to the variability between droplets. Third, the measure should be easily interpretable, as is the measure suggested previously[142]. Fourth, the measure should have well defined statistical properties to allow inference about the systems of coupled oscillators.

One such measure with all of these properties is the intraclass correlation[143, 144]. Consider one time point in the microfluidics droplet experiment. Let X_{ij} be the fluorescence of the j th cell in the i th droplet at one time point when there are a cells per droplet. We assume that the measurements X_{ij} have the following covariance structure[143]:

$$\begin{aligned}
 COV(X_{ij}, X_{kj}) &= 0, i \neq k \text{ (different droplet)} \\
 &= \rho\sigma^2, i = k, j \neq l \text{ (different cells within a droplet)} \\
 &= \sigma^2, i = k, j = l \text{ (same cell within a droplet)}
 \end{aligned} \tag{5.1}$$

The covariance (COV) is defined over all cells j in droplet i of size a at a particular time point.

In this variance components model[143] the intraclass correlation is ρ , the correlation between different measurements within a droplet. This measure has been used

for over 150 years[143], particularly in twin studies as a measure of heritability[145]. The variance σ^2 in one cell within one droplet at one time can be estimated by observing cells in replicate droplets. The partitioning of fluorescence variation is summarized in an analysis of variance (ANOVA) in Table 5.1[143]. The total variation in fluorescence SS_T was partitioned into a between droplet sum of squares (SS_B) and a within droplet sum of squares (SS_W) in Equation 5.2 such that $SS_T = SS_B + SS_W$. By setting the estimated mean squares (EMS_B and EMS_W) equal to their expectations in Table 5.1, we obtain two equations in two unknowns (σ^2 and ρ) in Table 5.1 to arrive at a sample estimator of the intraclass correlation (ICC):

$$ICC = (EMS_B - EMS_W)/(EMS_B + (a - 1)EMS_W) \quad (5.2)$$

The measure ICC in Equation 5.2 estimating ρ captures similarity of measurements within droplets relative to the variation between droplets. This measure of synchronization has two simple interpretations: (1) the correlation between cell measurements within a droplet from Equation 5.1; (2) the fraction of variation explained within droplets relative to between droplets from Table 5.1.

5.2 A deterministic quorum sensing model for the circadian oscillators

Kreuz et al.[124] have provided strong evidence that the utility of a synchronization measure depends strongly on the context for its use. Thus, we developed a relatively simple quorum sensing model of communication between cells within droplets. This model has some of the features used previously[118] and has been referred to as a mean-field model for coupled oscillators[146]. Other forms of cell to cell communication may be relevant that involve contact between cells or distance between cells[147–149]. The model is

Table 5.1: Analysis of Variance (ANOVA) of fluorescence of the *cgc-2* promoter between and within droplets is used to estimate the intraclass correlation ρ . The one-factor model is a balanced variance components model with cells grouped by droplets[143]. The number of cells in a droplet is a ; the number of droplets is n . The variance in a single fluorescent measurement is σ^2 , and the intraclass correlation is ρ . The intraclass correlation is a measure of fraction of total variation (SS_T) within droplets as well as the correlation between fluorescence measurements on different cells within the same droplet. The statistics $XBAR_i$ and $XBAR$ are the mean fluorescence in droplet i and over all droplets. The estimated mean square (EMS) is a sum of squares (SS) divided by its degrees of freedom. The EMS estimates its expectation in the last column. Setting the EMS equal to their expectations allows the solution for ρ .

Source	Degrees of freedom (df)	Sums of Square (SS)	Estimated Mean Square (EMS)	expectation of EMS
Between droplets	n	$SS_B = a \sum_i (XBAR_i - XBAR)^2$	$SS_B / (n - 1)$	$\sigma^2 + (a - 1)\rho\sigma^2$
Within droplets	$n(a - 1)$	$SS_W = \sum_i \sum_j (X_{ij} - XBAR_i)^2$	$SS_W / n(a - 1)$	$(1 - \rho)\sigma^2$
Corrected droplets	$na - 1$	$SS_T = \sum_i \sum_j (X_{ij} - XBAR)^2$		

summarized in Figure 5.1. Only a few parts in Equation 5.3 (in Figure 5.1 red) are new additions to a previously working model ensemble for the clock[120]:

$$\begin{aligned}
\frac{d[wc - 1^0]}{dt} &= 0 \\
\frac{d[wc - 1^{r0}]}{dt} &= S1 * [wc - 1^0] - D1 * [wc - 1^{r0}] - C1 * [wc - 1^{r0}] * [FRQ] \\
\frac{d[wc - 1^{r1}]}{dt} &= C1 * [wc - 1^{r0}] * [FRQ] - D7 * [wc - 1^{r1}] \\
\frac{d[WC - 1]}{dt} &= L1 * [wc - 1^{r1}] - D4[WC - 1] \\
&\quad - (C2 - C4 * [S_j]) * [WC - 2] * [WC - 1] \\
\frac{d[wc - 2^0]}{dt} &= 0 \\
\frac{d[wc - 2^r]}{dt} &= S2 * [wc - 2^0] - D2 * [wc - 2^r] \\
\frac{d[WC - 2]}{dt} &= L2 * [wc - 2^r] - D5 * [WC - 2] \\
&\quad - (C3 - C4 * [S_j]) * [WC - 2] * [WC - 1] + P * [WCC] * [FRQ]^4 \\
\frac{d[frq^0]}{dt} &= -A * [frq^0] * [WCC]^4 + Abar * [frq^1] \\
\frac{d[frq^1]}{dt} &= A[frq^0] * [WCC]^4 - Abar * [frq^1] \\
\frac{d[frq^r]}{dt} &= S3 * [frq^0] + S4 * [frq^1] - D3[frq^r] \\
\frac{d[FRQ]}{dt} &= L3 * [frq^r] - D6 * [FRQ] \\
\frac{d[WCC]}{dt} &= -n * A * 4 * [frq^0] * [WCC]^4 + n * Abar * [frq^1] - D8 * [WCC] + \\
&\quad (C2 - C4[S_j]) * [WC - 2] * [WC - 1] - P * [WCC] * [FRQ]^4 \\
\frac{d[ccg^0]}{dt} &= -A_c[ccg^0] * [WCC]^4 + B_c * [ccg^1] \\
\frac{d[ccg^1]}{dt} &= A_c[ccg^0] * [WCC]^4 - kb20 * [ccg^1] * [WCC]^4 - B_c * [ccg^1] \\
\frac{d[ccg^r]}{dt} &= S_c * [ccg^1] - D_{cr} * [ccg^r] \\
\frac{d[CCG]}{dt} &= L_c * [ccg^r] - D_{cp} * [CCG] \\
\frac{d[S_j]}{dt} &= -D9 * [S_j] + k_{S1} * [CCG] + \eta * (-[S_j] + [S_e]) \\
\frac{d[S_e]}{dt} &= -D10 * S_e + \eta_{ext} * \sum([S_j] - [S_e])
\end{aligned} \tag{5.3}$$

where $kb20 = 0$, $D2 = 0.0001$, $\eta = 100$, $\eta_{ext} = 1.44$, $D9 = 26$, $D10 = 4$, $C4 = 0.8$, $k_{S1} = 5 \times 10^9$. A source for the remaining coefficients is given in the legend of Figure 5.1. There is an implicit index $j = 1, \dots, a$ on all species in Equation 5.3, and the sum in the last equation is over all cells in a single droplet. Also the parenthetical terms including $C2$ and $C4$ are implicitly multiplied by a Heaviside step function to keep them non-negative. This quorum sensing model (Figure 5.1A) is based upon a mean-field assumption of instantaneous and uniform diffusion of the signaling molecule (sometimes referred to as the autoinducer) within a droplet. In our model, this signal is formed by a “*clock-controlled gene (ccg)*” and is, consequently, an oscillating output driven by the central clock network specified by Equation 5.3. This signal moves into and out of the cell at rates (η and η_{ext}) dependent upon the relationship between internal and external signal concentration ($[S_j]$ and $[S_e]$, respectively) as well as based upon the difference in volume of the cell compared to its droplet microenvironment (incorporated into the ext parameter). The signal in the media decays at a rate $D10$. There are a number of possible models for how the signal interacts with the oscillator in each cell[150]. When the model in Equation 5.3 is linearized, it then becomes similar to the repressilator[120]. This fact suggested that the coupling of cells might be taken to be similar to that of coupled repressilators[142]. A remaining question is what clock gene interacts with the incoming signal. The WCC complex interacts with Flavin Adenine Dinucleotide or FAD to receive the light signal and has a number of additional domains that may interact with other incoming signals[151]. These facts suggested WCC as the interactor with the hypothesized quorum sensing signal in Equation 5.3. The sign of the interaction was determined by the relative ease of synchronizing oscillators in different cells by using the signal to inhibit

WCC production. The signal within a cell interacts with $[WC - 1]$ and $[WC - 2]$ in Equation 5.3 in order to slow the formation of $[WCC]$ which slows the production of $[CCG]$ and $[S_j]$, thereby closing a coupling negative feedback loop.

Two classes of negative feedback models have been used for circadian rhythms, protein sequestration models and Hill Type transcriptional repression models[153]. In protein sequestration models it is assumed that the repressor (FRQ homolog) binds stoichiometrically in a 1:1 ratio with the transcriptional activator(s) (WCC homolog). In Hill Type transcriptional repression models the repressor (FRQ homolog) binds upstream of the activator as a multimer. These Hill Type models have been argued to be similar in structure to models with phosphorylation dependent repression of the activator[120]. Phosphorylation-dependent repression of the activator cannot currently be distinguished experimentally from the mechanism of FRQ inactivation of WCC in Equation 5.3[118]. The protein sequestration models are predicted to apply to *Drosophila* and mammals; the Hill Type models are predicted to apply to cyanobacteria and *N. crassa*[150, 153]. Each class of negative feedback models with cell-to-cell communication makes fundamentally different predictions about how the period of the single cell oscillators behave as a function of the number of communicating oscillators[153]. In protein sequestration models the mean period across single cell oscillators is predicted not to change with the number of communicating oscillators, but the variance in period across single cell oscillators should decrease with the number of communicating oscillators. In contrast with a Hill Type model the mean period across single cell oscillators is predicted to change with the number of oscillators. In mammals the prediction of stable mean period and decreasing variance in period with increasing number of communicating single cell oscillators has

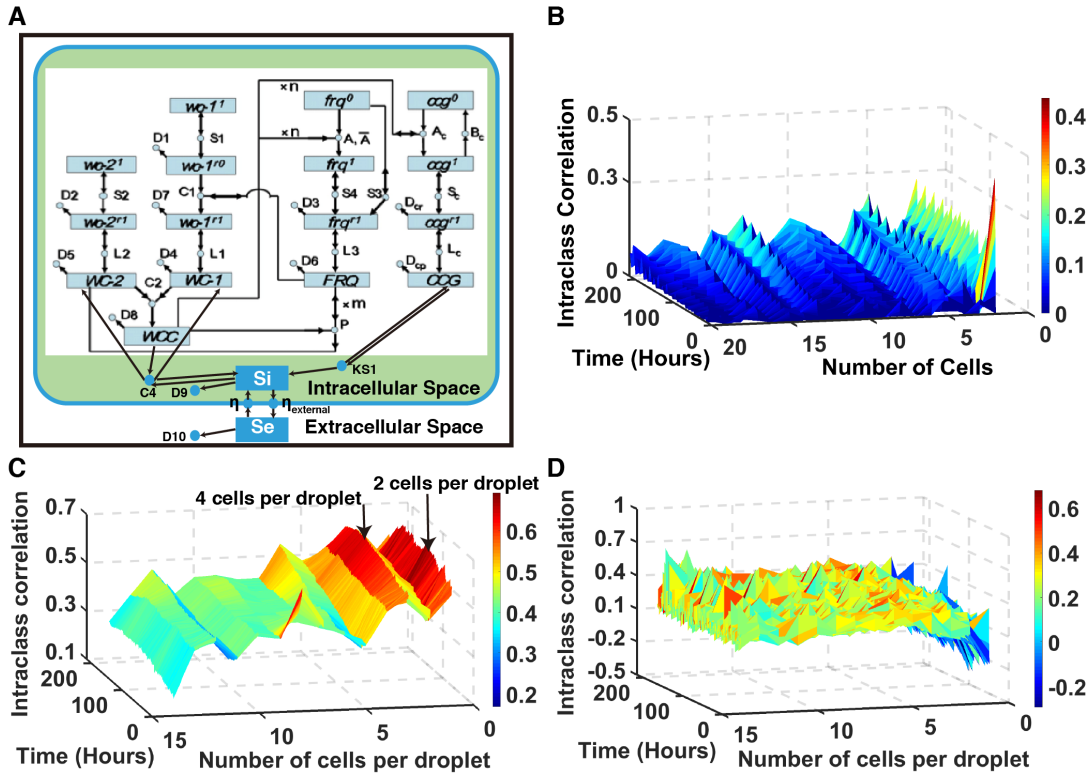


Figure 5.1: Conidial cells communicate the state of their oscillators to each other within a droplet. (A) A deterministic quorum sensing model is developed to interpret the similarity of trajectories within a droplet relative to the variation between droplets. Within each cell the oscillator network is hypothesized to be that of the working ensemble fitting the data at the macroscopic level of 10^7 cells. Boxes denote reactants and products in the network; circles denote reactions. Arrows pointing into reactions denote reactants, while arrows pointing out indicate products. Lines with arrows on both ends connect catalysts to a reaction. Reaction and molecular species labels in the network denote parameters in the model, rate coefficients and initial conditions, respectively. A new feature of the model is a clock-controlled gene (*ccg*) that makes a signaling molecule S_i within the cell, which then diffuses in or out at a rate η or η_{ext} . The signaling molecule S_i interacts with $WC - 1$ and $WC - 2$ to slow the production of WCC to synchronize the clocks of different cells. Modified from earlier network diagram[118]. (B) The synchronization surface of the quorum sensing model with new parameters given in Equation 5.3 and remaining parameters published previously[152] and released in sourceforge.net. Synchronization of cell trajectories within droplets is measured by the intraclass correlation (ICC). The ICC is shown as a function of time and number of cells per droplet for the model. (C) The ICC synchronization surface of the data on 7,903 cells is quite similar in structure to that of the quorum sensing model. (D) As a control, neighboring cells within droplets are replaced at random with strangers that have experienced no neighbors. The resulting surface has no structure, providing prima facie evidence of cell-cell communication within droplets.

been experimentally confirmed[113, 115]. The prediction for *N. crassa* was confirmed here as well in a ten day microfluidics experiment with the reference strain MFNC9 – the mean period of the single cell oscillators shifted significantly as the number of oscillators per droplet was increased (Table 5.2). The variance in period also declined significantly with the number of cells per droplet (Table 5.2), as in mammalian systems. This decline in variance in period across single cell oscillators within droplets could be understood by the examination of synchronization of these oscillators within droplets.

5.3 Synchronization of stochastic circadian oscillators

Under the null hypothesis of mean-field quorum sensing we established an expectation for the synchronization surface (Figure 5.1B) based on a working ensemble of deterministic models for the clock. We then constructed the synchronization surface for the ten day microfluidics droplet experiment involving 7,903 cells as a function of time and number of cells per droplet (Figure 5.1C). As can be seen in Figure 5.1C, the synchronization surface was quite similar to that of the mean-field quorum sensing model. Both surfaces (Figure 5.1B,C) increase along the time axis for an even number of cells per droplet. It is natural to ask whether or not this synchronization surface is real and significant. First, as a confirmation we replicated the experiment leading to the synchronization surface (Figure 5.1C) with over 25,000 cells, producing a surface of similar structure from >12 million time points (Figure 5.5). As another control for each droplet with more than one cell, the fluorescence value was replaced randomly with replacement by the fluorescence value of a singleton at the same time point. At each time point the minimum number of singletons in the pool was 193. This sampling with

Table 5.2: The mean period of single cell oscillators within a droplet increases significantly with the number of cells per droplet at two major frequencies in the periodogram, and the variance in period among single cell oscillators within a droplet decreases significantly with the number of cells per droplet at two major frequencies in the periodogram. Each single cell oscillator was examined at two frequencies in the periodogram, the frequency with the highest peak (primary harmonic) and the frequency with the second highest peak (secondary harmonic). Each cell's periods were computed by determining the maximum in the periodogram and second largest maximum in the periodogram on each cell trajectory after normalization and detrending. With respect to the highest peak in the periodogram (labeled primary harmonic below) the Spearman rank correlation (r_s) of average period of cells with the number of cells per droplet (a) is $r_s = 0.3669$ ($P < 0.10$), and the Spearman rank correlation (r_s) of variance of period within a droplet with the number of cells per droplet is $r_s = -0.6316$ ($P < 0.01$)[122]. With respect to the second highest peak in the periodogram (labeled secondary harmonic) the Spearman rank correlation (r_s) of average period of cells with the number of cells per droplet (a) is $r_s = 0.7083$ ($P < 0.005$)[122], and the Spearman rank correlation (r_s) of variance of period within a droplet with the number of cells per droplet is $r_s = -0.7083$ ($P < 0.005$)[122]

Number of cells/Droplets (a)	Primary harmonic		Secondary harmonic	
	Mean of period	Variance of period	Mean of period	Variance of period
1	16.357	57.06	9.077	56.095
2	16.608	52.225	9.3168	53.431
3	16.18	53.93	9.3788	52.724
4	16.426	53.351	10.025	52.699
5	17.068	50.007	10.468	52.338
6	16.504	49.729	10.267	49.443
7	16.324	47.549	10.115	47.244
8	16.23	51.906	9.708	47.59
9	16.537	51.911	10.065	49.642
10	16.701	50.377	10.539	47.125
11	16.206	55.129	10.424	48.35
12	17.034	41.147	10.86	44.434
13	16.388	46.923	10.171	47.247
14	16.768	45.904	10.725	46.066
15	17.214	42.897	11.502	42.188
16	17.146	46.499	10.893	53.131
17	17.445	37.217	11.106	42.044
18	16.879	53.687	9.6857	52.153
19	16.853	49.419	10.92	40.386
20	16.129	39.879	10.628	24.815

replacement was done for all droplets with multiple cells at all time points. In other words, neighbors were replaced with strangers in each droplet. The result was the synchronization surface in Figure 5.1D. There was no structure to this surface, unlike Figure 5.1B,C. This synchronization surface was replicated 20 times, replacing neighbors with strangers, with the same result. This is prima facie evidence that the cells within droplets are communicating. There were several other interesting features to the synchronization surface Figure 5.1C. For certain droplets with a specified number of cells, there was an upward trend in time in the intraclass correlation, as might be expected as synchronization evolves.

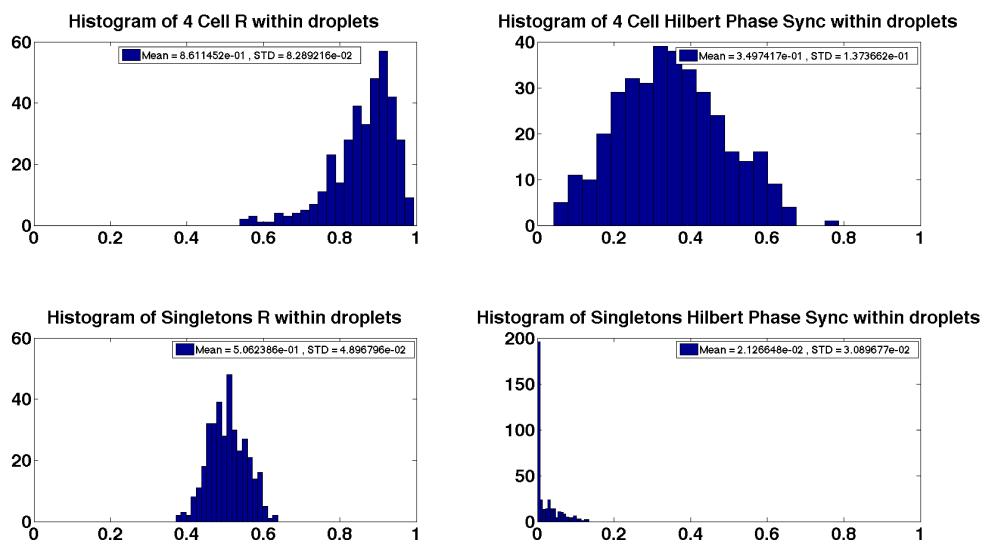


Figure 5.2: The synchronization as measured by the “order parameter” R in [142] or Hilbert transform phase synchronization [124] are high along the ridge formed at 4 cells per droplet in the Synchronization Surface, shown in Figure 5.1C, and they are low when neighbors are replaced with strangers. The figures on the top row, (A) and (B), are from the 4-cell droplet data subset of the main experiment involving 7,903 cells, as shown in Figure 5.1C. The bottom row, (C) and (D), is for the control experiment in which neighbors are replaced with strangers.

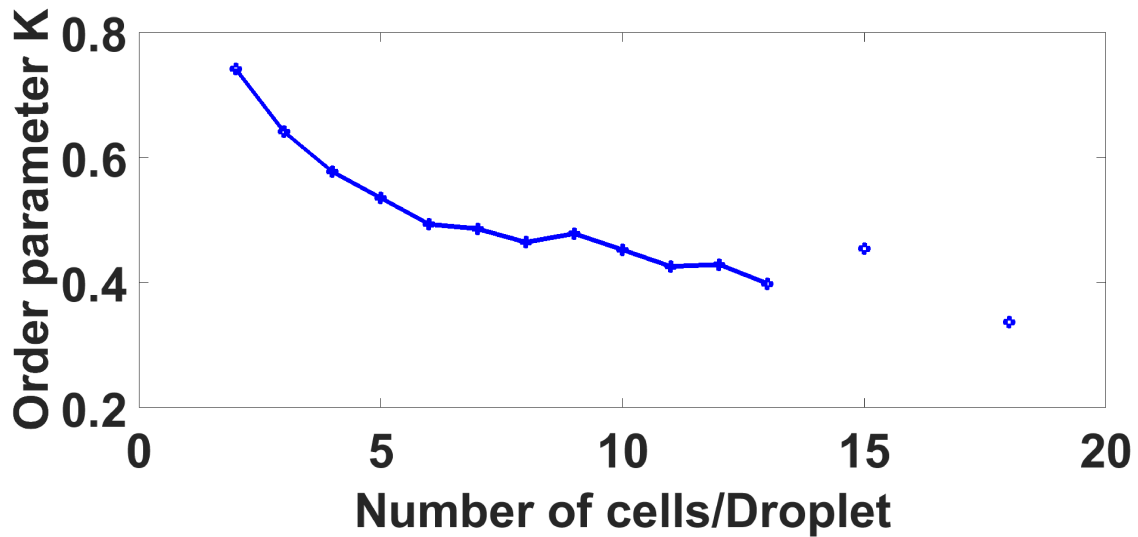


Figure 5.3: The Kuramoto order parameter K displays an alternating structure with number of cells per droplet and substantial coherence between oscillators. The order parameter K is the mean absolute deviation of oscillators phases[154]. The phase was computed about zero by removing the mean, extracting the discrete Hilbert Phase, and continuizing the discrete Hilbert phase as described in the legend of Figure 4.3.

We examined how this synchronization surface may be originating. Using sampling with replacement of neighbors by strangers again, we found that the more traditional measures of phase synchronization behaved as expected between the experiment (Figure 5.1C) and control (Figure 5.1D). Along the ridges of Figure 5.1C of 2 or 4 cells per droplet, the synchronization measure of Garcia-Ojalvo et al.[142] or of Kreuz[124], was high, Figure 5.2, but hovered around 0.5 or 0, respectively for the control with strangers replacing neighbors. The Kuramoto order parameter K (i.e., another synchronization measure) also displayed the ridges and coherence of the single cell oscillators (Figure 5.3), but was less informative than the ICC surface[154]. This order parameter K involves time averages over each droplet with a particular number of cells (a) that eliminate the structure visible in the time dimension of the ICC surface. There was also a ridge and valley structure

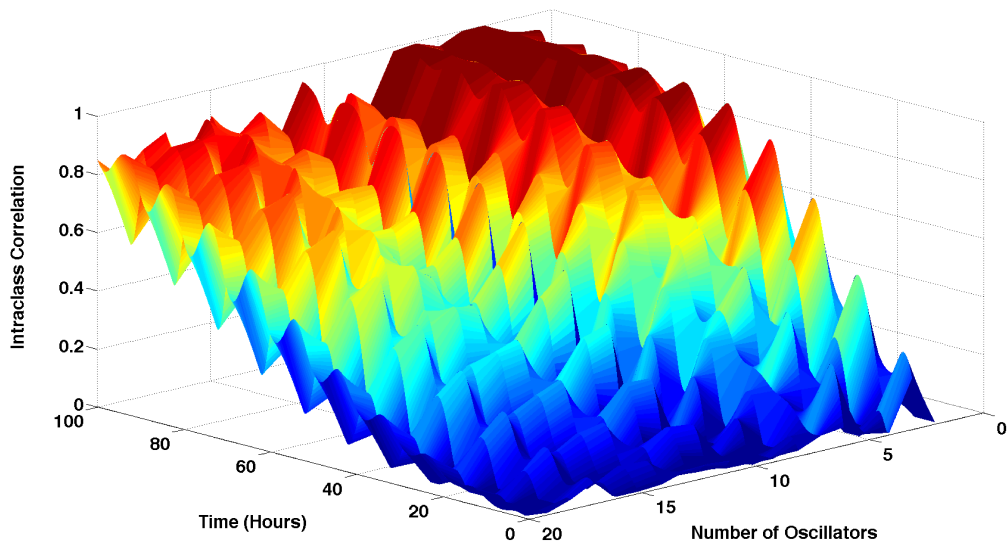


Figure 5.4: The synchronization surface for the Kuramoto phase-locking model[155] as a function of time and the number of oscillators. The model is defined by the equations: For $s \in [1, N]$, $\dot{\varphi}_s = \omega_s + \frac{K}{N} * \sum_{r=1}^N \sin(\varphi_r - \varphi_s)$. The parameters are $\omega_s = \frac{2\pi}{20}$, $K=0.05$

to the synchronization surface (ICC) both for the model and data. It is clear that we can measure synchronization with the microfluidics droplet platform and that the behavior of cells varies not only with time but neighborhood size as well.

As a final control on the choice of synchronization measure ICC in Equation 5.2, we let the dynamics of each cell's fluorescence be governed by the classic Kuramoto phase-locking model with the data structure of the primary ten day experiment[155]. The resulting synchronization surface Figure 5.4 looked very similar to the data and quorum sensing model in Figure 5.1B with a little delay to synchronization due to a local phase-locking assumption in the Kuramoto model.

The synchronization surface (ICC) is a reaction norm, which is not only a function of the “social environment” of a cell through neighborhood size, but also of genotype. In a genetic screen we have identified a gain-of-function mutation that

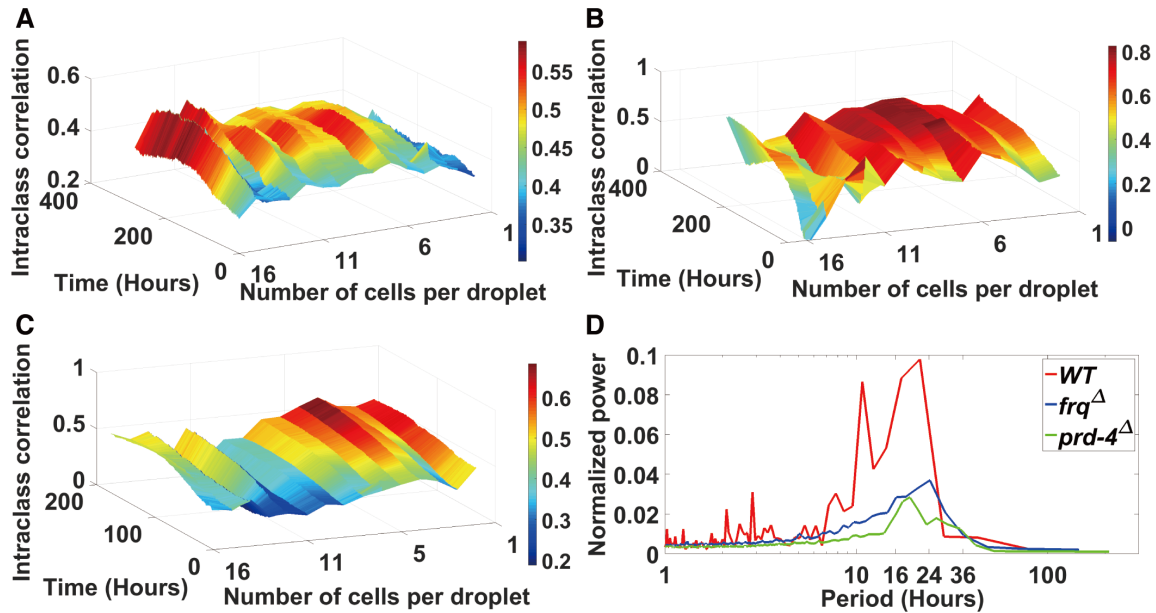


Figure 5.5: The synchronization surface (ICC) is a function of genotype. (A) A replicate of the ICCs surface with >25,000 cells was constructed [144] and resembles Figure 5.1B. (B) The deletion of *prd-4* in *prd-4*Δ, *cgg-2p:mCherry* results in increased synchronization. (C) The deletion of the oscillator *frq*Δ, *cgg-2p:mCherry* leads to a more even synchronization surface. (D) The power at 21 h in the average periodogram over singletons for the *frq*Δ is reduced 3-fold relative to MFNC9, but is not eliminated, suggesting a FRQ-less oscillator. Period (Hours) is plotted on a log scale.

increases synchronization. The gain of function mutation is from the knockout, *prd-4*Δ, *cgg-2p:mCherry*. As previously reported [156], this mutant reduces the period by 3 h to 19 h (Figure 5.5D). Some single cell trajectories are also given (Figure 5.6). This gene probably acts as a checkpoint kinase in mitosis [156] (and hence affects conidiation over time, the main clock phenotype assayed in race tubes). Our initial hypothesis is that *prd-4* acts to monitor for DNA damage, a quality control operation that likely introduces a delay between cells. The result is some asynchronization. In *prd-4*Δ, *cgg-2p:mCherry* there is no such delay introduced, and much higher synchronization is achieved at the cost of no proof-reading of the genome (Figure 5.5A vs. Figure 5.5B). In contrast *frq*Δ, *cgg-2p:mCherry*

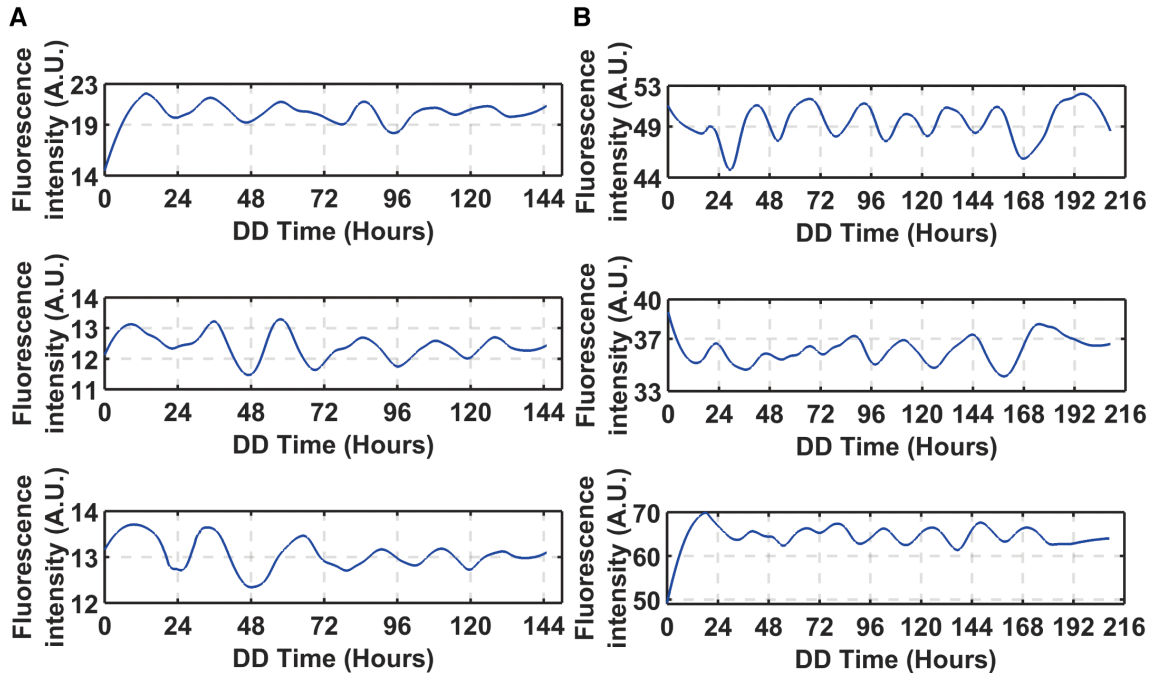


Figure 5.6: Randomly picked trajectories of (A) *frq* Δ , *ccg-2p:mCherry* and (B) *prd-4* Δ , *ccg-2p:mCherry* over 144 and 216 h, respectively. These trajectories are normalized, detrended, and smoothed by the smooth function in MATLAB with 'rloess' method.

In contrast *frq* Δ , *ccg-2p:mCherry* knockout has a period of 24 h, and the synchronization surface is responding to a loss of clock function. The *frq* Δ , *ccg-2p:mCherry* was confirmed not to band in race tubes. Synchronization surface looks more even than the MFNC9 genotype (Figure 5.5C vs 5A or 5B). Consistent with experiments done on *Synneococcus elongatus*, knockout of a clock gene does not completely remove oscillations, only reduces their power by 3-fold (Figure 5.5D)[157]. Some examples of *frq* Δ , *ccg-2p:mCherry* trajectories with low amplitudes are given (Figure 5.6). This outcome is consistent with earlier data suggesting a second weaker oscillator in *N. crassa* other than the one that is FRQ based. In this case the residual synchronization may be due to another FRQ-less oscillator[158]. Alternatively, the FRQ-based oscillator may be orchestrating cell-to-cell synchronization in a light response

and may be secondary to the FRQ-less oscillator[159]. This alternative hypothesis cannot be ruled out at this stage as well.

The significance of genotypic differences in synchronization (ICC) can be assessed by plotting one genotype's synchronization surface against another genotype's surface (Figure 5.7). The plots in Figure 5.7 are based on a total of 50 million time points. The synchronization values are organized into stripes of different numbers of cells per droplet (i.e., a). For example, the ICC surface of *prd-4* Δ , *ccg-2p:mCherry* is seen to reach much higher ICC values than the reference strain MFNC9 (Figure 5.7B vs. Figure 5.7A). Significance can be assessed by regressing the ICC surface on another ICC surface. Regressing replicate 2 (Figure 5.5A) on replicate 1 (Figure 5.1C) allows us to capture the stochastic variability in the measurements with Figure 5.7A acting as a negative control for comparisons of other genotypic ICC surface pairs. These regressions (Figure 5.7) capture at least 60% of the variation in a particular surface, depending on the surfaces compared (Table 5.3). From the regression of surface $y = ICC_2$ on $x = ICC_1$, the mean value of synchronization measure (ICC_2) with standard errors can be computed as a function of the number of cells per droplet (a) (Table 5.3). The 95% confidence intervals about the mean synchronization (ICC) for a given number of cells per droplet (a) in Table 5.3 are non-overlapping in comparing *prd-4* Δ , *ccg-2p:mCherry* (Figure 5.7B) and replicate 2 of MFNC9 (Figure 5.7A) and hence highly significant. From the comparison of these plots we also see that different genes lead to different levels of variation in synchronization relative to the reference surface (Figure 5.1C). For example, not only does *prd-4* Δ , *ccg-2p:mCherry* reach higher levels of synchronization (Figure 5.7B) there is also more variation in synchronization than that in the reference strain MFNC9 (Figure 5.7A).

Table 5.3: The intraclass correlation surface (ICC) for *prd-4Δ,ccg-2p:mCherry* is significantly different from that of MFNC9. To assess this one ICC surface (y) was regressed on another ICC surface (x), and the following relation $y = mx + b_a$ was fit by least squares to the plots in Figure 5.7. In each fit a constant slope (m) and intercept ($b - a$), which varies with the number of cells per droplet (a), was assumed. The regression R^2 summarizes the fraction of variation in the data captured by the linear regression of y on x . The mean ICC values are reported for droplets of even sizes (a) from 2 to 16 cells per droplet.

y	x	\hat{y}_2	\hat{y}_4	\hat{y}_6	\hat{y}_8	\hat{y}_{10}	\hat{y}_{12}	\hat{y}_{14}	\hat{y}_{16}	R^2
MFNC9 -rep2	MFNC9 -rep1	0.29	0.36	0.49	0.49	0.51	0.56	0.44	0.31	0.70
$2 \times$ Standard error (SE)		0.006	0.006	0.004	0.004	0.004	0.004	0.004	0.006	
<i>prd-4Δ</i>	MFNC9 -rep1	0.40	0.48	0.82	0.70	0.72	0.49	0.53	0.57	0.61
$2 \times$ SE		0.016	0.016	0.010	0.010	0.010	0.014	0.010	0.018	
<i>frqΔ</i>	MFNC9 -rep1	0.37	0.36	0.60	0.50	0.40	0.56	0.50	0.29	0.84
$2 \times$ SE		0.012	0.010	0.006	0.006	.0008	0.006	0.006	0.012	

The experimental study of stochastic coupled oscillators in biology is largely missing, particularly in the experimental study of circadian rhythms[160]. There are at least three theories on how cells in a circadian system might synchronize.

One non-intuitive theory is that single cell oscillators may experience stochastic resonance, leading to their synchronization[128, 161, 162]. Stochastic behavior of cells in tissue culture may actually lead to increased synchronization[46]. The stochasticity in expression of single cells of *N. crassa* has been quantified here and is substantial (> 94% of the variation in single cells). Here we have shown that synchronization does depend on genotype (Figure 5.5). Under this stochastic resonance hypothesis an explanation would be needed for why some genotypes improve synchronization through varying the noise in the single cell oscillators. Here the genotype of *prd-4 Δ* is likely to act to

improve synchronization by decreasing the phase noise in the oscillators by removal of a cell cycle check- point[156]. Another non-intuitive possibility is that the removal of the checkpoint actually increases phase noise to improve synchronization. A key feature of the stochastic resonance hypothesis is that synchronization varies non-monotonically with stochastic intracellular noise and that there is a local maximum in synchronization as the stochastic noise is varied. In Figure 5.5D the periodogram signal strength near 24 h is weaker for *prd-4* Δ than for either WT or *frq* Δ (red = WT, blue = *frq* Δ , green = *prd-4* Δ), but the synchronization is higher. Let us suppose the reference strain (MFNC9) sits to the left of a synchronization maximum as a function of intracellular noise. If the reference strain (MFNC9) were then shifted to a higher intracellular noise level by the *prd-4* deletion, then we would see more synchronization, as seen (Figure 5.5B). If we consider instead the synchronization as a function of the phase noise as measured through the phase standard deviation (SD = 4.41 cycles) of the *prd-4* deletion versus that of reference strain MFNC(SD = 2.40 cycles), increased phase noise would move us towards the synchronization maximum as well. The results in Figure 5.5 are then consistent with the stochastic resonance hypothesis. There may be other genes that also act to improve synchronization through increasing the intracellular noise of single cell oscillators, such as *frq* Δ . The micro uidics droplet platform enables the quantification of the variation introduced into each single cell oscillator by a particular genotype and its effect on synchronization (Figure 5.5).

A second theory is that discrete replication events drive the coupling of circadian system and the cell cycle[163]. The circadian system could become phase-locked to the

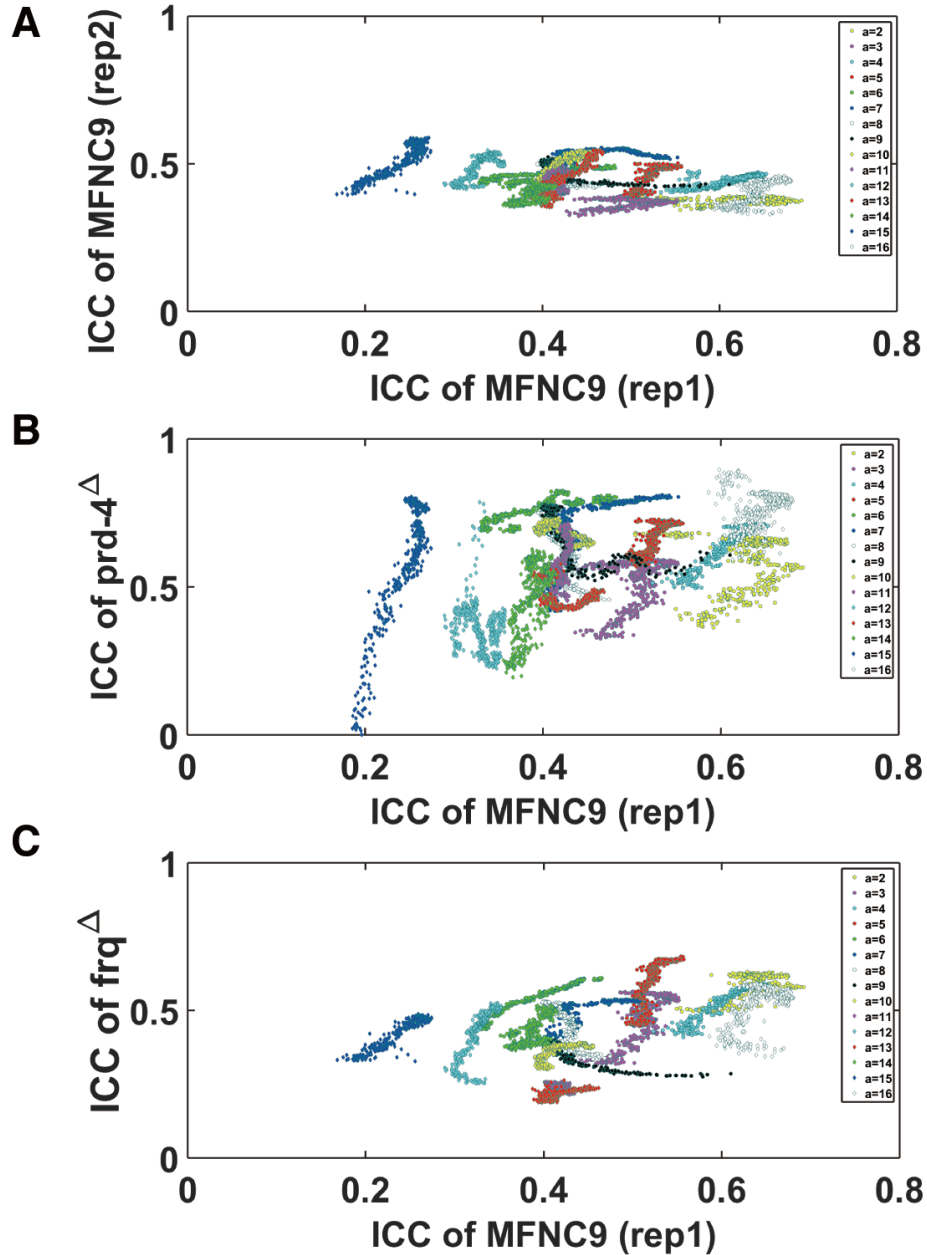


Figure 5.7: The synchronization surface for the *prd-4* knockout is significantly different from that of the reference strain, *cgg-2p:mCherry* (MFNC9). (A) Plot of replicate 2 of *cgg-2p:mCherry* (MFNC9)'s synchronization surface (ICC) in Figure 5.5A against replicate 1 of *cgg-2p:mCherry* (MFNC9)'s synchronization surface (ICC) in Figure 5.1C. This plot is the negative control. (B) Plot of *prd-4* Δ , *cgg-2p:mCherry*'s synchronization surface (ICC) in Figure 5.5B against replicate 1 of *tccg-2p:mCherry* (MFNC9)'s synchronization surface (ICC) in Figure 5.1C. (C) Plot of *freq* Δ , *cgg-2p:mCherry*'s synchronization surface (ICC) in Figure 5.5C against replicate 1 of *cgg-2p:mCherry* (MFNC9)'s ICC synchronization surface in Figure 5.1C.

cell cycle. The evidence against this theory of synchronization is that the cells in this study do not experience any cell division.

A final theory of synchronization favored here is that cells communicate the state of their clocks through some communication mechanism, such as quorum sensing[146] (Figure 5.1A). We have provided strong evidence that conidial oscillators communicate the state of their oscillators within droplets (Figure 5.1C and Figure 5.5A). A prediction of this model is that as the number of cells per droplet (a) increases, one should observe a rise in synchronization[142]. A trend of this sort is seen in Table 5.3. Another prediction of this theory is the structure of the synchronization surface (ICC) (Figure 5.1B), which resembles that measured (Figure 5.1C). The alternating structure to synchronization with an even number of cells per droplet versus an odd number of cells per droplet is a new phenomenon. We eliminated the cause being the synchronization measure (Figure 5.2). We also found this alternating structure in different models describing the data (Figure 5.5 and Figure 5.4). We anticipate further detailed analysis of the ICC surface in these models will provide an explanation for the phenomenon.

None of these mechanisms of synchronization are mutually exclusive. For example, Ulner et al.[131] combined the stochastic resonance hypothesis with quorum sensing in a model to explain cell synchronization in the suprachiasmatic nuclei under light of randomly varying intensity in mammals. Further experiments will uncover the exact mechanism of communication through manipulation of cells in their droplet environment.

There are a number of extensions needed. *N. crassa* has an interesting life cycle[164]. We have focused on single cells or conidia to take maximum advantage of high-throughput cell isolation by microfluidics to measure fluorescence on 25,000 cells

simultaneously over ten days (Figure 5.5A). We selected a media so that cells did not germinate, divide, or fuse. It is in this stage that we were able for the first time to demonstrate circadian rhythms in expression of *ccg-2* at the single cell level. These conidia can be multi-nucleate[164], and we have not examined intracellular communication, only intercellular communication. These conidia ultimately germinate and produce filaments as a subsequent life stage. Microfluidics devices in other studies also provide a tool for examination of these filaments for circadian rhythms[165]. It will be very interesting to see how the stochasticity in circadian rhythms changes at other life stages in an examination of period, phase, and amplitude variation change under intracellular communication (Figure 4.3). Even more interesting would be to examine how the synchronization surface changes as the cells divide during filamentous growth and experience both intracellular and intercellular communication. To reconstruct the synchronization surface will require on the order of 50,000,000 time points (Figure 5.7) to make such comparisons, which necessitates both high-throughput and high-resolution microfluidics measurements[165].

Palma-Guerrero et al.[148] recently described a population genetic approach through a genome-wide association study (GWAS) for isolating genes involved in cell-to-cell communication in *N. crassa*. Their GWAS produced one neuronal calcium sensor homolog (*cse-1*) and six other candidate genes. The experiments here provide a much more direct way to assay communication at the single cell level in which the environment of a droplet can be manipulated in a variety of ways. The combination of a top-down and bottom-up approach should provide a means to uncover new communication pathways between cells in fungi.

5.4 Light synchronized the circadian oscillators in *Neurospora Crassa*

From the chapter 4 we see that single cell circadian oscillators of *N. crassa* can be entrained by light. The external light signal has the effect of orchestrating the phase of the single *N. crassa* cells so that each single oscillator can more or less follow the phase of the external light signal. We then asked to what extent the light signal can synchronize the oscillators of individual isolated cells. The next questions would be whether coupling/communication between cells plays a role in the light entrainment and synchronization.

First we looked at the quality of the global response of all the single *N. crassa* cells to the external light signal. A measure of this response is given by computing the so-called spectral amplification factor R defined as in Equation 5.4[166]:

$$GR = \frac{4}{L_0^2} * | \langle e^{-i\omega t} \mathbf{X}(t) \rangle | \quad (5.4)$$

GR is the amplitude of Fourier component of the time series $\mathbf{X}(t) = \frac{1}{N} \sum_i^N X_i(t)$ at the forcing frequency ω normalized by the strength of the external force (the light intensity). N is number of oscillators and $X_i(t)$ is the fluorescence time series of each single cell oscillator. The global response for single cells in the 3 light entrainment experiments is summarized in Table 5.4.

The single cells have the strongest global response when entrained to the 12 hours artificial day as compared to the other two. When single cells were under the short 6 hours artificial day, their global response is low. This may be due to more single cells not being entrained to the period of the short LD cycles as can be seen from the mean period of the single cells under this light entrainment conditions that is much high than the period of the

Table 5.4: Global response and mean period of isolated single cells in 3 light entrainment conditions. GR is calculated as Equation 5.4 but without normalized by the light intensity since the light intensity is the same for the 3 experiment. Mean period is the average period at the maximum power of the periodogram of all the single cells.

	6 hours artificial day	12 hours artificial day	36 hours artificial day
<i>GR</i> (Global response)	8.1869	56.8550	29.0663
Mean period (+/- two standard error)	12.4994 (+/-0.4288)	12.3408 (+/-0.1547)	26.1430 (+/- 0.4813)

LD cycles (6 hours). The mean period of the single cells under the long LD cycles (the 36 hours artificial day) is ~ 26 , that is, also far away from the period of the corresponding LD cycles. A similar calculation of global response was done on single cells under constant dark (DD) condition as a control by calculating the amplitude of Fourier component of the average time series of all single cells at the intrinsic circadian period/frequency. The result is 0.048. This value is much smaller as expected. Because under DD, without external forcing, isolated single cells' clocks will drift out of phase with each other likely due to stochastic noise in gene expression and therefore their clock phase can cancel out each other when averaging their clocks. The range of entrainment of the circadian clock is demonstrated to be determined by its intrinsic period of the clock, its amplitude relaxation rate, and by the ratio between external force (zeitgeber) strength and amplitude of the clock[132]. Here we see that when the external force has a too short or too long period than the intrinsic period of the single cells oscillator, single cells are less likely to be entrained.

The LD cycles in light entrainment seems to orchestrate the phase of single cells by limiting phase drifting introduced by stochastic noise. We then want to know the degree of phase synchrony among single cell oscillators themselves under light entrainment. One

way to measure phase synchronization is to calculate the phase locking value between pairs of cells[124]. The phase locking value for two oscillators oscillating at the same frequency is defined as in Equation 5.5:

$$\gamma = \left| \frac{1}{N} \sum_{j=1}^N e^{i*[\phi_x(t_j) - \phi_y(t_j)]} \right| \quad (5.5)$$

N is the number of cells, $\phi_x(t_j)$ and $\phi_y(t_j)$ is the phase of cell x and cell y at time t_j . A phase locking value of 0 indicates no phase synchronization, *i.e.* the phase relationship of two cells change randomly over time. A phase locking value of 1 indicates perfect phase locking between the two cells with their phase difference being constant over time. Table 5.5 shows the average phase locking value between possible pair of cells of all the single cells in the 3 light entrainment experiments. Under DD, isolated single cells phase locking value is the lowest here as a comparison to that under LD cycles. The phase locking value of single cells under 12 hours cycle light entrainment has the highest value as compared to those under the 6 hours and 36 hours cycle light entrainment. This means that the single cells' clock under the 12 hours period light entrainment response to the light/dark signal more coherently than that under the other two light entrainment with more extreme cycles (much shorter or longer than the intrinsic period of *N. crassa* clock).

Another synchronization measurement that quantifies phase synchronization of a group

Table 5.5: Phase locking value of single cells in 3 light entrainment conditions

	DD	6 hours artificial day	12 hours artificial day	36 hours artificial day
γ (+/- two standard error)	0.0621 (+/- 4.10E-05)	0.1257 (+/- 9.97E-05)	0.2413 (+/- 1.40E-04)	0.1502 (+/- 09.67E-05)

of oscillators is the Kuramoto order parameter[154]. The Kuramoto order parameter, K , defined in Equation 5.6 captures the level of synchrony of a collection of oscillators by calculating time averaging phase variance among the oscillators.

$$K = \langle | N^{-1} \sum_j^N \exp(i\theta_j) - \langle N^{-1} \sum_j^N \exp(i\theta_j) \rangle | \rangle \quad (5.6)$$

N is the number of of the oscillators, θ_j is the phase of the j th oscillator. The angle brackets means a time average. The Kuramoto order parameter is 0 if all the oscillators are out of phase with each other and 1 when all the oscillators are perfectly in phase, meaning they have exactly the same phase at all times. Table 5.6 summarizes the Kuramoto order parameter K for all 3 light entrainment experiments. The single cell oscillators of *N. crassa* entrained under the LD cycles of 12 hours period shows the highest Kuramoto order parameter. This says that these oscillators have less phase variance as a population than the others. The Kuramoto order parameter for single cells under DD is the lowest as compared to those entrained under varied LD cycles. Periodic LD cycles entrain the single cell circadian oscillators of *N.crassa* and has the effect to synchronize them to be in phase with each other. So far we have looked at the light entrainment and synchronization

Table 5.6: Kuramotor order parameter of single cells in 3 light entrainment conditions

	DD	6 hours artificial day	12 hours artificial day	36 hours artificial day
K	0.0909	0.3007	0.4208	0.3272

effect on *N. crassa* at the single cell level. Below, we aim to study the cell-to-cell communication or cell-cell coupling effect on the light entrainability or light response of *N. crassa*. For SCN, external light signal influences the neuronal synchronization by means

of neurotransmitters that are responsible for the coupling between cells in the SCN[166]. An interesting mechanism proposed by Gonze *et al.* suggests that interneuronal coupling transforms SCN into damped oscillators that can then be easily entrained by external forcing[167]. Some also have shown that right amount of heterogeneity in the intrinsic periods of the oscillators facilitates the response of coupled neuronal system to the external light-dark forcing[166]. Coupling is demonstrated to be governing the entrainment range of a circadian clock, which explained experimental findings that lung clocks entrained to extreme zeitgeber cycles, whereas SCN clocks do not[132]. These studies all point to the fact that cell-cell coupling has an effect on the light entrainment of SCN. Single neuron oscillates with a period ranging from 20 to 28 hours, which is different from single *N. crassa* oscillating with a period ~ 21 -22 hours. However, *N. crassa* has substantial phase and amplitude heterogeneity in their clocks at the single cell level as demonstrated in the previous chapter. It would be very interesting to see what effect coupling has on the phase, amplitude and synchrony of the clock of *N. crassa* cells under light entrainment conditions.

First we would want to look at how the amplitude of the oscillators affected by the coupling strength. Here the coupling strength is associated with the number of cells per droplet. A mechanism relating coupling with entrainability of SCN were proposed by Gonze *et. al*[146] and Bernard *et. al*[168]. They found that coupling induces damping in individual oscillators, enabling efficient synchronization and entrainment by LD cycles[146]. A similar mechanism has been hypothesized elsewhere, the effect of neuron heterogeneity is stressed, and also that inter neuronal heterogeneity is enough to damp the neuron oscillation and bring the coupled system to a steady state where it can be easily entrained[166]. These theories suggest that entrained oscillators are those whose

amplitude is reduced with coupling strength due to them being brought to a damping state by coupling and heterogeneity when there is no external forcing. Therefore we hypothesize that the amplitude of entrained cells will decrease as number of cells per droplet increase. Table 5.7 shows the mean amplitude of all the cells (amplitude at the maximum periodogram value) as the number of cells per droplet increases from 2 to 10 for the 3 hours light on and 3 hours light off entrainment condition. There is no significant relationship between the amplitude of all cells (including entrained cells and non-entrained cells) and number of cells per droplet. Yet the entrained cells' amplitudes are negatively correlated with number of cells per droplet. This correlation is consistent with our hypothesis. The non-entrained cell amplitude is positively correlated with the number of cells per droplet. For cells under 6 hours light on and 6 hours light off cycles and the 18 hours light on and 18 hours light off cycles (Table 5.8, Table 5.9), the entrained cells amplitude also shows a negative relationship with the number of cells per droplet while the amplitude of non-entrained cells show no significant change as number of cells per droplet increases. Also shown in Table 5.7, Table 5.8 and Table 5.9 is that the Global Response (GR) does not significantly change with the increase in the number of cells per droplet while the Global Response of cells within the same droplet (GR_W) behaves differently. However, GR_W is larger than GR for all number of cells per droplet. This indicates that cells within the same droplet have a more coherent response to the external light signal than cells in different droplets. Here, coupling among cells within the same droplet plays a positive role in improving the global response of the cells to the external light signal.

Besides global response to the external signal, we also want to look directly at the phase synchronization among coupled *N. crassa* oscillators. The phase locking value and

Table 5.7: Amplitude and Global Response (Equation 5.4) of *N. crassa* with different neighboring cells in a droplet (number of cells per droplet) in the 3 hours light on 3 hours light off condition. Mean amplitude is the average of amplitude at the maximum periodogram power for each cell. Amplitude of entrained cells, AE , is the amplitude of cell that has a maximum periodogram value at the same period as the LD cycles. Amplitude of non-entrained cells, NAE , is the amplitude of cell that has a maximum periodogram value at a different period than the period of the LD cycles. For Global response, GR is calculated as describe in Table 5.4 by first averaging the fluorescence intensity time series of all the cells corresponding to the droplets with the same number of cells. For GR_W , GR for cells in each droplet was calculated individually by only averaging the fluorescence intensity time series of cells in the same droplet and then all the GR for the droplets with the same number of cells was averaged to get GR_W . The correlation coefficient (r) of amplitude with the number of cells per droplet is $r = 0.0139$ ($P = 0.5067$), the correlation coefficient (r) of entrained cells amplitude, AE , with the number of cells per droplet is $r = -0.1006$ ($P = 0.008$), the correlation coefficient (r) of non-entrained cells amplitude, NAE , with the number of cells per droplet is $r = 0.0516$ ($P = 0.0408$), the correlation coefficient (r) of GR with the number of cells per droplet is $r = -0.1682$ ($P = 0.6653$), the correlation coefficient (r) of GR_W with the number of cells per droplet is $r = 0.0224$ ($P = 0.9543$).

Number of cells per droplet	Mean amplitude (+/- two standard error)	AE (+/- two standard error)	NAE (+/- two standard error)	GR (Global Response)	GR_W (Global Response)
2	3.2089 (+/- 0.4102)	3.2467 (+/- 0.5978)	3.1952(+/- 0.5156)	13.9821	40.0503
3	2.2514 (+/- 0.1577)	2.4323 (+/- 0.2555)	2.1794(+/- 0.1954)	8.3889	39.4520
4	2.5637 (+/- 0.2664)	2.8218 (+/- 0.5367)	2.4558(+/- 0.3034)	12.5032	37.2256
5	2.4090 (+/- 0.3367)	2.3393(+/- 0.4043)	2.4494(+/- 0.4780)	9.7214	41.9378
6	2.8450 (+/- 0.4031)	2.5118(+/- 0.6004)	3.0167(+/- 0.5257)	13.2791	46.9263
7	2.1840 (+/- 0.3874)	2.1537(+/- 0.5321)	2.2020(+/- 0.5333)	8.2437	40.2727
8	4.3430 (+/- 1.8612)	1.7698(+/- 0.5677)	5.7726(+/- 2.7986)	17.1218	115.7930
9	2.2716 (+/- 0.6999)	1.6601(+/- 0.6485)	2.4091(+/- 0.8417)	7.8365	22.1959
10	2.1818 (+/- 0.6725)	2.2638 (+/- 0.8334)	2.1041(+/- 1.0664)	9.5098	17.6098

Kuramoto order parameter are calculated for different numbers of cells per droplet. The Phase locking value, γ , and Kuramoto order parameter, K , are calculated for different number of cells per droplet by using all the cell data from those droplets with the same number of cells (not differentiate cells from the same or different droplets). Phase locking value, γ_W , and Kuramoto order parameter, K_W are calculated for different number of cells per droplet by first only considering the cells from the same droplet and then averaging the results from all the droplets that have the same number of cells. By only considering the cells in the same droplet before averaging the result, γ_W and K_W can eliminate the differences between droplets. γ_W , γ , K , K_W for the 3 light entrainment experiments are summarized in Table 5.10, Table 5.11 and Table 5.12. γ_W and K_W show higher values than γ and K respectively for the 3 light entrainment experiments. These results suggest that the coupling among cells in the same droplet contributes to the synchronization under light entrainment and external forcing alone here is not the only cause to the increased phase synchrony among *N. crassa*.

The ICC surfaces for cells in DD and 3 light entrainment experiments are shown in Figure 5.8. The ICC surfaces constructed from multiple cells data under the light entrainment conditions (Figure 5.8 C, E, and G) have higher values as compared to that under constant dark condition (Figure 5.8A). This indicates that light entrainment has the effect of increasing the similarity of rhythm among cells within the same droplets.

Table 5.8: Amplitude and Global Response (Equation 5.4) of *N. crassa* with different neighboring cells in a droplet (number of cells per droplet) in the 6 hours light on 6 hours light off condition. Mean amplitude is the average of amplitude at the maximum periodogram power for each cell. Amplitude of entrained cells, AE , is the amplitude of cell that has a maximum periodogram value at the same period as the LD cycles. Amplitude of non-entrained cells, NAE , is the amplitude of cell that has a maximum periodogram value at a different period than the period of the LD cycles. For Global response, GR is calculated as describe in Table 5.4 by first averaging the fluorescence intensity time series of all the cells corresponding to the droplets with the same number of cells. For GR_W , GR for cells in each droplet was calculated individually by only averaging the fluorescence intensity time series of cells in the same droplet and then all the GR for the droplets with the same number of cells was averaged to get GR_W . The correlation coefficient (r) of amplitude with the number of cells per droplet is $r = -0.0380$ ($P = 0.024$), the correlation coefficient (r) of entrained cells amplitude, AE , with the number of cells per droplet is $r = -0.0541$ ($P = 0.005$), the correlation coefficient (r) of non-entrained cells amplitude, NAE , with the number of cells per droplet is $r = -0.0037$ ($P = 0.9172$), the correlation coefficient (r) of GR with the number of cells per droplet is $r = -0.5687$ ($P = 0.1101$), the correlation coefficient (r) of GR_W with the number of cells per droplet is $r = -0.5300$ ($P = 0.1423$).

Number of cells per droplet	Mean amplitude (+/- two standard error)	AE (+/- two standard error)	NAE (+/- two standard error)	GR (Global Response)	GR_W (Global Response)
2	3.2863 (+/- 0.2865)	3.5778(+/- 0.3201)	2.5040(+/- 0.5916)	36.0518	66.9573
3	3.4324 (+/- 0.1814)	3.6159(+/- 0.2051)	2.8160(+/- 0.3769)	39.8296	53.0524
4	3.0159 (+/- 0.2175)	3.1729(+/- 0.2392)	2.5077(+/- 0.4895)	28.6044	36.3701
5	3.2923 (+/- 0.2594)	3.4605(+/- 0.2963)	2.6188 (+/- 0.5060)	37.2041	55.0610
6	3.0365 (+/- 0.2634)	3.2782(+/- 0.2976)	2.0730(+/- 0.5109)	33.2627	34.5946
7	3.2444 (+/- 0.3526)	3.3047(+/- 0.3452)	2.9688(+/- 1.1783)	34.3107	51.5447
8	2.9961 (+/- 0.2937)	3.1360(+/- 0.3312)	2.5075(+/- 0.6224)	30.6363	46.6487
9	3.0382 (+/- 0.3745)	3.1968(+/- 0.4063)	2.5783(+/- 0.8560)	29.3276	44.4677
10	3.1060 (+/- 0.4065)	3.1462(+/- 0.4238)	2.9605(+/- 1.1063)	31.9273	39.1778

Table 5.9: Amplitude and Global Response (Equation 5.4) of *N. crassa* with different neighboring cells in a droplet (number of cells per droplet) in the 36 hours light on 36 hours light off condition. Mean amplitude is the average of amplitude at the maximum periodogram power for each cell. Amplitude of entrained cells, AE , is the amplitude of cell that has a maximum periodogram value at the same period as the LD cycles. Amplitude of non-entrained cells, NAE , is the amplitude of cell that has a maximum periodogram value at a different period than the period of the LD cycles. For Global response, GR is calculated as describe in Table 5.4 by first averaging the fluorescence intensity time series of all the cells corresponding to the droplets with the same number of cells. For GR_W , GR for cells in each droplet was calculated individually by only averaging the fluorescence intensity time series of cells in the same droplet and then all the GR for the droplets with the same number of cells was averaged to get GR_W . The correlation coefficient (r) of amplitude with the number of cells per droplet is $r = -0.0277$ ($P = 0.0295$), the correlation coefficient (r) of entrained cells amplitude, AE , with the number of cells per droplet is $r = -0.0806$ ($P = 0.003$), the correlation coefficient (r) of non-entrained cells amplitude, NAE , with the number of cells per droplet is $r = -0.0165$ ($P = 0.2535$), the correlation coefficient (r) of GR with the number of cells per droplet is $r = -0.8888$ ($P = 0.001$), the correlation coefficient (r) of GR_W with the number of cells per droplet is $r = -0.6074$ ($P = 0.083$).

Number of cells per droplet	Mean amplitude (+/- two standard error)	AE (+/- two standard error)	NAE (+/- two standard error)	GR (Global Response)	GR_W (Global Response)
2	3.8171 (+/- 0.2356)	3.9953(+/- 0.3462)	3.7577(+/- 0.2922)	25.1973	46.6835
3	3.5101 (+/- 0.1903)	3.7169(+/- 0.2925)	3.4407(+/- 0.2343)	22.2537	33.4959
4	3.3673 (+/- 0.2163)	3.4732(+/- 0.3380)	3.3393(+/- 0.2585)	19.9324	35.9674
5	3.4289 (+/- 0.2186)	3.9700(+/- 0.4280)	3.3016(+/- 0.2496)	20.6158	30.7808
6	23.5276 (+/- 0.2511)	3.6092(+/- 0.4739)	3.5055(+/- 0.2924)	20.8161	38.7182
7	3.4694 (+/- 0.2456)	3.4480(+/- 0.3966)	3.4753(+/- 0.2940)	19.3970	28.5748
8	3.3410 (+/- 0.3791)	3.3680(+/- 0.4887)	3.3347(+/- 0.4536)	19.5802	33.4352
9	3.3208 (+/- 0.4427)	3.0500(+/- 0.4231)	3.3867(+/- 0.5476)	16.5947	32.2743
10	3.4415 (+/- 0.4339)	3.2435(+/- 0.5435)	3.4890(+/- 0.5222)	17.8071	31.4357

Table 5.10: Phase synchronization of *N. crassa* with different neighboring cells in a droplet (number of cells per droplet) in the 3 hours light on 3 hours light off condition. Phase locking value, γ , and Kuramoto order parameter, K are calculated for different number of cells per droplet by using all the cell data from those droplet with the same number of cells (not differentiate cells from the same or different droplets). Phase locking value, γ_W , and Kuramoto order parameter, K_W are calculated for different number of cells per droplet by first only considering the cells from the same droplet then average the results from all the droplets that has the same number of cells. The correlation coefficient (r) of γ_W with the number of cells per droplet is $r = -0.0864$ ($P = 0.1578$), the correlation coefficient (r) of K_W with the number of cells per droplet is $r = -0.3543$ ($P < 0.001$),

Number of cells per droplet	γ_W (+/- two standard error)	γ	K_W (+/- two standard error)	K
2	0.1788 (+/- 0.0982)	0.1015	0.7042 (+/- 0.0390)	0.2637
3	0.1793 (+/- 0.0736)	0.1156	0.6748 (+/- 0.0551)	0.2861
4	0.1446 (+/- 0.0667)	0.1107	0.6728 (+/- 0.0429)	0.2824
5	0.1572 (+/- 0.0773)	0.1115	0.6680 (+/- 0.0429)	0.2840
6	0.1709 (+/- 0.0754)	0.1078	0.6365 (+/- 0.0782)	0.2835
7	0.1618 (+/- 0.0867)	0.1147	0.6738 (+/- 0.0862)	0.2917
8	0.1811 (+/- 0.0623)	0.1239	0.6350 (+/- 0.0792)	0.3252
9	0.1237 (+/- 0.0403)	0.1043	0.6186 (+/- 0.0604)	0.2960
10	0.1722 (+/- 0.0302)	0.1133	0.6570 (+/- 0.0746)	0.3168

5.5 Conclusion

The circadian oscillators of different cells communicate and synchronize to overcome stochastic asynchrony. This cell-to-cell synchronization has a genetic basis because the synchronization surface varies with genotype.

The phase of single cells under light entrainment is shown to be synchronized by the external light forcing to a certain degree that the oscillations of single cells follow the external alternating light/dark signal. As cells that are under constant dark condition, cells with neighbors in the same droplet under light entrainment also communicate their states through coupling. This means coupling between cells still play an import role in coordinating the clock rhythm under light entrainment.

Table 5.11: Phase synchronization of *N. crassa* with different neighboring cells in a droplet (number of cells per droplet) in the 6 hours light on 6 hours light off condition. Phase locking value, γ , and Kuramoto order parameter, K are calculated for different number of cells per droplet by using all the cell data from those droplet with the same number of cells (not differentiate cells from the same or different droplets). Phase locking value, γ_W , and Kuramoto order parameter, K_W are calculated for different number of cells per droplet by first only considering the cells from the same droplet then average the results from all the droplets that has the same number of cells. The correlation coefficient (r) of γ_W with the number of cells per droplet is $r = -0.0480$ ($P = 0.1823$), the correlation coefficient (r) of K_W with the number of cells per droplet is $r = -0.2280$ ($P < 0.001$),

Number of cells per droplet	γ_W (+/- two standard error)	γ	K_W (+/- two standard error)	K
2	0.2523 (+/- 0.1360)	0.1911	0.7223 (+/- 0.0552)	0.3791
3	0.2333 (+/- 0.1265)	0.2079	0.6840 (+/- 0.0760)	0.3934
4	0.2106 (+/- 0.1112)	0.1839	0.6894 (+/- 0.0694)	0.3729
5	0.2362 (+/- 0.1181)	0.1998	0.6956 (+/- 0.0646)	0.3898
6	0.2319 (+/- 0.1220)	0.1992	0.6836 (+/- 0.0742)	0.3913
7	0.2371 (+/- 0.1271)	0.2041	0.6766 (+/- 0.0799)	0.4035
8	0.2378 (+/- 0.1428)	0.1924	0.6720 (+/- 0.0890)	0.3897
9	0.2127 (+/- 0.1168)	0.1833	0.6574 (+/- 0.0841)	0.3705
10	0.2227 (+/- 0.1117)	0.1883	0.6608 (+/- 0.0818)	0.3874

Table 5.12: Phase synchronization of *N. crassa* with different neighboring cells in a droplet (number of cells per droplet) in the 18 hours light on 18 hours light off condition. Phase locking value, γ , and Kuramoto order parameter, K are calculated for different number of cells per droplet by using all the cell data from those droplet with the same number of cells (not differentiate cells from the same or different droplets). Phase locking value, γ_W , and Kuramoto order parameter, K_W are calculated for different number of cells per droplet by first only considering the cells from the same droplet then average the results from all the droplets that has the same number of cells. The correlation coefficient (r) of γ_W with the number of cells per droplet is $r = -0.0660$ ($P = 0.004$), the correlation coefficient (r) of K_W with the number of cells per droplet is $r = -0.3635$ ($P < 0.001$),

Number of cells per droplet	γ_W (+/- two standard error)	γ	K_W (+/- two standard error)	K
2	0.1681 (+/- 0.1080)	0.1129	0.6887 (+/- 0.0525)	0.2724
3	0.1475 (+/- 0.0894)	0.1103	0.6306 (+/- 0.0683)	0.2662
4	0.1524 (+/- 0.0959)	0.1070	0.6478 (+/- 0.0796)	0.2586
5	0.1362 (+/- 0.0859)	0.1015	0.6142 (+/- 0.0859)	0.2483
6	0.1445 (+/- 0.0759)	0.1001	0.6090 (+/- 0.0925)	0.2477
7	0.1427 (+/- 0.0763)	0.1037	0.6048 (+/- 0.0939)	0.2548
8	0.1461 (+/- 0.0800)	0.0951	0.5770 (+/- 0.1004)	0.2393
9	0.1409 (+/- 0.0737)	0.0947	0.5743 (+/- 0.0998)	0.2388
10	0.1613 (+/- 0.0849)	0.1012	0.5713 (+/- 0.1182)	0.2479

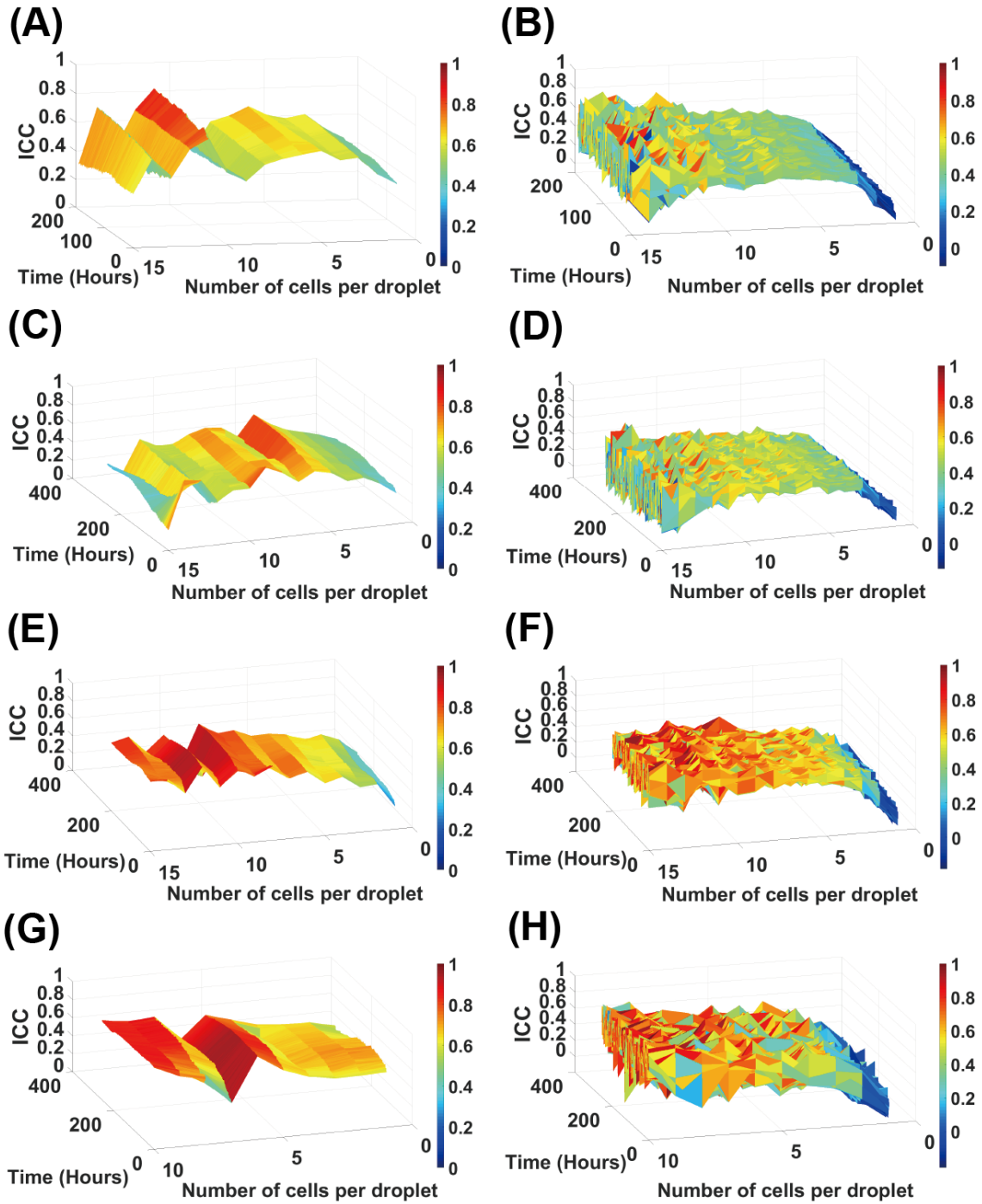


Figure 5.8: ICC surfaces of cells under 3 light entrainment conditions. (A), (C), (E), and (G) are ICC surfaces constructed from real multiple cells data. (B), (D), (F), and (H) are ICC surfaces constructed from singletons randomly sampled from the single cells data. (A) and (B) are ICC surfaces of cells under DD. (C) and (D) are ICC surfaces of cells under 18 hours light on and 18 hours light off. (E) and (F) are ICC surfaces of cells under 6 hours light on and 6 hours light off. (G) and (H) are ICC surfaces of cells under 3 hours light on and 3 hours light off.

CHAPTER 6

CONCLUSION

This dissertation presents a high-throughput microfluidic droplet platform for single-cell analysis on the biological clock of *N. crassa*. This microfluidic droplet platform overcomes several technical challenges for measuring the biological clock at the single cell level. Here it is demonstrated that > 1000 single cells of *N. crassa* can be measured up to 10 days simultaneously for their circadian rhythm. We have shown that a circadian oscillator, with a period ~ 21 hours, exists in single-cells of *N. crassa*. A biological clock consists of three major components: a circadian oscillator, light entrainment, and temperature compensation. Using this platform, we also have shown that single-cell oscillators in *N. crassa* can be light entrained, and its period can be efficiently temperature compensated. The presence of a biological clock in a single cell of *N. crassa* is demonstrated here by the first time. Cell-clusters (more than one cell in a droplet) measured by the microfluidic platform were also examined for synchronization of their circadian rhythm under LD cycles and D/D. The intraclass correlation (ICC) was used as a measurement of synchronization for multiple cells in cell-clusters across different droplets. The synchronization surface ICC provides evidence that the cells communicate the state of their circadian oscillators to each other.

Bibliography

- [1] Y. Ouyang, C. R. Andersson, T. Kondo, S. S. Golden, and C. H. Johnson. Resonating circadian clocks enhance fitness in cyanobacteria. *Proc Natl Acad Sci U S A*, 95(15):8660–4, 1998.
- [2] T. P. Michael, P. A. Salome, H. J. Yu, T. R. Spencer, E. L. Sharp, M. A. McPeck, J. M. Alonso, J. R. Ecker, and C. R. McClung. Enhanced fitness conferred by naturally occurring variation in the circadian clock. *Science*, 302(5647):1049–53, 2003.
- [3] C. P. Kyriacou and M. H. Hastings. Circadian clocks: genes, sleep, and cognition. *Trends Cogn Sci*, 14(6):259–67, 2010.
- [4] P. C. Zee and P. Manthena. The brain’s master circadian clock: implications and opportunities for therapy of sleep disorders. *Sleep Med Rev*, 11(1):59–70, 2007.
- [5] M. H. Hastings, A. B. Reddy, and E. S. Maywood. A clockwork web: circadian timing in brain and periphery, in health and disease. *Nat Rev Neurosci*, 4(8):649–61, 2003.
- [6] J. S. Takahashi, H. K. Hong, C. H. Ko, and E. L. McDearmon. The genetics of mammalian circadian order and disorder: implications for physiology and disease. *Nat Rev Genet*, 9(10):764–75, 2008.
- [7] J. Gibbs, L. Ince, L. Matthews, J. Mei, T. Bell, N. Yang, B. Saer, N. Begley, T. Poolman, M. Pariollaud, S. Farrow, F. DeMayo, T. Hussell, G. S. Worthen, D. Ray,

- and A. Loudon. An epithelial circadian clock controls pulmonary inflammation and glucocorticoid action. *Nat Med*, 20(8):919–26, 2014.
- [8] J. A. Haspel, S. Chettimada, R. S. Shaik, J. H. Chu, B. A. Raby, M. Cernadas, V. Carey, V. Process, G. M. Hunninghake, E. Ifedigbo, J. A. Lederer, J. Englert, A. Pelton, A. Coronata, L. E. Fredenburgh, and A. M. Choi. Circadian rhythm reprogramming during lung inflammation. *Nat Commun*, 5:4753, 2014.
- [9] S. Sahar and P. Sassone-Corsi. Metabolism and cancer: the circadian clock connection. *Nat Rev Cancer*, 9(12):886–96, 2009.
- [10] L. Fu and C. C. Lee. The circadian clock: pacemaker and tumour suppressor. *Nat Rev Cancer*, 3(5):350–61, 2003.
- [11] Matthew R. Blake, Scott D. Holbrook, Joanna Kotwica-Rolinska, Eileen S. Chow, Doris Kretzschmar, and Jadwiga M. Giebultowicz. Manipulations of amyloid precursor protein cleavage disrupt the circadian clock in aging drosophila. *Neurobiology of Disease*, 77(0):117–126, 2015.
- [12] Ray Zhang, Nicholas F Lahens, Heather I Ballance, Michael E Hughes, and John B Hogenesch. A circadian gene expression atlas in mammals: implications for biology and medicine. *Proceedings of the National Academy of Sciences*, 111(45):16219–16224, 2014.
- [13] Francis Lévi, Christian Focan, Abdoulaye Karaboué, Virginie de la Valette, Danielle Focan-Henrard, Benoît Baron, Françoise Kreutz, and Sylvie Giacchetti.

- Implications of circadian clocks for the rhythmic delivery of cancer therapeutics. *Advanced drug delivery reviews*, 59(9):1015–1035, 2007.
- [14] T. Danino, O. Mondragon-Palomino, L. Tsimring, and J. Hasty. A synchronized quorum of genetic clocks. *Nature*, 463(7279):326–30, 2010.
- [15] M. R. Atkinson, M. A. Savageau, J. T. Myers, and A. J. Ninfa. Development of genetic circuitry exhibiting toggle switch or oscillatory behavior in *escherichia coli*. *Cell*, 113(5):597–607, 2003.
- [16] Arthur Prindle, Phillip Samayoa, Ivan Razinkov, Tal Danino, Lev S. Tsimring, and Jeff Hasty. A sensing array of radically coupled genetic /‘biopixels/’. *Nature*, 481(7379):39–44, 2012.
- [17] F. Hussain, C. Gupta, A. J. Hirning, W. Ott, K. S. Matthews, K. Josic, and M. R. Bennett. Engineered temperature compensation in a synthetic genetic clock. *Proc Natl Acad Sci U S A*, 111(3):972–7, 2014.
- [18] M. R. Connor and S. Atsumi. Synthetic biology guides biofuel production. *J Biomed Biotechnol*, 2010, 2010.
- [19] W. Weber, J. Stelling, M. Rimann, B. Keller, M. Daoud-El Baba, C. C. Weber, D. Aubel, and M. Fussenegger. A synthetic time-delay circuit in mammalian cells and mice. *Proc Natl Acad Sci U S A*, 104(8):2643–8, 2007.
- [20] J. C. Dunlap. Molecular bases for circadian clocks. *Cell*, 96(2):271–90, 1999.

- [21] D. Bell-Pedersen, V. M. Cassone, D. J. Earnest, S. S. Golden, P. E. Hardin, T. L. Thomas, and M. J. Zoran. Circadian rhythms from multiple oscillators: lessons from diverse organisms. *Nat Rev Genet*, 6(7):544–56, 2005.
- [22] J. J. Loros, J. C. Dunlap, L. F. Larrondo, M. Shi, W. J. Belden, V. D. Gooch, C. H. Chen, C. L. Baker, A. Mehra, H. V. Colot, C. Schwerdtfeger, R. Lambreghts, P. D. Collopy, J. J. Gamsby, and C. I. Hong. Circadian output, input, and intracellular oscillators: Insights into the circadian systems of single cells. *Cold Spring Harbor symposia on quantitative biology*, 72:201–214, 2007.
- [23] Q. Yang, B. F. Pando, G. Dong, S. S. Golden, and A. van Oudenaarden. Circadian gating of the cell cycle revealed in single cyanobacterial cells. *Science*, 327(5972):1522–6, 2010.
- [24] Jeffrey R. Chabot, Juan M. Pedraza, Prashant Luitel, and Alexander van Oudenaarden. Stochastic gene expression out-of-steady-state in the cyanobacterial circadian clock. *Nature*, 450(7173):1249–1252, 2007.
- [25] I. Mihalcescu, W. Hsing, and S. Leibler. Resilient circadian oscillator revealed in individual cyanobacteria. *Nature*, 430(6995):81–5, 2004.
- [26] S. Honma, W. Nakamura, T. Shirakawa, and K. Honma. Diversity in the circadian periods of single neurons of the rat suprachiasmatic nucleus depends on nuclear structure and intrinsic period. *Neurosci Lett*, 358(3):173–6, 2004.
- [27] Steven J Altschuler and Lani F Wu. Cellular heterogeneity: do differences make a difference? *Cell*, 141(4):559–563, 2010.

- [28] D. K. Welsh, S. H. Yoo, A. C. Liu, J. S. Takahashi, and S. A. Kay. Bioluminescence imaging of individual fibroblasts reveals persistent, independently phased circadian rhythms of clock gene expression. *Curr Biol*, 14(24):2289–95, 2004.
- [29] P. O. Westermark, D. K. Welsh, H. Okamura, and H. Herzl. Quantification of circadian rhythms in single cells. *PLoS Comput Biol*, 5(11):e1000580, 2009.
- [30] E. Castro-Longoria, M. Ferry, S. Bartnicki-Garcia, J. Hasty, and S. Brody. Circadian rhythms in *neurospora crassa*: dynamics of the clock component frequency visualized using a fluorescent reporter. *Fungal Genet Biol*, 47(4):332–41, 2010.
- [31] Arjun Raj and Alexander van Oudenaarden. Nature, nurture, or chance: stochastic gene expression and its consequences. *Cell*, 135(2):216–226, 2008.
- [32] T. Lionnet and R. H. Singer. Transcription goes digital. *EMBO Rep*, 13(4):313–21, 2012.
- [33] Iain G Johnston, Bernadett Gaal, Ricardo Pires das Neves, Tariq Enver, Francisco J Iborra, and Nick S Jones. Mitochondrial variability as a source of extrinsic cellular noise. *PLoS computational biology*, 8(3):e1002416, 2012.
- [34] Ehud Shapiro, Tamir Biezuner, and Sten Linnarsson. Single-cell sequencing-based technologies will revolutionize whole-organism science. *Nature reviews. Genetics*, 14(9):618, 2013.
- [35] Jay C Dunlap and Jennifer J Loros. Analysis of circadian rhythms in *neurospora*: overview of assays and genetic and molecular biological manipulation. *Methods in enzymology*, 393:3–22, 2005.

- [36] Emi Nagoshi, Steven A Brown, Charna Dibner, Benoît Kornmann, and Ueli Schibler. Circadian gene expression in cultured cells. *Methods in enzymology*, 393:543–557, 2005.
- [37] Andrew J Tindall, Jade Waller, Mark Greenwood, Peter D Gould, James Hartwell, and Anthony Hall. A comparison of high-throughput techniques for assaying circadian rhythms in plants. *Plant methods*, 11:32, 2015.
- [38] Sean R Moore, Jill Pruszka, Jefferson Vallance, Eitaro Aihara, Toru Matsuura, Marshall H Montrose, Noah F Shroyer, and Christian I Hong. Robust circadian rhythms in organoid cultures from period2::luciferase mouse small intestine. *Disease models & mechanisms*, 7:1123–1130, September 2014.
- [39] Masato Nakajima, Keiko Imai, Hiroshi Ito, Taeko Nishiwaki, Yoriko Murayama, Hideo Iwasaki, Tokitaka Oyama, and Takao Kondo. Reconstitution of circadian oscillation of cyanobacterial kaic phosphorylation in vitro. *Science*, 308(5720):414–415, 2005.
- [40] David K Welsh, Takato Imaizumi, and Steve A Kay. Real-time reporting of circadian-regulated gene expression by luciferase imaging in plants and mammalian cells. *Methods in enzymology*, 393:269–288, 2005.
- [41] Werner Kammerloher. Bioluminescence microscopy for cellular level circadian analysis in the suprachiasmatic nucleus. *Nature Methods*, 5(11), 2008.
- [42] Kurt R Zinn, Tandra R Chaudhuri, April Adams Szafran, Darrell O’Quinn, Casey Weaver, Kari Dugger, Dale Lamar, Robert A Kesterson, Xiangdong Wang, and

- Stuart J Frank. Noninvasive bioluminescence imaging in small animals. *ILAR journal*, 49(1):103–115, 2008.
- [43] Clare Guilding, Alun TL Hughes, Timothy M Brown, Sara Namvar, and Hugh D Piggins. A riot of rhythms: neuronal and glial circadian oscillators in the mediobasal hypothalamus. *Molecular brain*, 2(1):28, 2009.
- [44] Tomoaki Muranaka and Tokitaka Oyama. Heterogeneity of cellular circadian clocks in intact plants and its correction under light-dark cycles. *Science advances*, 2(7):e1600500, 2016.
- [45] Alexis B Webb, Nikhil Angelo, James E Huettner, and Erik D Herzog. Intrinsic, nondeterministic circadian rhythm generation in identified mammalian neurons. *Proceedings of the National Academy of Sciences*, 106(38):16493–16498, 2009.
- [46] Caroline H Ko, Yujiro R Yamada, David K Welsh, Ethan D Buhr, Andrew C Liu, Eric E Zhang, Martin R Ralph, Steve A Kay, Daniel B Forger, and Joseph S Takahashi. Emergence of noise-induced oscillations in the central circadian pacemaker. *PLoS biology*, 8(10):e1000513, 2010.
- [47] Tomoaki Muranaka, Saya Kubota, and Tokitaka Oyama. A single-cell bioluminescence imaging system for monitoring cellular gene expression in a plant body. *Plant and Cell Physiology*, 54(12):2085–2093, 2013.
- [48] Kazuhito Goda, Yoko Hatta-Ohashi, Ryutaro Akiyoshi, Takashi Sugiyama, Ikuko Sakai, Takeo Takahashi, and Hirobumi Suzuki. Combining fluorescence and

- bioluminescence microscopy. *Microscopy research and technique*, 78(8):715–722, 2015.
- [49] Siting Gan and Erin K O’Shea. An unstable singularity underlies stochastic phasing of the circadian clock in individual cyanobacterial cells. *Molecular Cell*, 67(4):659–672, 2017.
- [50] Esther Yakir, Miriam Hassidim, Naomi Melamed-Book, Dror Hilman, Ido Kron, and Rachel M Green. Cell autonomous and cell-type specific circadian rhythms in arabidopsis. *The Plant Journal*, 68(3):520–531, 2011.
- [51] Laura Lande-Diner, Jacob Stewart-Ornstein, Charles J Weitz, and Galit Lahav. Single-cell analysis of circadian dynamics in tissue explants. *Molecular biology of the cell*, 26(22):3940–3945, 2015.
- [52] Takako Noguchi and Susan Golden. Bioluminescent and fluorescent reporters in circadian rhythm studies.
- [53] Andre Gross, Jonas Schoendube, Stefan Zimmermann, Maximilian Steeb, Roland Zengerle, and Peter Koltay. Technologies for single-cell isolation. *International journal of molecular sciences*, 16(8):16897–16919, 2015.
- [54] Satoshi Ishii, Kanako Tago, and Keishi Senoo. Single-cell analysis and isolation for microbiology and biotechnology: methods and applications. *Applied microbiology and biotechnology*, 86(5):1281–1292, 2010.
- [55] Ping Hu, Wenhua Zhang, Hongbo Xin, and Glenn Deng. Single cell isolation and analysis. *Frontiers in cell and developmental biology*, 4:116, 2016.

- [56] WJ Alland. Tumor cells circulate in the peripheral blood of all major carcinomas but not in healthy or patients with non-malignant diseases. *Clin Cancer Res*, 10:6897–6904, 2004.
- [57] George M Whitesides. The origins and the future of microfluidics. *Nature*, 442(7101):368–373, 2006.
- [58] A James Link, Ki Jun Jeong, and George Georgiou. Beyond toothpicks: new methods for isolating mutant bacteria. *Nature Reviews Microbiology*, 5(9):680–688, 2007.
- [59] M. R. Bennett and J. Hasty. Microfluidic devices for measuring gene network dynamics in single cells. *Nat Rev Genet*, 10(9):628–38, 2009.
- [60] V. Lecault, A. K. White, A. Singhal, and C. L. Hansen. Microfluidic single cell analysis: from promise to practice. *Curr Opin Chem Biol*, 16(3-4):381–90, 2012.
- [61] Haakan N. Joensson and Helene Andersson Svahn. Droplet microfluidics—a tool for single-cell analysis. *Angewandte Chemie International Edition*, 51(49):12176–12192, 2012.
- [62] W. M. Weaver, P. Tseng, A. Kunze, M. Masaeli, A. J. Chung, J. S. Dudani, H. Kittur, R. P. Kulkarni, and D. Di Carlo. Advances in high-throughput single-cell microtechnologies. *Curr Opin Biotechnol*, 25:114–23, 2014.
- [63] Agata Rakszewska, Jurjen Tel, Venkatachalam Chokkalingam, and Wilhelm T. S. Huck. One drop at a time: toward droplet microfluidics as a versatile tool for single-cell analysis. *NPG Asia Mater*, 6:e133, 2014.

- [64] R. Gomez-Sjoberg, A. A. Leyrat, D. M. Pirone, C. S. Chen, and S. R. Quake. Versatile, fully automated, microfluidic cell culture system. *Anal Chem*, 79(22):8557–63, 2007.
- [65] N. H. Youssef, P. C. Blainey, S. R. Quake, and M. S. Elshahed. Partial genome assembly for a candidate division op11 single cell from an anoxic spring (zodletone spring, oklahoma). *Appl Environ Microbiol*, 77(21):7804–14, 2011.
- [66] K. Leung, H. Zahn, T. Leaver, K. M. Konwar, N. W. Hanson, A. P. Page, C. C. Lo, P. S. Chain, S. J. Hallam, and C. L. Hansen. A programmable droplet-based microfluidic device applied to multiparameter analysis of single microbes and microbial communities. *Proc Natl Acad Sci U S A*, 109(20):7665–70, 2012.
- [67] S. Vedel, S. Tay, D. M. Johnston, H. Bruus, and S. R. Quake. Migration of cells in a social context. *Proc Natl Acad Sci U S A*, 110(1):129–34, 2013.
- [68] M. X. Gu. Microfluidic single-cell analysis shows that porcine induced pluripotent stem cell-derived endothelial cells improve myocardial function by paracrine activation. *Circulation research*, 111(7):882–893, 2012.
- [69] T. Frank and S. Tay. Flow-switching allows independently programmable, extremely stable, high-throughput diffusion-based gradients. *Lab Chip*, 13(7):1273–81, 2013.
- [70] Peng Shi, Mark A. Scott, Balaram Ghosh, Dongpeng Wan, Zachary Wissner-Gross, Ralph Mazitschek, Stephen J. Haggarty, and Mehmet Fatih Yanik. Synapse

- microarray identification of small molecules that enhance synaptogenesis. *Nature Communications*, 2:510–510, 2011.
- [71] Q. Han, N. Bagheri, E. M. Bradshaw, D. A. Hafler, D. A. Lauffenburger, and J. C. Love. Polyfunctional responses by human t cells result from sequential release of cytokines. *Proc Natl Acad Sci U S A*, 109(5):1607–12, 2012.
- [72] E. Cimetta, C. Cannizzaro, R. James, T. Biechele, R. T. Moon, N. Elvassore, and G. Vunjak-Novakovic. Microfluidic device generating stable concentration gradients for long term cell culture: application to wnt3a regulation of beta-catenin signaling. *Lab Chip*, 10(23):3277–83, 2010.
- [73] H. Zhu, G. Stybayeva, J. Silangcruz, J. Yan, E. Ramanculov, S. Dandekar, M. D. George, and A. Revzin. Detecting cytokine release from single t-cells. *Anal Chem*, 81(19):8150–6, 2009.
- [74] Q. Zhang, G. Lambert, D. Liao, H. Kim, K. Robin, C. K. Tung, N. Pourmand, and R. H. Austin. Acceleration of emergence of bacterial antibiotic resistance in connected microenvironments. *Science*, 333(6050):1764–7, 2011.
- [75] A. Jin, T. Ozawa, K. Tajiri, T. Obata, S. Kondo, K. Kinoshita, S. Kadowaki, K. Takahashi, T. Sugiyama, H. Kishi, and A. Muraguchi. A rapid and efficient single-cell manipulation method for screening antigen-specific antibody-secreting cells from human peripheral blood. *Nat Med*, 15(9):1088–92, 2009.

- [76] J. C. Love, J. L. Ronan, G. M. Grotenbreg, A. G. van der Veen, and H. L. Ploegh. A microengraving method for rapid selection of single cells producing antigen-specific antibodies. *Nat Biotechnol*, 24(6):703–7, 2006.
- [77] Xavier A. Figueroa, Gregory A. Cooksey, Scott V. Votaw, Lisa F. Horowitz, and Albert Folch. Large-scale investigation of the olfactory receptor space using a microfluidic microwell array. *Lab On A Chip*, 10(9):1120–1127, 2010.
- [78] Y. Liu. Simultaneous detection of cell-secreted tnf-a and ifn-g using micropatterned aptamer-modified electrodes. *Biomaterials*, 33(30):7347–7355, 2012.
- [79] S. A. Kobel, O. Burri, A. Griffa, M. Girotra, A. Seitz, and M. P. Lutolf. Automated analysis of single stem cells in microfluidic traps. *Lab Chip*, 12(16):2843–9, 2012.
- [80] A. M. Skelley, O. Kirak, H. Suh, R. Jaenisch, and J. Voldman. Microfluidic control of cell pairing and fusion. *Nat Methods*, 6(2):147–52, 2009.
- [81] J. Ryley and O. M. Pereira-Smith. Microfluidics device for single cell gene expression analysis in *saccharomyces cerevisiae*. *Yeast*, 23(14-15):1065–73, 2006.
- [82] E. Brouzes, M. Medkova, N. Savenelli, D. Marran, M. Twardowski, J. B. Hutchison, J. M. Rothberg, D. R. Link, N. Perrimon, and M. L. Samuels. Droplet microfluidic technology for single-cell high-throughput screening. *Proc Natl Acad Sci U S A*, 106(34):14195–200, 2009.
- [83] J. Q. Boedicker, M. E. Vincent, and R. F. Ismagilov. Microfluidic confinement of single cells of bacteria in small volumes initiates high-density behavior of

- quorum sensing and growth and reveals its variability. *Angew Chem Int Ed Engl*, 48(32):5908–11, 2009.
- [84] J. Clausell-Tormos, D. Lieber, J. C. Baret, A. El-Harrak, O. J. Miller, L. Frenz, J. Blouwolff, K. J. Humphry, S. Koster, H. Duan, C. Holtze, D. A. Weitz, A. D. Griffiths, and C. A. Merten. Droplet-based microfluidic platforms for the encapsulation and screening of mammalian cells and multicellular organisms. *Chem Biol*, 15(5):427–37, 2008.
- [85] A. C. Hatch, J. S. Fisher, A. R. Tovar, A. T. Hsieh, R. Lin, S. L. Pentoney, D. L. Yang, and A. P. Lee. 1-million droplet array with wide-field fluorescence imaging for digital pcr. *Lab Chip*, 11(22):3838–45, 2011.
- [86] L. Warren, D. Bryder, I. L. Weissman, and S. R. Quake. Transcription factor profiling in individual hematopoietic progenitors by digital rt-pcr. *Proc Natl Acad Sci U S A*, 103(47):17807–12, 2006.
- [87] Q. Shi, L. Qin, W. Wei, F. Geng, R. Fan, Y. S. Shin, D. Guo, L. Hood, P. S. Mischel, and J. R. Heath. Single-cell proteomic chip for profiling intracellular signaling pathways in single tumor cells. *Proc Natl Acad Sci U S A*, 109(2):419–24, 2012.
- [88] A. Rosenthal, A. Macdonald, and J. Voldman. Cell patterning chip for controlling the stem cell microenvironment. *Biomaterials*, 28(21):3208–16, 2007.
- [89] Y. S. Hwang, B. G. Chung, D. Ortmann, N. Hattori, H. C. Moeller, and A. Khademhosseini. Microwell-mediated control of embryoid body size regulates

- embryonic stem cell fate via differential expression of wnt5a and wnt11. *Proc Natl Acad Sci U S A*, 106(40):16978–83, 2009.
- [90] S. Gobaa, S. Hoehnel, M. Roccio, A. Negro, S. Kobel, and M. P. Lutolf. Artificial niche microarrays for probing single stem cell fate in high throughput. *Nat Methods*, 8(11):949–55, 2011.
- [91] J. C. Baret, Y. Beck, I. Billas-Massobrio, D. Moras, and A. D. Griffiths. Quantitative cell-based reporter gene assays using droplet-based microfluidics. *Chem Biol*, 17(5):528–36, 2010.
- [92] Y. J. Yamanaka, G. L. Szeto, T. M. Gierahn, T. L. Forcier, K. F. Benedict, M. S. Brefo, D. A. Lauffenburger, D. J. Irvine, and J. C. Love. Cellular barcodes for efficiently profiling single-cell secretory responses by microengraving. *Anal Chem*, 84(24):10531–6, 2012.
- [93] K. Eyer, S. Stratz, P. Kuhn, S. K. Kuster, and P. S. Dittrich. Implementing enzyme-linked immunosorbent assays on a microfluidic chip to quantify intracellular molecules in single cells. *Anal Chem*, 85(6):3280–7, 2013.
- [94] J. Pan, A. L. Stephenson, E. Kazamia, W. T. Huck, J. S. Dennis, A. G. Smith, and C. Abell. Quantitative tracking of the growth of individual algal cells in microdroplet compartments. *Integr Biol (Camb)*, 3(10):1043–51, 2011.
- [95] Rowland H. Davis and Frederick J. de Serres. [4] genetic and microbiological research techniques for neurospora crassa. *Methods in Enzymology*, 17:79–143, 1970.

- [96] K. M. Lindgren. *Characterization of ccg-1, a clock-controlled gene of Neurospora crassa*. PhD thesis, 1994.
- [97] Hildur V Colot, Gyungsoon Park, Gloria E Turner, Carol Ringelberg, Christopher M Crew, Liubov Litvinkova, Richard L Weiss, Katherine A Borkovich, and Jay C Dunlap. A high-throughput gene knockout procedure for neurospora reveals functions for multiple transcription factors. *Proceedings of the National Academy of Sciences*, 103(27):10352–10357, 2006.
- [98] Hao Gu, Michel HG Duits, and Frieder Mugele. Droplets formation and merging in two-phase flow microfluidics. *International journal of molecular sciences*, 12(4):2572–2597, 2011.
- [99] Jerry M Chen, Ming-Che Kuo, and Chien-Po Liu. Control of droplet generation in flow-focusing microfluidic device with a converging-diverging nozzle-shaped section. *Japanese Journal of Applied Physics*, 50(10R):107301, 2011.
- [100] Younan Xia and George M. Whitesides. Soft lithography. *Annual Review of Materials Science*, 28(1):153–184, 1998.
- [101] GE Healthcare Life Sciences percoll description. <http://www.gelifesciences.com/webapp/wcs/stores/servlet/ProductDisplay?categoryId=11704&catalogId=10101&productId=22976&storeId=11787&langId=-1>. Accessed: 2017-09-08.
- [102] Michael W. Young. *Circadian rhythms*. Methods in enzymology ;. San Diego, Elsevier Academic Press, 2005.

- [103] Mariko Izumo, Takashi R Sato, Martin Straume, and Carl Hirschie Johnson. Quantitative analyses of circadian gene expression in mammalian cell cultures. *PLoS computational biology*, 2(10):e136, 2006.
- [104] Z. Deng, S. Arsenault, C. Caranica, J. Griffith, T. Zhu, A. Al-Omari, H. B. Schuttler, J. Arnold, and L. Mao. Synchronizing stochastic circadian oscillators in single cells of *neurospora crassa*. *Sci Rep*, 6:35828, 2016.
- [105] M. Izumo, T. R. Sato, M. Straume, and C. H. Johnson. Quantitative analyses of circadian gene expression in mammalian cell cultures. *PLoS Comput Biol*, 2(10):e136, 2006.
- [106] Md Arafat Hossain, John Canning, Zhikang Yu, Sandra Ast, Peter J Rutledge, Joseph K-H Wong, Abbas Jamalipour, and Maxwell J Crossley. Time-resolved and temperature tuneable measurements of fluorescent intensity using a smartphone fluorimeter. *Analyst*, 2017.
- [107] Vinay K Natrajan and Kenneth T Christensen. Development of fluorescent thermometry methods for microfluidic systems. In *14th Int Symp on Applications of Laser Techniques to Fluid Mechanics (Lisbon, 2008)*, 2008.
- [108] Susanne Ebert, Kort Travis, Bryan Lincoln, and Jochen Guck. Fluorescence ratio thermometry in a microfluidic dual-beam laser trap. *Optics express*, 15(23):15493–15499, 2007.
- [109] XA Cao, SF LeBoeuf, and TE Stecher. Temperature-dependent electroluminescence of algan-based uv leds. *IEEE electron device letters*, 27(5):329–331, 2006.

- [110] Akvilė Zabaliūtė. Temperature characteristics of leds.
- [111] Octavio Mondragón-Palomino, Tal Danino, Jangir Selimkhanov, Lev Tsimring, and Jeff Hasty. Entrainment of a population of synthetic genetic oscillators. *Science*, 333(6047):1315–1319, 2011.
- [112] Pablo Meyer, Lino Saez, and Michael W Young. Per-tim interactions in living drosophila cells: an interval timer for the circadian clock. *Science*, 311(5758):226–229, 2006.
- [113] Daisuke Ono, Sato Honma, and Ken-ichi Honma. Cryptochromes are critical for the development of coherent circadian rhythms in the mouse suprachiasmatic nucleus. *Nature communications*, 4:1666, 2013.
- [114] Shun Yamaguchi, Hiromi Isejima, Takuya Matsuo, Ryusuke Okura, Kazuhiro Yagita, Masaki Kobayashi, and Hitoshi Okamura. Synchronization of cellular clocks in the suprachiasmatic nucleus. *Science*, 302(5649):1408–1412, 2003.
- [115] Sara J Aton, Christopher S Colwell, Anthony J Hattar, James Waschek, and Erik D Herzog. Vasoactive intestinal polypeptide mediates circadian rhythmicity and synchrony in mammalian clock neurons. *Nature neuroscience*, 8(4):476, 2005.
- [116] Jihwan Myung, Sungho Hong, Daniel DeWoskin, Erik De Schutter, Daniel B Forger, and Toru Takumi. Gaba-mediated repulsive coupling between circadian clock neurons in the scn encodes seasonal time. *Proceedings of the National Academy of Sciences*, 112(29):E3920–E3929, 2015.

- [117] Mary E Case, James Griffith, Wubei Dong, Ira L Tigner, Kimberly Gaines, James C Jiang, S Michal Jazwinski, and Jonathan Arnold. The aging biological clock in *neurospora crassa*. *Ecology and evolution*, 4(17):3494–3507, 2014.
- [118] Y. Yu, W. Dong, C. Altimus, X. Tang, J. Griffith, M. Morello, L. Dudek, J. Arnold, and H. B. Schuttler. A genetic network for the clock of *neurospora crassa*. *Proc Natl Acad Sci U S A*, 104(8):2809–14, 2007.
- [119] M. B. Elowitz, A. J. Levine, E. D. Siggia, and P. S. Swain. Stochastic gene expression in a single cell. *Science*, 297(5584):1183–6, 2002.
- [120] W. Dong, X. Tang, Y. Yu, R. Nilsen, R. Kim, J. Griffith, J. Arnold, and H. B. Schuttler. Systems biology of the clock in *neurospora crassa*. *PLoS One*, 3(8):e3105, 2008.
- [121] Daniel T Gillespie. Exact stochastic simulation of coupled chemical reactions. *The journal of physical chemistry*, 81(25):2340–2361, 1977.
- [122] M. Kendall and A. Stuart. *The advanced theory of statistics. Vol.2: Inference and relationship*. 1979.
- [123] Ronald A. Fisher and Frank Yates. *Statistical Tables for Biological, Agricultural and Medical Research*. Oliver and Boyd, London, 1948. 3d ed.
- [124] T. Kreuz, F. Mormann, R. G. Andrzejak, A. Kraskov, K. Lehnertz, and P. Grassberger. Measuring synchronization in coupled model systems: A comparison of different approaches. *Physica D Nonlinear Phenomena*, 225:29–42, January 2007.

- [125] Luis Fernando Larrondo Castro. Decoupling circadian clock protein turnover from circadian period determination. *Science*, 2015.
- [126] Laura B Duvall and Paul H Taghert. The circadian neuropeptide pdf signals preferentially through a specific adenylate cyclase isoform ac3 in m pacemakers of drosophila. *PLoS biology*, 10(6):e1001337, 2012.
- [127] Tal Danino, Octavio Mondragon-Palomino, Lev Tsimring, and Jeff Hasty. A synchronized quorum of genetic clocks. *Nature*, 463(7279):326, 2010.
- [128] Roberto Benzi. Stochastic resonance: from climate to biology. In *Collective Phenomena in Macroscopic Systems*, pages 79–95. World Scientific, 2007.
- [129] Ozgur E Akman, Maria Luisa Guerriero, Laurence Loewe, and Carl Troein. Complementary approaches to understanding the plant circadian clock. *arXiv preprint arXiv:1002.4661*, 2010.
- [130] D. J. Durgan and M. E. Young. The cardiomyocyte circadian clock: emerging roles in health and disease. *Circ Res*, 106(4):647–58, 2010.
- [131] Ekkehard Ullner, Javier Buceta, Antoni Díez-Noguera, and Jordi García-Ojalvo. Noise-induced coherence in multicellular circadian clocks. *Biophysical journal*, 96:3573–3581, May 2009.
- [132] U. Abraham, A. E. Granada, P. O. Westermark, M. Heine, A. Kramer, and H. Herzel. Coupling governs entrainment range of circadian clocks. *Mol Syst Biol*, 6:438, 2010.

- [133] Amanda-Jayne F Carr and David Whitmore. Imaging of single light-responsive clock cells reveals fluctuating free-running periods. *Nature cell biology*, 7(3):319, 2005.
- [134] Martha Merrow, Michael Brunner, and Till Roenneberg. Assignment of circadian function for the neurospora clock gene frequency. *Nature*, 399(6736):584, 1999.
- [135] Christian Heintzen, Jennifer J Loros, and Jay C Dunlap. The pas protein vivid defines a clock-associated feedback loop that represses light input, modulates gating, and regulates clock resetting. *Cell*, 104(3):453–464, 2001.
- [136] Elan Gin, Axel CR Diernfellner, Michael Brunner, and Thomas Höfer. The neurospora photoreceptor vivid exerts negative and positive control on light sensing to achieve adaptation. *Molecular systems biology*, 9(1):667, 2013.
- [137] Yi Liu, Norman Y Garceau, Jennifer J Loros, and Jay C Dunlap. Thermally regulated translational control of frq mediates aspects of temperature responses in the neurospora circadian clock. *Cell*, 89(3):477–486, 1997.
- [138] Peter Ruoff, Maxim Zakhartsev, and Hans V Westerhoff. Temperature compensation through systems biology. *The FEBS journal*, 274(4):940–950, 2007.
- [139] J Woodland Hastings and Beatrice M Sweeney. On the mechanism of temperature independence in a biological clock. *Proceedings of the National Academy of Sciences*, 43(9):804–811, 1957.
- [140] Peter Ruoff. Introducing temperature-compensation in any reaction kinetic oscillator model. 1992.

- [141] J Buhl, D J T Sumpter, I D Couzin, J J Hale, E Despland, E R Miller, and S J Simpson. From disorder to order in marching locusts. *Science (New York, N.Y.)*, 312:1402–1406, June 2006.
- [142] J. Garcia-Ojalvo, M. B. Elowitz, and S. H. Strogatz. Modeling a synthetic multicellular clock: repressilators coupled by quorum sensing. *Proc Natl Acad Sci U S A*, 101(30):10955–60, 2004.
- [143] Shayle R Searle, George Casella, and Charles E McCulloch. *Variance components*, volume 391. John Wiley & Sons, 2009.
- [144] Z Deng, S Arsenault, L Mao, and J Arnold. Measuring synchronization of stochastic oscillators in biology. In *Journal of Physics: Conference Series*, volume 750, page 012001. IOP Publishing, 2016.
- [145] Sarah B Holt. Genetics of dermal ridges: Inheritance of total finger ridge-count. *Annals of Human Genetics*, 18(1):140–161, 1953.
- [146] D. Gonze. Spontaneous synchronization of coupled circadian oscillators. *Biophysical Journal*, 89:120–129, July 2005.
- [147] Takashi Nishikawa, Adilson E Motter, Ying-Cheng Lai, and Frank C Hoppensteadt. Heterogeneity in oscillator networks: are smaller worlds easier to synchronize? *Physical review letters*, 91:014101, July 2003.
- [148] Javier Palma-Guerrero, Charles R Hall, David Kowbel, Juliet Welch, John W Taylor, Rachel B Brem, and N Louise Glass. Genome wide association identifies novel loci involved in fungal communication. *PLoS Genetics*, 9(8):e1003669, 0 2013.

- [149] Eric Nudleman, Daniel Wall, and Dale Kaiser. Cell-to-cell transfer of bacterial outer membrane lipoproteins. *Science (New York, N.Y.)*, 309:125–127, July 2005.
- [150] J. K. Kim. Protein sequestration versus hill-type repression in circadian clock models. *IET Systems Biology*, 10(4):125–135, 2016.
- [151] Allan C Froehlich, Yi Liu, Jennifer J Loros, and Jay C Dunlap. White collar-1, a circadian blue light photoreceptor, binding to the frequency promoter. *Science (New York, N.Y.)*, 297:815–819, August 2002.
- [152] A. Al-Omari, J. Griffith, M. Judge, T. Taha, J. Arnold, and H. B. Schüttler. Discovering regulatory network topologies using ensemble methods on gpppus with special reference to the biological clock of neurospora crassa. *IEEE Access*, 3:27–42, 2015.
- [153] Jae Kyoung Kim, Zachary P Kilpatrick, Matthew R Bennett, and Krešimir Josić. Molecular mechanisms that regulate the coupled period of the mammalian circadian clock. *Biophysical journal*, 106(9):2071–2081, 2014.
- [154] A. F. Taylor, M. R. Tinsley, F. Wang, Z. Huang, and K. Showalter. Dynamical quorum sensing and synchronization in large populations of chemical oscillators. 323:614–617, 2009.
- [155] Yoshiki Kuramoto. *Chemical oscillations, waves, and turbulence*, 1984.
- [156] António M Pogueiro, Qiuyun Liu, Christopher L Baker, Jay C Dunlap, and Jennifer J Loros. The neurospora checkpoint kinase 2: a regulatory link between the circadian and cell cycles. *Science*, 313(5787):644–649, 2006.

- [157] Kok Hao Chen, Alistair N Boettiger, Jeffrey R Moffitt, Siyuan Wang, and Xiaowei Zhuang. Spatially resolved, highly multiplexed rna profiling in single cells. *Science*, 348(6233):aaa6090, 2015.
- [158] Alejandro Correa, Zachary A Lewis, Andrew V Greene, Irene J March, Richard H Gomer, and Deborah Bell-Pedersen. Multiple oscillators regulate circadian gene expression in neurospora. *Proceedings of the National Academy of Sciences*, 100(23):13597–13602, 2003.
- [159] P. L. Lakin-Thomas and S. Brody. Circadian rhythms in neurospora crassa: Lipid deficiencies restore robust rhythmicity to null frequency and white-collar mutants. 97:256–261, 2000.
- [160] Arthur T Winfree. On emerging coherence. *Science*, 298(5602):2336–2337, 2002.
- [161] Mark D. McDonnell and Derek Abbott. What is stochastic resonance? definitions, misconceptions, debates, and its relevance to biology. *PLoS Computational Biology*, 5(5), 2009.
- [162] Z. Hou and H. Xin. Internal noise stochastic resonance in a circadian clock system. , 119:11508–11512, December 2003.
- [163] Joris Paijmans, Mark Bosman, Pieter Rein Ten Wolde, and David K Lubensky. Discrete gene replication events drive coupling between the cell cycle and circadian clocks. *Proceedings of the National Academy of Sciences of the United States of America*, 113:4063–4068, April 2016.

- [164] Rowland H. Davis. *Neurospora*. Oxford Univ. Press, Oxford [u.a.], 2000. Includes bibliographical references and index.
- [165] Tao Geng, Erin L Bredeweg, Craig J Szymanski, Bingwen Liu, Scott E Baker, Galya Orr, James E Evans, and Ryan T Kelly. Compartmentalized microchannel array for high-throughput analysis of single cell polarized growth and dynamics. *Scientific reports*, 5:16111, November 2015.
- [166] Niko Komin, Adrian C. Murza, Emilio Hernandez-Garcia, and Raul Toral. Synchronization and entrainment of coupled circadian oscillators.
- [167] Didier Gonze, José Halloy, and Albert Goldbeter. Stochastic models for circadian oscillations: Emergence of a biological rhythm. *International Journal of Quantum Chemistry*, 98(2):228–238, 2004.
- [168] Samuel Bernard, Didier Gonze, Branka Čajavec, Hanspeter Herzog, and Achim Kramer. Synchronization-induced rhythmicity of circadian oscillators in the suprachiasmatic nucleus. *PLoS computational biology*, 3(4):e68, 2007.